



Journal of Electromagnetic Analysis and Applications

ISSN: 1942-0730 (Print), 1942-0749 (Online)

Volume 1, Number 1, March 2009

www.scirp.org/journal/jemaa



*Scientific
Research
Publishing*

JOURNAL EDITORIAL BOARD

ISSN: 1942-0730 (Print) 1942-0749 (Online)

[Http://www.scirp.org/journal/jemaa](http://www.scirp.org/journal/jemaa)

Editor-in-Chief

Prof. James L. Drewniak University of Missouri-Rolla, USA
Prof. Yuanzhang Sun Wuhan University, China

Editorial Board (According to Alphabet)

Dr. Mazen Abd El-Salam Assiut University, Egypt
Dr. Ji Chen University of Houston, USA
Dr. Isabel Jessus Institute of Engineering of Porto, Portugal
Dr. Ozlem Ozgun Middle East Technical University, Turkey
Dr. Jiangjun Ruan Wuhan University, China
Dr. Yuanzhang Sun Wuhan University, China
Dr. Wenhua Yu Pennsylvania State University, USA
Dr. Jun Zou Zhejiang University, China
Dr. Xijiang Han Harbin Institute of Technology, China

Editorial Assistants

Xiao-Qian Qi Wuhan University, China
Dao-Chun Huang Wuhan University, China

Guest Reviewers (According to Alphabet)

A.K. Al-Othman	Peisheng Li	Pedro Roncero-Sánchez
C.B. Chiou	Elahe Mashhour	Bojan Štumberger
Florian Herrault	Abderrazak Ouali	Sheng-Kuan Wang
Anwar Ul-Hamid	C. Christober Asir Rajan	Yu Fu Wing
Jian Le	Martin Hagsted Rasmussen	Ben Young

CONTENTS

Volume 1 Number 1

March 2009

Analysis of the Magnetic Flux Density, the Magnetic Force and the Torque in a 3D Brushless DC Motor	
M. Pakdel.....	1
Ion Exchange Softening and Alkalization Treatment for Zerodischarge of Circulating Cooling Water	
X. Z. Bu, L. Xu & L. Su.....	6
Reduction of Cogging Torque in Permanent Magnet Flux-Switching Machines	
Y. Wang, J. X. Shen, W. Z. Fei & Z. X. Fang.....	11
Impact of Reactive Power in Power Evacuation from Wind Turbines	
A. Ranjan, S. P. Karthikeyan, A. Ahuja, K. Palanisamy, I. J. Raglend & D. P. Kothari.....	15
Some Advances in the Application of Weathering and Cold-Formed Steel in Transmission Tower	
F. L. Yang, J. K. Han, J. B. Yang & Z. Li.....	24
Identification of Lightning Stroke and Fault in the Travelling Wave Protection	
G. B. Zou, H. L. Gao, W. B. Su & D. P. Wang.....	31
Desulphurization Characteristic of Industry Alkaline Wastes during Coal Combustion	
B. Zheng & C. M. Lu.....	36
The Online Assessment of Electric Distribution Network Load Capability	
H. M. Liu, Z. K. Li, K. Yu & X. Y. Chen.....	42
Complex Dynamics Analysis for Cournot Game with Bounded Rationality in Power Market	
H. M. Yang & Y. X. Zhang.....	48
The Preliminary Design of IPv6 Home Gateway and Terminal	
C. Y. Wang & R. Gao.....	61
Analysis and Design of a Kind of Improved Parallel Resonant Converters	
C. H. Yuan, J. R. Wan, X. Y. Li, H. Shen, Y. P. Liu & G. Y. Li.....	66

Journal of Electromagnetic Analysis and Applications (JEMAA)

Journal Information

SUBSCRIPTIONS

The *Journal of Electromagnetic Analysis and Applications* (Online at Scientific Research Publishing, www.SciRP.org) is published quarterly by Scientific Research Publishing, Inc. 5005 Paseo Segovia, Irvine, CA 92603-3334, USA.

E-mail: jemaa@scirp.org

Subscription rates: Volume 1 2009

Print: \$50 per copy.

Electronic: free, available on www.SciRP.org.

To subscribe, please contact Journals Subscriptions Department, E-mail: jemaa@scirp.org

Sample copies: If you are interested in subscribing, you may obtain a free sample copy by contacting Scientific Research Publishing, Inc at the above address.

SERVICES

Advertisements

Advertisement Sales Department, E-mail: jemaa@scirp.org

Reprints (minimum quantity 100 copies)

Reprints Co-ordinator, Scientific Research Publishing, Inc. 5005 Paseo Segovia, Irvine, CA 92603-3334, USA.

E-mail: jemaa@scirp.org

COPYRIGHT

Copyright©2009 Scientific Research Publishing, Inc.

All Rights Reserved. No part of this publication may be reproduced, stored in a retrieval system, or transmitted, in any form or by any means, electronic, mechanical, photocopying, recording, scanning or otherwise, except as described below, without the permission in writing of the Publisher.

Copying of articles is not permitted except for personal and internal use, to the extent permitted by national copyright law, or under the terms of a license issued by the national Reproduction Rights Organization.

Requests for permission for other kinds of copying, such as copying for general distribution, for advertising or promotional purposes, for creating new collective works or for resale, and other enquiries should be addressed to the Publisher.

Statements and opinions expressed in the articles and communications are those of the individual contributors and not the statements and opinion of Scientific Research Publishing, Inc. We assume no responsibility or liability for any damage or injury to persons or property arising out of the use of any materials, instructions, methods or ideas contained herein. We expressly disclaim any implied warranties of merchantability or fitness for a particular purpose. If expert assistance is required, the services of a competent professional person should be sought.

PRODUCTION INFORMATION

For manuscripts that have been accepted for publication, please contact:

E-mail: jemaa@scirp.org

Analysis of the Magnetic Flux Density, the Magnetic Force and the Torque in a 3D Brushless DC Motor

Majid Pakdel¹

¹Isfahan University of Technology, Isfahan, Iran.
Email: majidpakdel@yahoo.com

Received January 8th, 2009; revised February 4th, 2009; accepted February 18th, 2009.

ABSTRACT

As permanent magnet motors and generators produce torque, vibration occurs through the small air gap due to the alternating magnetic forces created by the rotating permanent magnets and the current switching of the coils. The magnetic force can be calculated from the flux density by finite element methods and the Maxwell stress tensor in cylindrical coordinates. In this paper the magnetic flux density, the magnetic force and the torque of a real three dimensional brushless DC motor are simulated using Maxwell 3 D V 11.1.

Keywords: Brushless DC Motor, Finite Element Analysis, Maxwell 3 D V 11.1

1. Introduction

Magnetic force analysis is important in determining not only the torque as the output of motor, but also the source of vibration in machine itself. Vibration is induced in permanent magnet DC motors and generators as shown in Figure 1, by traveling magnetic forces. Neodymium and other rare earths have greater retentivity, coercive force and maximum energy product than traditional ferrite magnets. Therefore, since the magnetic force increases approximately with the square of magnetic flux, the forces arising from designs using rare earth magnets are significantly greater than those from conventional magnet designs. These problems are particularly serious when the forcing frequencies match one or more of the structural resonant frequencies in the machine.

The analysis of magnetic force has been addressed by a number of investigators. Initially, papers mainly focused on the calculation of the torque as the output of motor. Marinescu *et al.* [1] and Mizia *et al.* [2] compared the several different methods to calculate the torque. Their efforts resulted in torque calculation at several different locations based on the quasi-static magnetic field, which were verified by experiments. The problem of magnetically generated vibration has been addressed by other investigators. Boules [3] analytically predicted the flux density in permanent magnet machine. Sabonnadiere *et al.* [4] calculated the magnetic force using the finite element method, while Lefevre *et al.* [5] did so with finite difference method along with determining the dynamic reaction with FEM. Rahman [6] and Jang [7] showed that the driving frequencies may be characterized by Fourier decomposition of the magnetic traction, and demonstrated that the vibration levels could be reduced by proper

shaping of the magnet. In addition Jang and Lieu [8] showed that the composition of the frequency spectrum can be shifted to higher frequencies to reduce the overall transmission to the base system. The transmissibility of the higher frequencies are low except when the structural resonance occurs. Vibration reduction could be effected by interlacing higher energy magnets and slightly changing the magnetic orientations at the pole transitions or by the interlocking of the magnets. In recent papers [9,10,11], the two dimensional finite element analysis of brushless DC motor has been reported, but three dimensional finite element analysis of brushless DC motor has not been reported in details.

In this paper, the characteristics of torque and magnetic force acting on the rotor are analyzed as the rotation of the rotor. The magnetic force in the motor with three poles and six teeth were calculated from the flux density by finite element methods and the Maxwell stress tensor. The component and the characteristics of the magnetic force and magnetic torque in a small air gap were analyzed with the introduction of cylindrical coordinate.

2. Magnetic Force and Torque

The magnetic field generated by a brushless DC motor is governed by the set of Maxwell's equations. Introducing the scalar potential into the Maxwell equations, with some mathematics, gives a single partial differential equation for the scalar potential.

$$\nabla^T \mu \nabla \phi - \nabla^T \mu H_s = 0 \quad (1)$$

The field intensity due to the current in the winding and the permanent magnet may always be calculated di-

rectly by the Biot-Savart law and the magnetic dipole moment per unit volume, respectively. This equation, like the Poisson's equation for electrostatic fields can be solved using finite element method. Maxwell 3D V11.1 a FEM solver for magnetic field was used to calculate the scalar potential ϕ and the magnetic field intensity H .

A non uniform distributed force per unit area at the interface between two materials is calculated by use of the Maxwell stress tensor. Since the strain imposed on the material due to magnetostriction is small enough to neglect changes in the density, it can be assumed that the change of permeability is negligible. Thus in tensor notation we have:

$$\sigma_{ij} = \frac{1}{\mu} (B_i B_j - \frac{1}{2} \sigma_{ij} B_k B_k) \quad (2)$$

where σ_{ij} is the Maxwell stress tensor. B_i is the magnetic flux density which is obtained by the multiplication of permeability to the magnetic flux density. From the expression given by Woodson and Melcher [12] for an interface between two materials a and b, the traction f_i , is given by:

$$f_i = (\sigma_{ij}^a - \sigma_{ij}^b) n_j \quad (3)$$

The normal and the tangential traction can be decomposed as follows:

$$f_n = (\sigma_{ij}^a - \sigma_{ij}^b) n_i n_j \quad (4)$$

$$f_t = \sqrt{|f_i|^2 - |f_n|^2} = |n \times f \times n| \quad (5)$$

Since $\mu_{air} \ll \mu_{iron}$, the magnetic traction can be simplified with the introduction of the cylindrical coordinate on the rotor. Along the air gap, the normal and the tangential traction for tooth face are as follows:

$$f_r \approx \sigma_{rr}^a = \frac{1}{2\mu_{air}} (B_r^2 - B_\theta^2 - B_z^2) \quad (6)$$

$$f_\theta \approx \sigma_{r\theta}^a = \frac{1}{\mu_{air}} B_r B_\theta \quad (7)$$

But for tooth side which is perpendicular to the air gap the normal and the tangential traction have the following form:

$$f_\theta \approx \sigma_{\theta\theta}^a = \frac{1}{2\mu_{air}} (B_\theta^2 - B_r^2 - B_z^2) \quad (8)$$

$$f_r \approx \sigma_{r\theta}^a = \frac{1}{\mu_{air}} B_r B_\theta \quad (9)$$

The torque produced for one position can easily be derived from the integration of the shear force along the small air gap with the fact the field distribution inside a closed surface in air remain unchanged if the external sources are removed and replaced by currents and poles on the surface:

$$T = \oint R \times f_\theta d\Omega \quad (10)$$

3. Modeling

The finite element method has a solid theoretical foundation. It is based on mathematical theorems that guarantee an asymptotic increase of the accuracy of the field calculation towards the exact solution as the size of the finite elements used in the solution process decreases. For time domain solutions the spatial discretization of the problem must be refined in a manner coordinated with the time steps of the calculation according to estimated time constants of the solution (such as magnetic diffusion time constant). Maxwell 3D V11.1 solves the electromagnetic field problems by solving Maxwell's equations in a finite region of space with appropriate boundary conditions and-when necessary-with user-specified initial conditions in order to obtain a solution with guaranteed uniqueness. In order to obtain the set of algebraic equations to be solved, the geometry of the problem is discretized automatically into tetrahedral elements. All the model solids are meshed automatically by the mesher. The assembly of all tetrahedra is referred to as the finite element mesh of the model or simply the mesh. Inside each tetrahedron, the unknowns characteristic for the field being calculated are represented as polynomials of second order. Thus, in regions with rapid spatial field variation, the mesh density needs to be increased for good solution accuracy (see also adaptive mesh refinement).

Solving an electromagnetic field problem is always based on solving Maxwell's equations. However the process of obtaining the solution is typically based on solving a second order consequence of Maxwell's equations with the consideration of applicable constitutive equations. At the same time-as a rule-a subset of complete Maxwell's equations is considered according to characteristic aspects of the application. Thus for reasons of efficiency of the solution, applications are classified as electrostatic, magnetostatic, frequency domain or time domain and as a consequence a specific type of solver is used in each case. This allows the users to obtain the solution with the desired accuracy but always within the limits of the fundamental assumptions made when the application was classified along the lines of the above mentioned criteria. The guide lines that can be used to correctly identify the type of solution to use are mentioned in the following paragraphs. The unknowns for each type of solution can be different, depending on the formulation.

The solution process for 3D transient applications poses several challenges not apparent for other solver types. For instance, the behavior of fields is more complex than it is for static or steady-state applications, and a special finite element mesh structure is required in order for the software to accurately represent the physics. For 3D transient applications, the behavior of the fields is more complex than it is for static or steady-state applications. A diffusion of the magnetic field into the materials occurs in 3D transient situations. The distribution of the magnetic field inside objects typically has a number of spatial harmonics, which usually means the time step used in the analysis should be less 7 (sometimes

much less) than the magnetic diffusion time constant. These time constants depend upon the geometry of objects and also upon their respective material properties. Since eddy currents are usually considered in conductive objects, a special finite element mesh structure is required in order to accurately capture the physics. In general, a careful planning of the (manual) meshing process is required in order to achieve an accurate solution with the available hardware resources. The three dimensional view of the Brushless DC motor is shown in Figure 1.

4. Simulation Results

It is assumed that the square voltages with amplitude of 311 V and frequency of 60 Hz are applied to the brushless DC motor as shown in Figure 2. The brushless DC motor is simulated in the interval of 0 to 0.02 seconds with 0.002s of time step. The magnitude of flux density in times of 0.004s, 0.006s, 0.008s, 0.01s, 0.012s, 0.014s, 0.016s, 0.018s and 0.02s are shown in Figures 3–11. Also, the diagrams of the torque and the force in the z, y and x directions are shown in Figures 12–17 respectively.

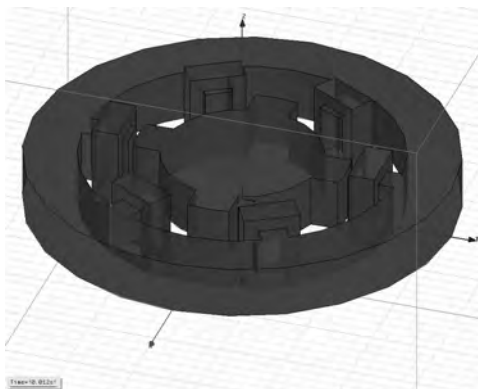


Figure 1. Three dimensional brushless DC motor

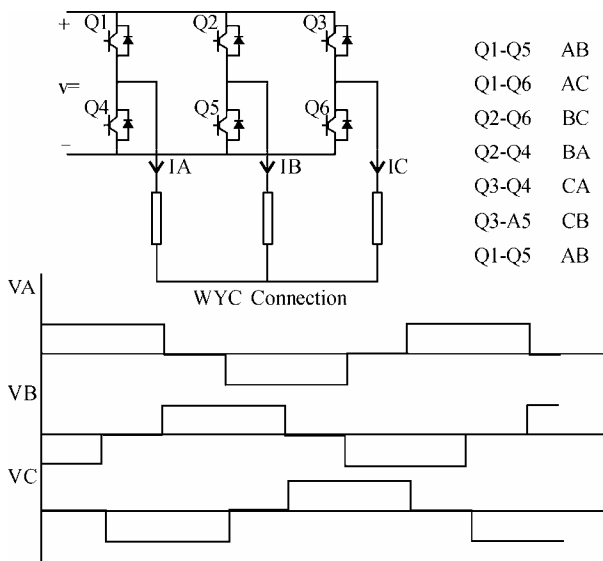


Figure 2. Input voltage waveforms and stator excitation inverter

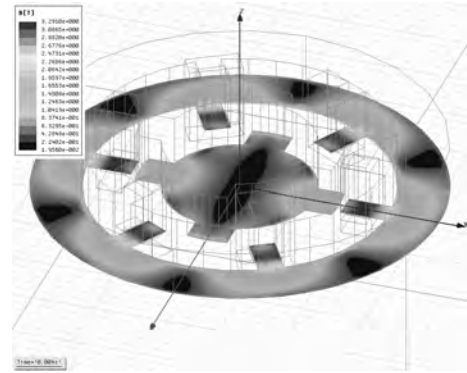


Figure 3. Magnetic flux density in 0.004 s

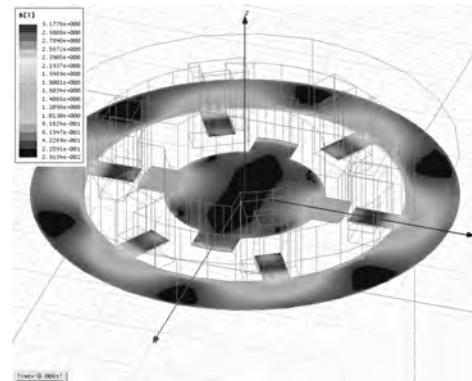


Figure 4. Magnetic flux density in 0.006 s

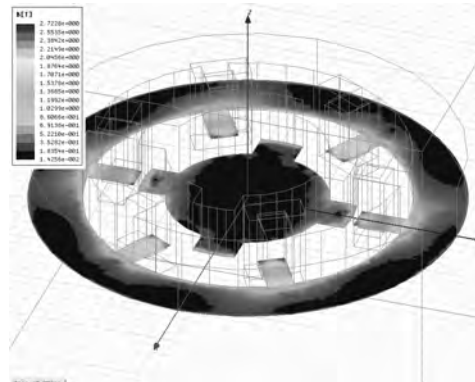


Figure 5. Magnetic flux density in 0.008 s

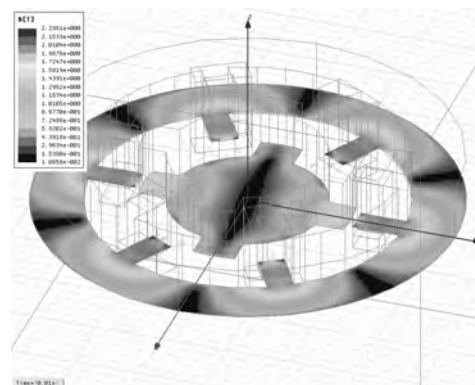


Figure 6. Magnetic flux density in 0.01 s

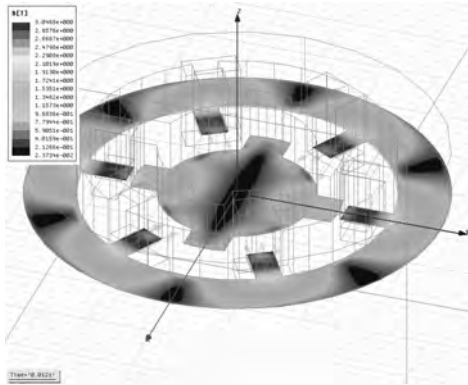


Figure 7. Magnetic flux density in 0.012 s

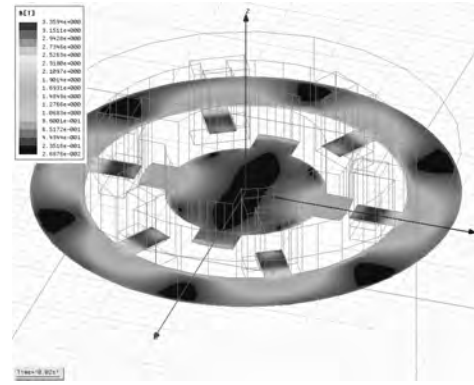


Figure 11. Magnetic flux density in 0.02 s

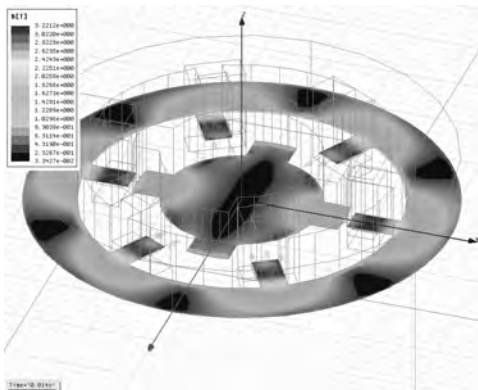


Figure 8. Magnetic flux density in 0.014 s

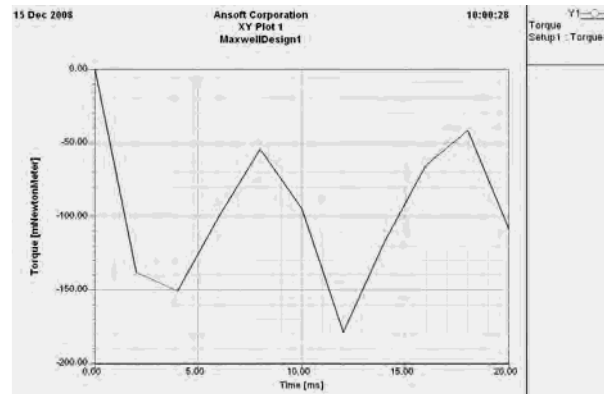


Figure 12. Torque in z-direction

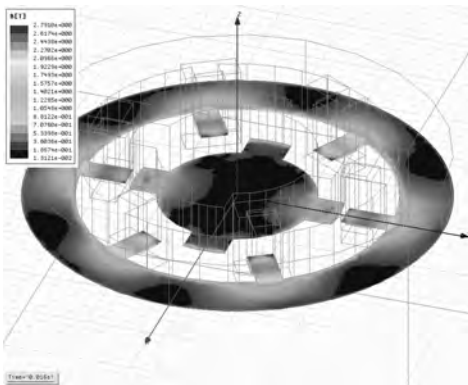


Figure 9. Magnetic flux density in 0.016 s

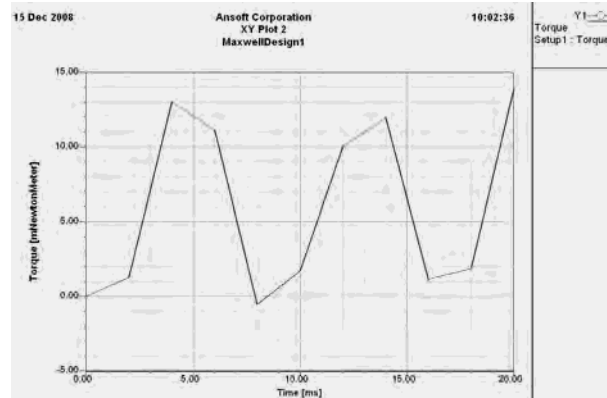


Figure 13. Torque in y-direction

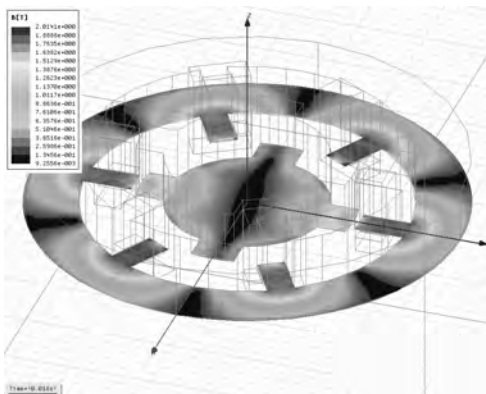


Figure 10. Magnetic flux density in 0.018 s

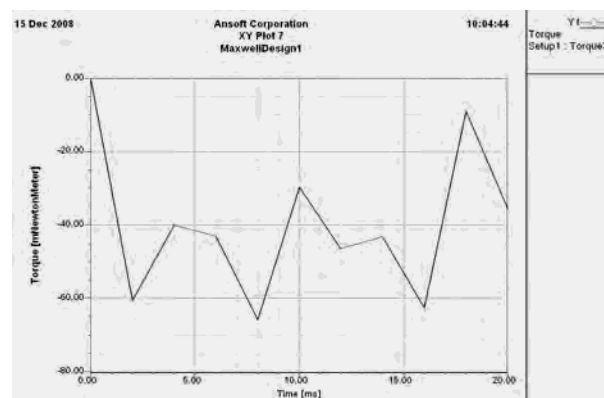


Figure 14. Torque in x-direction

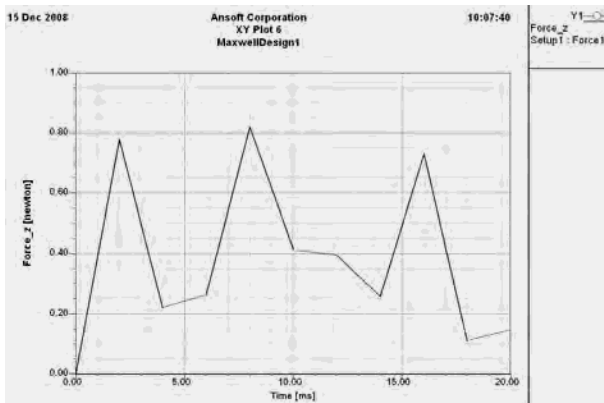


Figure 15. Force in z-direction

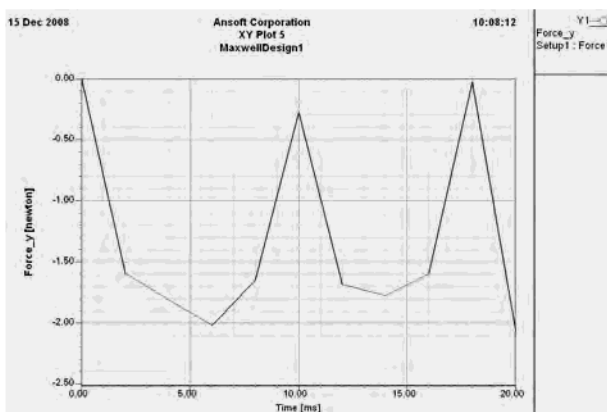


Figure 16. Force in y-direction

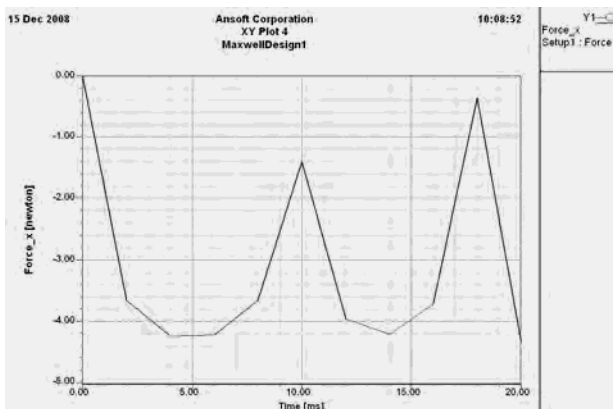


Figure 17. Force in x-direction

5. Conclusions

A method for the analysis of the magnetic force and the torque in a brushless DC motor has been presented from the finite element method and Maxwell stress tensor, so that the characteristics of the magnetic force and the torque can be predictable. Shear force existing in a small air gap produces the torque. The permanent magnet and the teeth geometry produces the reluctant torque, which increases the magnetic field of the teeth corner with the

direction to move the rotor to the equilibrium position. The commutating torque is produced by the interaction of the permanent magnet and the current which increases the magnetic field concentration of the teeth corner in the moving direction and decreases it in the opposite direction and the simulation software has analyzed nicely the performance of the brushless DC motor in the transient state.

REFERENCES

- [1] M. Marinescu and N. Marinescu, "Numerical computation of torques in permanent magnet motors by Maxwell stresses and energy method," *IEEE Transactions on Magnetics*, Vol. 24, No. 1, pp. 463–466, 1988.
- [2] J. Mizia, K. Adamiak, A. R. Eastham, and G. E. Dawson, "Finite element force calculation: Comparison of methods for electric machine," *IEEE Transactions on Magnetics*, Vol. 24, No. 1, pp. 447–450, 1988.
- [3] N. Boules, "Prediction of no-load flux density distribution in permanent magnet machines," *IEEE Transactions on Industry Applications*, Vol. IA-21, No. 3, pp. 633–643, 1985.
- [4] J. C. Sabonnadiere, A. Foggia, J. F. Imhoff, G. Reyne, and G. Meunier, "Spectral analysis of electromagnetic vibrations in DC machines through the finite element method," *Digests of the 1989 IEEE Intermag Conference*, P. Ec-07, 1989.
- [5] Y. Lefevre, B. Davat, and M. Lajoie-Mazenc, "Determination of synchronous motor vibrations due to electromagnetic force harmonics," *IEEE Transactions on Magnetics*, Vol. 25, No. 4, pp. 2974–2976, 1989.
- [6] B. S. Rahman and D. K. Lieu, "The origin of permanent magnet induced vibration in electric machines," *ASME Journal of Vibration and Acoustics*, Vol. 113, No. 4, pp. 476–481, 1991.
- [7] G. H. Jang and D. K. Lieu, "Vibration reduction in electric machine by magnet interlacing," *IEEE Transactions on Magnetics*, Vol. 28, No. 5, pp. 3024–3026, 1992.
- [8] G. H. Jang and D. K. Lieu, "Vibration reduction in electric machine by interlocking of the magnets," *IEEE Transactions on Magnetics*, Vol. 29, No. 2, pp. 1423–1426, 1993.
- [9] P. Kurrone, "Torque vibration model of axial-flux surface-mounted permanent magnet synchronous machine," *Dissertation, Acta Universitatis Lappeenrantaensis 154*, ISBN 951-764-773-5, pp. 123, 2003.
- [10] P. Salminen, "Fractional slot permanent magnet synchronous motors for low speed applications," *Dissertation, Acta Universitatis Lappeenrantaensis 198*, Finland, pp. 150, 2004.
- [11] T. Heikkilä, "Permanent magnet synchronous motor for industrial applications-analysis and design," *Dissertation, Acta Universitatis Lappeenrantaensis 134*, ISBN 951-764-699-2, pp. 109, 2002.
- [12] H. Woodson and J. Melcher, "Electromechanical dynamics, Part II: Fields, forces, and motion," *The Robert E. Krieger Publishing Company*, New York, pp. 445–447, 1985.

Ion Exchange Softening and Alkalization Treatment for Zerodischarge of Circulating Cooling Water

Huiming Zeng¹, Jiuyang Lin^{1*}, Chunsong Ye¹, Lihui Tong¹, Xiaolan Chen¹, Fei Yu¹

¹School of Power and Mechanical Engineering, Wuhan University, Wuhan, China, *Corresponding author.
Email: linjiuyang@126.com

Received January 8th, 2009; revised January 31st, 2009; accepted February 20th, 2009.

ABSTRACT

In order to solve the problems including pipe corrosion, scaling and microbial growth, which severely threat safe operation of circulating cooling water system, this paper proposes ion exchange softening and alkalization process to solve these problems and carries out a series of studies to study the feasibility of ion exchange softening and alkalization process in the simulation process of circulating cooling water system. The studies include product water quality of ion exchange softening and alkalization process, effect on the performance of carbon steel and brass, and the inhibition that suppresses microbial growth. The results indicate that ion exchange softening and alkalization process is feasible to prevent the circulating cooling water system from scaling, pipe corrosion, and microbial growth without any other chemicals. Thus circulating cooling water system can achieve zerodischarge of wastewater.

Keywords: Ion Exchange Softening and Alkalization, Circulating Cooling Water, Zerodischarge

1. Introduction

Circulating cooling water system is widely used in industrial process and central air conditioning system because of its high water conversation efficiency and rejection of thermal pollution of receiving water compared to once-through cooling water system [1]. However, circulating cooling water system has three major problems including pipe corrosion, scaling and microbial growth.

Generally speaking, the general method to solve the three problems is to add chemicals such as scale inhibitor, corrosion inhibitor, and microorganism inhibitors, which can effectively control pipe corrosion, scaling and microbial growth to the circulating cooling water, but the prevalent method brings some disadvantages including the discharge and disposal of harmful chemicals and high operation cost. Currently the researches on developing the environment-friendly chemicals with synergistic effects and high efficiency become a hotspot [2,3]. At the same time, the physical methods such as high frequency electromagnetic, electrostatic, and ultrasonic treatment, are also developing. However, neither chemical methods nor physical methods can absolutely solve these problems without any harmful impact on the water environment.

In order to solve these tough problems, this paper puts forward an innovative process, ion exchange softening and alkalization process, to transform the hardness and the corrosive anions into sodium bicarbonate to maintain the pH value of sodium bicarbonate solution in the fixed range and protect the circulating cooling water system from scaling, pipe corrosion and microbial growth.

2. Principle of Ion Exchange Softening and Alkalization Process

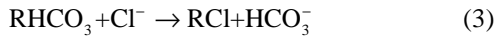
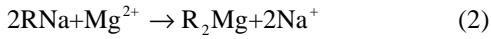
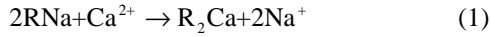
2.1 Description of Ion Exchange Softening and Alkalization Process for Circulating Cooling Water System

Figure 1 shows the schematic diagram of the facility for circulating cooling water system consisting of ion exchange system, a circulating water loop and a cooling tower. Ion exchange softening and alkalization process is used for circulating cooling water softening and alkalization treatment. Sodium form strong acidic resin and bicarbonate form strong basic resin are used to remove the hardness and corrosive anions including sulfate and chloride, transform the ions into sodium bicarbonate, and alkalinize product water of ion exchanger. The circulating loop and cooling tower are used to simulate the operation of circulating cooling water system.

2.2 Ion Exchange Softening and Alkalization System

Ion exchange softening and alkalization process uses ion exchange resin as a method for water softening and alkalization treatment. During the ion exchange process, strong acidic sodium form ion exchange resin is used as softener to remove divalent cations, especially hardness including calcium ion and magnesium ion. Then the effluent of the cation exchanger in sodium form passes through the anion exchanger in bicarbonate form, so the effluent of ion exchanger mainly contains sodium ion,

bicarbonate ion and the other ions including calcium ion, magnesium ion, chloride ion, sulfate ion are trace. The general bicarbonate-chloride anion exchange reaction and sodium-calcium or sodium-magnesium cation exchange reaction are shown below.



2.3 The Open Equilibrium State of Carbonation Solution

In circulating cooling water system, circulating cooling water exchanges heat with the atmosphere in cooling tower and it is vaporized partly and concentrated. Carbon dioxide gas in the atmosphere contacts with cooling water fully. When concentration of dissolved carbon dioxide is in line with Henry's law which is applicable to carbon dioxide equilibrium between atmosphere and liquid, the aqueous and atmosphere phases reach the equilibrium state after the spray cooling process in the cooling tower, Henry's law is expressed in Equation 4.

$$C_{CO_2} = K_H \cdot P_{CO_2} \quad (4)$$

The carbonate system controls the pH value of solution. The chemical species of solution that compose the carbonate system include gaseous carbon dioxide, aqueous carbon dioxide, carbonic acid, bicarbonate and carbonate. The presence of carbonate, bicarbonate, and hydroxyl ions accounts for essentially all of the alkalinity, so the alkalinity greatly influences the equilibrium pH value of the carbonate solution. The relation between equilibrium pH value in theory and total alkalinity in solution is expressed in Equation 5.

$$pH = -\lg \frac{(K_w + C_{CO_2} \cdot K_1) + \sqrt{(K_w + C_{CO_2} \cdot K_1)^2 + 8 \cdot B \cdot C_{CO_2} \cdot K_1 \cdot K_2}}{2 \cdot B} \quad (5)$$

The equilibrium pH values of the solutions with different alkalinities at different temperatures are showed in Figure 2. Figure 2 indicates that the equilibrium pH value of solutions rises as the alkalinity and temperature rise.

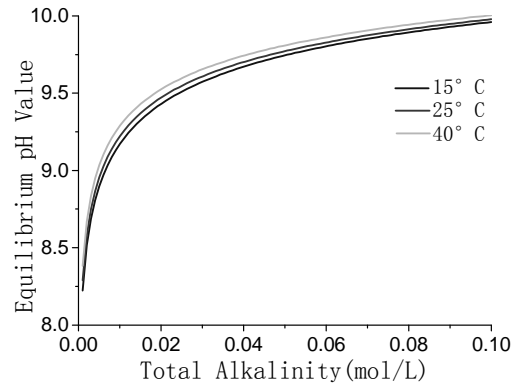


Figure 2. The relation between pH value and total alkalinity

2.4 Principle of Anti-Scale Corrosion Inhibition and Suppression of Microbial Growth

Ion exchange softening and alkalization process removes the hardness mainly including calcium ion and magnesium ion, and the corrosive anions such as sulfate and chloride, transforms the ions into sodium bicarbonate and maintains the pH value of sodium bicarbonate solution in the fixed range, so the process can effectively prevent the circulating cooling water system from scaling. From the Pourbaix diagram, we can learn that iron and copper can form a passive and compact oxide coating on the surface of metal pipe in the pH value range from 8.9 to 13.0 and from 8.6 to 10.0, respectively. And for copper pipe, it can form a protective passive coating in the optimal pH value range from 7.60 to 8.95 at low conductivity [4]. So it's possible to control the pH value of solution to prevent the metal from corrosion.

To continue to grow properly, an organism in the circulating cooling water must have a source of carbon and energy. In addition, elements such as nitrogen, phosphorus, and trace elements including sulfur, potassium, calcium, and magnesium must be available. Ion exchange softening and alkalization process cuts off the nutrition sources such as nitrogen and phosphorus which are essential for cell synthesis of microorganism. So, the ion exchange process can suppress microbial growth for circulating cooling water system.

3. Experimental Studies

3.1 Effluent Quality of Ion Exchange Softening and Alkalization Process

The raw water which comes from Yangtze River in China firstly passes through strong acidic sodium form ion exchange resin for softening to remove the hardness, and then the effluent of the cation exchanger in sodium form passes through the anion exchanger in bicarbonate form for the removal of corrosive anions such as sulfate and chloride. The qualities analyses of the raw water and effluent of ion exchanger are shown in Table 1. Table 1 indicates that the ion exchange process can removes all of the hardness and corrosive anions and transforms the ions into sodium bicarbonate. However, the pH value falls from 7.5 to 6.8.

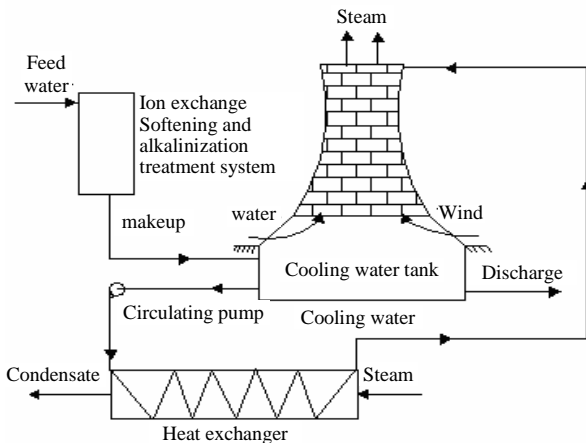


Figure 1. Schematic of ion exchange softening and alkalization for circulating cooling water system

3.2 Test Results of Carbonate Equilibrium

The equilibrium pH value of bicarbonate solution is influenced by the total alkalinity of solution, and the equilibrium pH value of solution rises as the alkalinity rises, so it is feasible to control the pH value by adjusting the alkalinity of solution. The relation between theoretical and measured equilibrium pH value in different alkalinities is showed in Figure 3. Figure 3 illustrates that the measured pH value approximates to the theoretical equilibrium pH value. Therefore, the carbonate solution is able to obtain gas-liquid equilibrium state.

3.3 Pilot Test of Circulating Cooling Water System

The pilot test flow sheet of ion exchange softening and alkalization treatment for circulating cooling water system are illustrated in Figure 4. In the study of circulating cooling water system, part of circulating water after ion exchange softening and alkalization treatment sprays, the other part of circulating cooling water goes back to cooling water tank by bypass. In the circulating cooling water system, when the cooling water sprays and contacts with

Table 1. Quality analysis of the raw water and effluent

Items	Ca ²⁺ (mol/L)	Mg ²⁺ (mol/L)	Na ⁺ (mol/L)	Cl ⁻ (mol/L)	SO ₄ ²⁻ (mol/L)	HCO ₃ ⁻ (mol/L)
Raw Water	9.1E-4	3.5E-4	7.1E-4	5.2E-4	4.1E-4	2.0E-3
Effluent	0	0	3.3E-4	0	0	3.3E-3

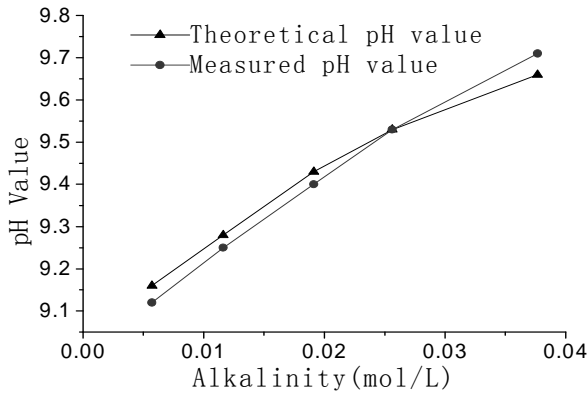


Figure 3. The comparison of measured pH value and theoretical pH value in different alkalinity

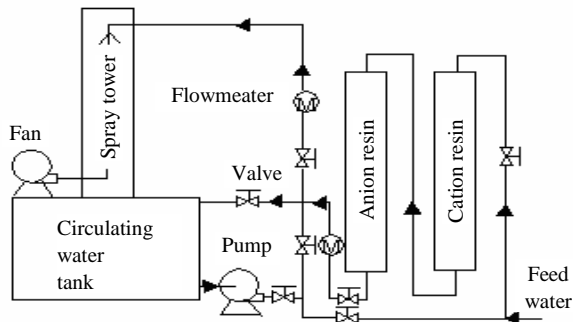


Figure 4. Schematic of the assimilation of circulating cooling water system

carbon dioxide gas in the atmosphere fully, the pH value of cooling water is increasing until carbonate solution obtains the gas-liquid equilibrium. The relation between concentration of hydrogen ion of circulating cooling water and the duration, T , of aeration is showed in Equation 6.

$$T = -\frac{V}{Q} \cdot \left\{ \ln \left(1 - \frac{(C-D) \cdot Q \cdot K_G}{\left(\frac{C}{K_H \cdot 55.56} - P_{CO_2} \right) \cdot A} \right) \right\} \quad (6)$$

$$C = \frac{B \cdot [H_i^+]^2 - K_w \cdot [H_i^+]}{2 \cdot K_1 \cdot K_2 + K_1 \cdot [H_i^+]} \quad (7)$$

$$D = \frac{B \cdot [H^+]^2 - K_w \cdot [H^+]}{2 \cdot K_1 \cdot K_2 + K_1 \cdot [H^+]} \quad (8)$$

The variation trends of the measured pH value of circulating water are showed in Figure 5. Figure 5 indicates that the value of circulating water rises as the duration of aeration increases, and measured pH value shows the same variation trends as the theoretical value. When the spray flow rate is 400 L/h and the volume of circulating water is 175.6 L. It takes 2 hour for the circulating water to keep pH value stable regardless of the initial pH value and total alkalinity of circulating water. So for an open circulating cooling water system, the pH value can be controlled accurately, it takes the fixed time for circulating water to maintain the pH value stable, and the theoretical mathematic model can be adopted to predict the pH value of circulating cooling water system.

3.4 Corrosion Test of Iron and Brass in Open Carbonate Equilibrium System

In order to studies anti-corrosion performance of carbon steel and brass in equilibrium carbonate solution with different alkalinities, the corrosion tests are carried out. During the tests, static weight loss measurement and

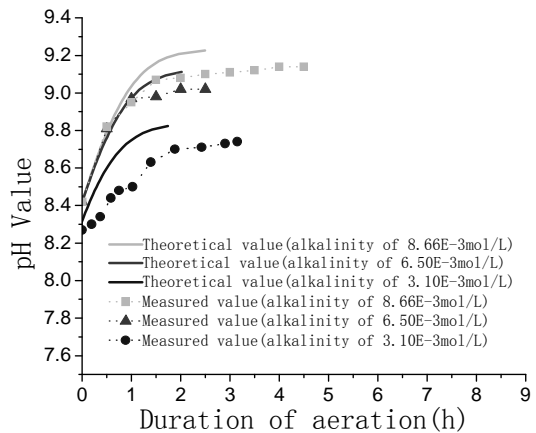


Table 5. Tendency of the variation of the pH value of solution

electrochemical methods including polarization curve and Electrochemical Impedance Spectroscopy (EIS) are adopted. In order to study the performance of passive coating formation of brass, the kinetics experiments of passive coating formation are conducted. Figure 6 shows the corrosion rate of brass by weight loss measurement. Figure 7 illustrates the corrosion current density of carbon steel and brass in carbonate solution with different alkalinities. Figure 8 shows Nyquist Plots of carbon steel in carbonate solution with different alkalinities. Figure 9 and Figure 10 show Bode Plots and Nyquist Plots of kinetics of passive coating formation of brass, respectively.

Figure 6 indicates that corrosion rate of brass in bicarbonate solution with different alkalinities is below 5.0E-3 mm/a, and it means that the bicarbonate solution has good performance on corrosion inhibition. Figure 7 indicates that the corrosion current density of brass rises as the alkalinity of bicarbonate solution rises when the alkalinity is below 3.0E-2 mol/L, and brass has the lowest corrosion current rate when the alkalinity is 3.0E-2 mol/L. Figure 7 and Figure 8 show the same result that when the alkalinity of carbonate solution is 3.0E-2 mol/L, carbon steel has the lowest corrosion current density. Figure 9 and Figure 10 illustrate that firstly the surface of brass forms the compact oxide coating consisting of cuprous oxide, and then the cuprous oxide is transformed into copper oxide by oxidation, when the oxide coating consisting of cuprous oxide forms, it can maintain stable and prevent the brass from corrosion.

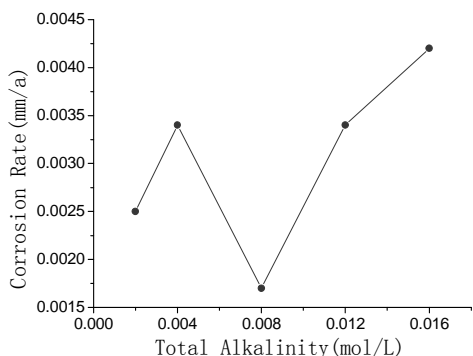


Figure 6. Corrosion rate of brass in bicarbonate solution with different alkalinities

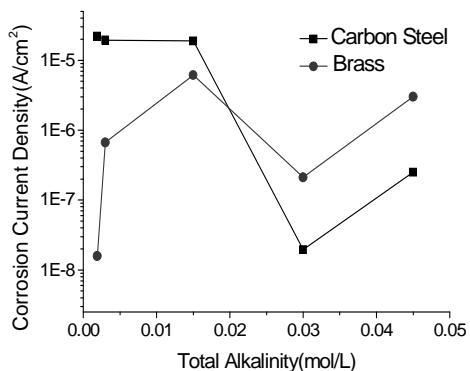


Figure 7. Corrosion current density of carbon steel and brass in bicarbonate solution with different alkalinities

3.5 Microbial Growth Test

Ion exchange softening and alkalinization process can remove calcium ion, magnesium ion, trace elements and other nutrition resource such as inorganic nitrogen and phosphorus which are essential for microbial growth. However, the circulating cooling water after softening and alkalinization treatment provides carbon resource for the microorganism. So it is necessary to study the influence factors of microorganism.

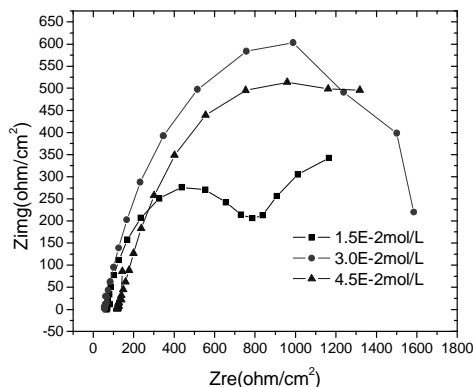


Figure 8. Nyquist plots of carbon steel in carbonate solution with different alkalinities

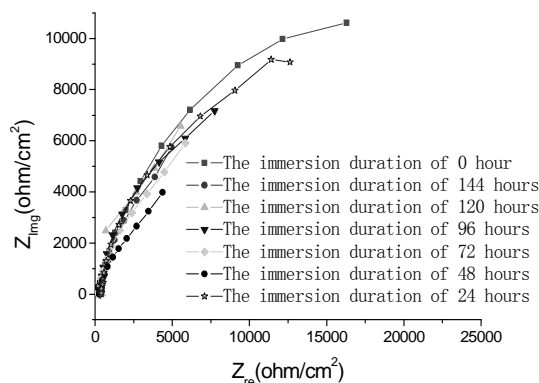


Figure 9. Nyquist Plots of kinetics of passive coating formation of brass in bicarbonate solution with different alkalinities

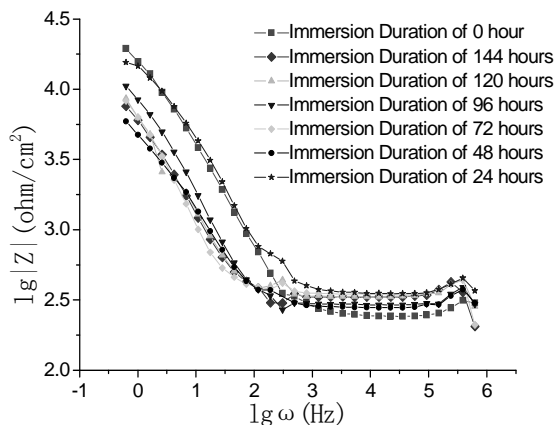


Figure 10. Bode plots of carbon steel in bicarbonate solution with different alkalinities

Table 2. Microbial growth test in different conditions

Number	Item	Alkalinity (mol/L)	Glucose (g/L)	Protein (g/L)	NH ₄ Cl (g/L)	K ₂ HPO ₄ (g/L)	CaCl ₂ (g/L)	Multiple of microbial growth	Decrement of COD _{Cr} (mg/L)
1		3.3	10	5	0	1		10.76	1840
2		16.5	10	5	0	1	0	18.34	3600
3		33.0	10	5	0	1	0	14.94	4800
4		49.5	10	5	0	1	0	13.34	8160
5		16.5	10	0	3	1	0	3.27	1680
6		16.5	10	0	0	0	0	5.87	1440
7		16.5	0	5	0	1	0	6.25	1920
8		16.5	5	0	3	1	0	6.02	1520
9		16.5	0	0	3	1	0	0.71	880
10		16.5	10	5	0	1	1.5	24.33	6720
11		16.5	10	5	0	1	3.0	17.48	6080

Nomenclature

C_{CO_2}	concentration of CO ₂ in carbonate solution, mol/L
K_w	equilibrium constant for water
K_1	coefficient of first order dissociation of H ₂ CO ₃
K_2	coefficient of second order dissociation of H ₂ CO ₃
K_H	Henry coefficient, atm ⁻¹
B	total alkalinity of carbonate solution, mol/L
A	renewing speed of gas-liquid mass transfer area, m ² /h
K_G	coefficient of gas transfer, (atm·m ²)/mol
Q	flux of spraying, L/h
V	volume of circulating cooling water, L
pH _i	initial pH value of carbonate solution
P_{CO_2}	partial pressure of carbon dioxide in atmosphere, atm.
C	initial concentration of CO ₂ in carbonate solution, mol/L
D	concentration of CO ₂ in carbonate solution at any fixed pH value, mol/L

The test studies the factors including alkalinity, nitrogen, phosphorus, hardness, organic matter. Table 2 shows the test results of the microbial growth test.

Table 2 illustrates that organic matter is the main factor that controls the microbial growth, and the absence of calcium ion, magnesium ion, nitrogen, phosphorus also can suppress the microbial growth. Content of inorganic carbon has no obvious effect on microbial growth.

4. Conclusions

Ion exchange softening and alkalization process can remove hardness and corrosive anions dissolved in circulating cooling water, transform all the ions into sodium bicarbonate, and alkalize the circulating cooling water. So the process can effectively prevent the circulating cooling water system from scaling.

The pH value of circulating water after spraying can greatly approximate to the theoretical value. Corrosion test illustrates that carbon steel and brass can reach the lowest corrosion rate in the bicarbonate solution with total alkalinity of 3.0E-2 mol/L. To optimize the operation condition of circulating cooling water system and maintain the alkalinity of circulating cooling water is an

crucial way to prevent the circulating cooling water system from corrosion. And maintain the alkalinity of carbonate solution in the level of 3.0E-2 mol/L, the concentration factor of circulating cooling water system can reach up to 15, ion exchange softening and alkalization process can improve the cooling water usage efficiency.

Microbial growth test indicates that organic matter is the main factor to influence the microbial growth, and the absence of other nutrition source such as calcium ion, magnesium ion, nitrogen, phosphorus also can affect the microbial growth. And ion exchange softening and alkalization process can remove most of organic matter and maintain the low content of organic matters and effectively suppress the microbial growth.

Therefore, ion exchange softening and alkalization process is a feasible and effective method to solve the problems of pipe corrosion, scaling, and microbial growth, improve usage efficiency of cooling water, achieve zerodischarge of wastewater and converse water resource.

5. Acknowledgement

The authors would like to thank the anonymous reviewer for their good suggestions.

REFERENCES

- [1] J. K. Kim and R. Smith, "Cooling water system design," Chemical Engineering Science, Vol. 56, No. 12, pp. 3641-3658, 2001.
- [2] F. Ziegler, "State of the art in sorption heat pumping and cooling technologies," International Journal of Refrigeration, Vol. 25, No. 4, pp. 450-459, 2002.
- [3] M. Saremi, C. Dehghanian, and M. Mohammadi Sabet, "The effect of molybdate concentration and hydrodynamic effect on mild steel corrosion inhibition in simulated cooling water," Corrosion Science, Vol. 48, No.6, pp. 1404-1412, 2006.
- [4] C. S. Ye, J. Zhang, Q. Qian, and S. P. Fan, "Study on the tubo-generator inner cooling water treated by ion-exchange micro-basification," China, Journal of Industrial water treatment, Vol. 6, pp. 17-19, 2004.

Reduction of Cogging Torque in Permanent Magnet Flux-Switching Machines

Yu Wang¹, Jianxin Shen^{1*}, Weizhong Fei², Zongxi Fang¹

¹College of Electrical Engineering, Zhejiang University, Hangzhou, 310027, China, ²Department of Aerospace Power and Sensors, Defence College of Management and Technology, Cranfield University, Shrivenham SN6 8LA, United Kingdom.
 Email: wangyu88207028@163.com

Received January 18th, 2009; revised February 5th, 2009; accepted February 20th, 2009.

ABSTRACT

Permanent magnet flux-switching machine (PMFMSM) is a relatively new structure. Available literatures mainly focused on its general design procedure and performance analysis. In this paper, Finite Element Method (FEM) is taken to analyze various design techniques to reduce the cogging torque in a prototype 12/10-pole PMFMSM.

Keywords: Permanent Magnet, Flux-Switching Machines, FEM

1. Introduction

The permanent magnet flux-switching (PMFMSM) machine is a relatively new type of electric motor. It has both windings and magnets in stator and it is a combination of switched reluctance motor (SRM) and the inductor alternator [1]. Recent research has revealed that the PMFMSM has the advantages of high power/torque density, high efficiency, and high flux-weakening capability. However, the available papers mainly focused on general design procedure [2,3,4,5,6], and performance analysis [7,8,9,10]. Due to the unique structure, the cogging torque in the PMFMSM which results from the interaction of the stator permanent magnets with the rotor teeth is relatively high comparing with other types of PM motors, producing vibration and acoustic noise and deteriorating motor performance.

In this paper, FEM is taken to analyze various design techniques to reduce the cogging torque in a prototype 12/10-pole PMFMSM.

2. Factors Influencing Cogging Torque

2.1 Motor Model

Figure 1 shows the cross-section of a 3-phase 12/10-pole PMFMSM. It has 10 poles teeth on rotor which is the same as a SRM rotor, and 12 poles on stator. Each stator pole has two iron teeth with a magnet sandwiched between them. The magnets are tangentially magnetized with opposite direction in any adjacent magnets. Moreover, each stator pole is wound around with a concentrated coil, and each phase has 4 coils. Table I gives the specification of the PMFMSM studied in this paper.

2.2 Cogging Torque Calculation

Cogging torque is due to energy variation within a motor

as the rotor rotates, even if there is no current in windings. Since the energy variation in magnets and iron is negligible compared to that in air, cogging torque for a conventional inner-rotor surface-mounted PM brushless motor can be expressed as follows [11]:

$$T(\alpha) = -\frac{\partial W(\alpha)_{airgap}}{\partial \alpha} \quad (1)$$

$$= \frac{L_s \pi}{4\mu_0} (R_s^2 - R_m^2) \cdot \sum_{n=0}^{\infty} n N_L G_{nN_L} B_{nN_L} \sin n N_L \alpha$$

where L_s , μ_0 , R_s , R_m , α are the stack length, air permeability, stator bore radius, magnet outer radius and rotation angle of rotor, respectively; G_{nN_L} , B_{nN_L} are the corresponding Fourier coefficients of relative airgap permeance function and flux density function; N_L is the least common multiple of the number of magnets and the number of slots. The fundamental cycle of the cogging torque is $2\pi/N_L$.

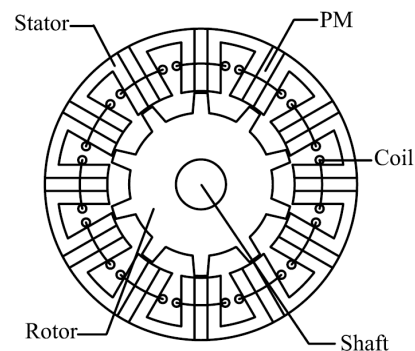


Figure 1. Topology of PMFMSM

Table 1. Specification of the PMFSM

Item	Value
Stator pole/rotor pole	12/10
Stator outer diameter	100mm
Rotor outer diameter	58.8mm
Airgap	0.6mm
Magnet thickness	4.2mm
Axial length	90mm

Though, Equation (1) was originally derived for the PM brushless motor, it has value of reference for the PMFSM. It reveals that the cogging torque can be reduced by controlling N_L , G_{nNL} , B_{nNL} . Therefore, various design techniques can be applied.

3. Method of Reducing Cogging Torque

3.1 Rotor Tooth-Notching

Figure 2 shows the tooth-notching on the rotor. This changes the airgap between the rotor and stator, which can effectively control the airgap permeance function. Cogging torque can be reduced by applying proper number and depth of notches. Especially, two tooth-notches allocated on the 1/3 position of the rotor tooth is the most effective, as verified by FEA results.

3.2 Rotor Tooth-Chamfering

Figure 3 shows the chamfered rotor teeth. This also modifies the airgap permeance function. It makes sure that the flux in the airgap can vary much more smoothly. FEA shows that proper chamfer radius of arc can reduce the cogging torque significantly.

3.3 Rotor Teeth-Pairing

Figure 4 shows the rotor teeth pairing technique to reduce the cogging torque. The cogging torque waveform varies with the rotor tooth width β_r . By the way of example, if the width of all rotor teeth is $\beta_r = 8^\circ$, the cogging torque has almost the same waveform as the case when the width of all rotor teeth is $\beta_r = 11^\circ$, but opposite phase. Therefore, two types of rotor teeth with different width of $\beta_r = 8^\circ$ and $\beta_r = 11^\circ$, are alternatively employed, as shown in Figure 4. The overall cogging torque can thus be significantly reduced, as verified by FEA results. Consequently, significant reduction of the cogging torque is observed.

Another way of realizing rotor teeth-pairing is to axially device the rotor stack into two parts. The width of all teeth in the first part is $r=11^\circ$, whilst that in the second part is $r=8^\circ$. The cogging torque produced on these two parts will kill each other, such that the overall cogging torque will be reduced effectively. This method will not be mentioned in the next section.

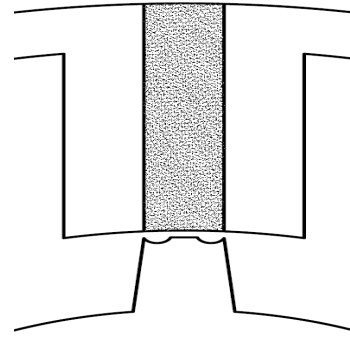
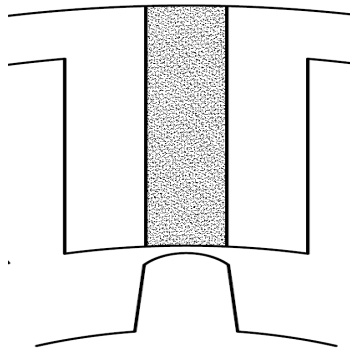
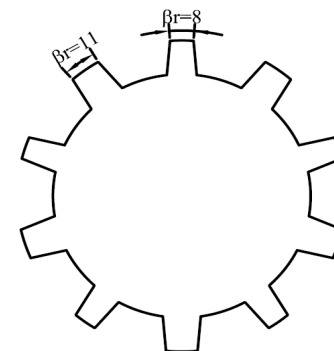
3.4 Rotor-Skewing

Skewing is the most common method to reduce the cogging torque in PM machines. In the PMFSM, the stator

has magnets, whilst the rotor is composed entirely of laminations. Therefore, skewing rotor is much more convenient in the PMFSM. In this paper, the rotor is skewed by one cogging torque cycle, viz. 6 mech-degrees. Finite Element Analysis (FEA) shows that rotor skewing can reduce the cogging torque by 95%. However, rotor-skewing also decreases the rotor saliency, and thus reduces the back-EMF and electromagnetic torque.

3.5 Magnet Thickness Optimization

It was originally recommended in [2] that the magnet thickness should be the same as that of stator teeth. However, FEA shows that it is essential to optimize the magnet thickness to reduce the cogging torque. Generally, thinner magnets will lead to lower cogging torque, but also result in lower airgap field and electromagnetic torque.

**Figure 2. Rotor Tooth-Notching****Figure 3. Rotor Tooth-Chamfering****Figure 4. Rotor Teeth-Pairing**

4. Effectiveness Analysis with FEM

In the preceding section, five design methods of reducing the cogging torque, as well as their pros and cons, have been presented. It is noted that the back-EMF may decrease when these methods are applied, therefore, the back-EMF variation should also be examined.

Figure 5 and Table 2 show the cogging torque reduction of the 12/10-pole PMFSM with various design methods. Compared with the case of the original model, the cogging torque can be reduced by 95% with the rotor-skewing technique, and by 80% or more with the rotor teeth-pairing, rotor tooth-notching and rotor tooth-chamfering techniques. Using thinner magnets can also decrease the cogging torque, by 64%, though it is not sufficiently effective.

Figure 6 shows the back-EMF waveforms with half a cycle. It is seen that the back-EMF with rotor-skewing by 6 mech-deg is almost sinusoidal, and its amplitude decreases by 5% compared with that of the original model. The back-EMF with rotor tooth-notching contains more harmonics which can deteriorate the motor performance, and its amplitude is reduced by 12% due to the increase of the equivalent airgap length. Moreover, the airgap field with rotor tooth-chamfering or thinner magnets is smoother than that in the original model, thus, the back-EMF waveforms are also close to sine-wave. However, the rotor tooth-chamfering will decrease the back-EMF, also because of the larger airgap. Furthermore, it is interesting to notice that the back-EMF amplitude with

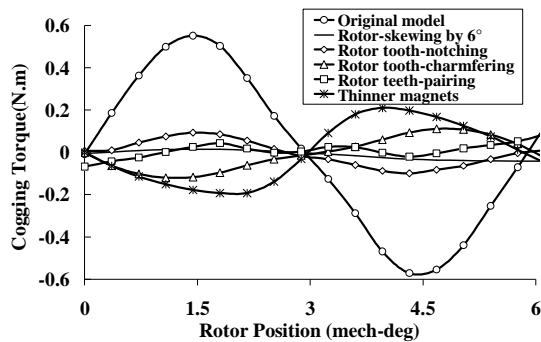


Figure 5. Cogging torque reduction with various methods

Table 2. Effectiveness of cogging torque reduction of various methods

Design Methods	Cogging Torque (Peak-to-Peak) (Nm)	Percentage to Original
Original	1.12	100%
Rotor tooth-notching	0.19	17%
Rotor tooth-chamfering	0.23	20%
Rotor teeth-pairing	0.15	13%
Rotor-skewing by 6 mech-deg	0.056	5%
Thinner magnets	0.40	36%

width, which is the same as the magnet width and the stator tooth width as well as the stator slot opening width the rotor teeth-pairing technique increases by 4%. This further proves that the originally proposed rotor tooth [2], might be unsuitable. Hence, optimization of rotor tooth width is usually essential [6].

On the other hand, the PMFSM can be driven as a sine-wave permanent magnet synchronous motor (PMSM). Thus, the effective component of the back-EMF is the fundamental. Clearly, even if the amplitude of the phase back-EMF is high, its fundamental might not be essentially high due to the influence of harmonics. Therefore, the electromagnetic torque (EM-torque) produced with sine-wave armature currents are investigated. As can be seen in Figure 7, there exist ripples in the EM-torque, partly because of the harmonics in the back-EMF, and mainly because of the motor saliency and non-sinusoidal variation of winding inductance. The average EM-torque, as well as the back-EMF amplitude, is all listed in Table 3. It is seen that the rotor-skewing technique and thinner magnets technique will keep the average EM-torque almost the same, the rotor tooth-notching technique and rotor tooth-chamfering techniques which increase the equivalent airgap length will reduce the average EM torque, whilst the rotor teeth-pairing technique can in contrast enhance the EM torque.

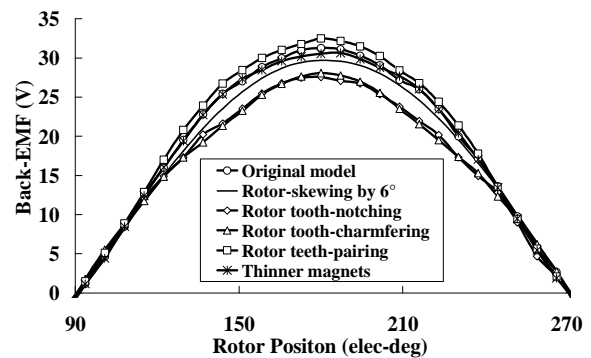


Figure 6. Back-EMF variation with various methods

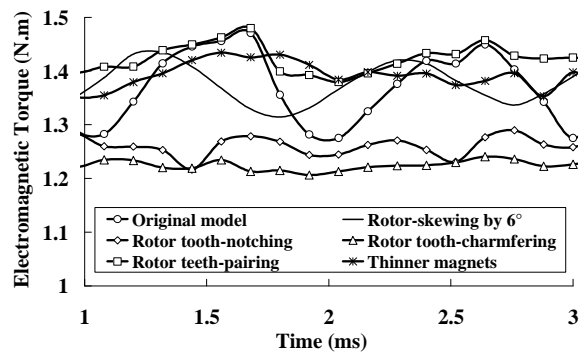


Figure 7. Electromagnetic torque variation with various methods

Table 3. Comparison of back-EMF and average torque with various methods

Design Methods	Back-EMF amplitude (V)	Average EM-Torque (N.m)
Original	31.3	1.38
Rotor-skewing by 6 mech-deg	29.7	1.37
Rotor tooth-notching	27.6	1.26
Rotor tooth-chamfering	28.1	1.23
Rotor teeth-pairing	32.5	1.42
Thinner magnets	30.6	1.39

5. Conclusions

Five design methods are presented to reduce the cogging torque in the permanent magnet flux-switching machine. FEM is taken to analyze the effects of these methods, including the cogging torque reduction and the back-EMF variation. It is proved that the rotor-skewing technique is the most effective to reduce the cogging torque and can keep the average EM-torque almost unchanged. Moreover, the rotor teeth-pairing technique can also reduce the cogging torque significantly, and meanwhile enhance the EM-torque by some degrees. These two methods are generally preferable.

REFERENCES

- [1] S. E. Rauch and L. J. Johnson, "Design principles of flux-switching alternators," *AIEE Transactions*, Vol. 74III, pp. 1261–1268, 1955.
- [2] E. Hoang, A. H. Ben Ahmed, and J. Lucidarme, "Switching flux permanent magnet polyphased synchronous machines," *EPE-97 Conference*, Trondheim, September 1997.
- [3] H. Wei, M. Cheng, J. Z. Zhang, and X. Y. Zhu, "Optimal design of flux-switching permanent magnet machine based on finite element analysis," *Electromagnetic Field Computation*, pp. 333–333, 2006.
- [4] H. Wei, M. Cheng, Z. Q. Zhu, and D. Howe, "Analysis and optimization of back-EMF waveform of a novel flux-switching permanent magnet motor," *Electric Machines & Drives Conference*, Vol 2, 3–5, pp.1025–1030, May 2007.
- [5] Y. Amara, E. Hoang, M. Gabsi, M. Lecrivain, and S. Al-lano, "Design and comparison of different flux-switch synchronous machines for an aircraft oil breather application," *Proceedings 2nd IEEE International Conference on Signals, Systems, Decision and Information Technology*, pp. 26–26, 2003.
- [6] W. Z. Fei and J. X. Shen, "Novel permanent magnet switching flux motors," *41st UPEC Conference*, New Castle, pp. 729–733, September 2006.
- [7] Y. Chen., Z. Q. Zhu., D. Howe. and Y. Y .Ye, "Starting torque of single-phase flux-switching permanent magnet motor," *IEEE Transactions on Magentics*, Vol. 42, No. 10, pp. 3416–3418, October 2006.
- [8] E. Hoang, A. H. Ben-Ahmed, and J. Lucidarme, "Switching flux permanent magnet polyphased synchronous machines," *Proceedings 7th European Conference Power Electron and Applications*, Vol. 3, pp. 903–908, 1997.
- [9] Z. Q. Zhu, Y. Pang, D. Howe., S. Iwasaki, R. Deodhar, and A. Pride, "Analysis of electromagnetic performance of flux-switching permanent magnet machines by non-linear adaptive lumped parameter magnetic circuit model," *IEEE Transactions Magnetics*, Vol. 41, No. 11, pp. 4277–4287, 2005.
- [10] W. Hua, Z. Q. Zhu, M. Cheng, Y. Pang, and D. Howe, "Comparison of flux-switching and doubly-salient permanent magnet brushless machines," *Proceedings 8th International Conference on Electrical Machines and System*, Vol. 1, pp. 165–170, 2005.
- [11] S. M. Hwang, J. B. Eom, G. B. Hwang, W. B. Jeong, and Y. H. Jung, "Cogging torque and acoustic noise reduction in permanent magnet motors by teeth pairing," *IEEE Transactions Magnetics*, Vol. 36, No. 5, pp. 3144–3146, September 2000.

Impact of Reactive Power in Power Evacuation from Wind Turbines

Asish Ranjan¹, S. Prabhakar Karthikeyan¹, Ankur Ahuja,¹ K. Palanisamy¹, I. Jacob Raglend², D. P. Kothari³

¹School of Electrical Sciences, Vellore Institute of Technology, Vellore, India-632014, ² Christian College of Engineering and Technology, Ottanchatiram, Dindugal District. India-632014, ³Vellore Institute of Technology University, Vellore, India-632014.
Email: asran@vestas.com; spk25in@yahoo.co.in; ahuja.ankur.1986@gmail.com; kpalanisamy79@yahoo.co.in; jacobraglend@rediffmail.com; dpk0710@yahoo.com; vc@vit.ac.in

Received January 31st, 2009; revised February 17th, 2009; accepted February 28th, 2009.

ABSTRACT

Application of Distributed Generation (DG) to supply the demands of a diverse customer base plays a vital role in the renewable energy environment. Various DG technologies are being integrated into power systems to provide alternatives to energy sources and to improve reliability of the system. Power Evacuation from these remotely located DG's remains a major concern for the power utilities these days. The main cause of concern regarding evacuation is consumption of reactive power for excitation by Induction Generators (IG) used in wind power production which affects the power system in variety of ways. This paper deals with the issues related to reactive power consumption by Induction generators during power evacuation. Induction generator based wind turbine model using MATLAB/SIMULINK is simulated and its impact on the grid is observed. The simulated results are analyzed and validated with the real time results for the system considered. A wind farm is also modeled and simulations are carried out to study the various impacts it has on the grid & nearby wind turbines during Islanding and system event especially on 3-Phase to ground fault.

Keywords: Distributed Generation (DG), Grid, Wind Turbines, Induction Generator, Islanding, Power Evacuation, Point of Common Connection 3 Phase to Ground Fault

1. Introduction

Wind is one of the most important resources found in nature's bounty totally free of cost and without any hazardous effects. Perhaps that is why, in this hour of energy crisis, the entire human race has diverted its attention to wind energy as a suitable alternative to the conventional sources of energy we have been using for more than a century.

Having an insight into the statistics concerning installed wind power capacity, we see that the total capacity as of today is 93,849MW (2008). India stands fourth in wind power commissioning with an installed capacity of 7844.5MW (2008). But Germany with a capacity of 22,247MW (2008) shows that the distance to be covered is still huge. Of course, it instills a hope that the future will be bright with no reliance on conventional sources of energy and wind energy forming a large chunk of the installed capacity.

There are two types of utility-scale wind turbines, fixed- and variable-speed. Fixed-speed wind turbines operate at a near constant rotor speed at all times and are directly connected to the power grid [1]. Fixed speed wind turbine which is used here for analysis operates within a very small range (around 5% of the nominal value) and in general they use a fixed shunt capacitor to provide reactive power compensation [2].

1.1 Islanding

A phenomenon which generally occurs in a network with Wind Generation in which a portion of the distribution network becomes Electrically Isolated from utility grid due to transmission system events & after disconnection, wind generator maintains supply to local loads. Islanding can be categorized as Intentional Island and Unintentional Island. Islanding is a condition in which local Distribution Generation systems continue to supply stable real power and reactive power to the local loads at a sustained voltage and frequency while the main Energy system is de-energized. An islanding condition creates a safety hazard and may cause damage to power generation and power supply facilities as a result of unsynchronized re-closure [3]. In general, after loss of the main source, the DG has to take charge of the remaining network and the connected loads; therefore, the loading condition of the DG is suddenly changed after islanding. Since the distribution networks generally include single-phase loads, it will be highly possible that the islanding changes the load balance of DG [4].

1.2 Intentional Island

Planned islanding is often called Intentional Islanding. This condition arises when a portion of the network is

separated from the rest of the network for the sake of system reliability & maintaining the safety of the network. Utility personnel monitor the islanded system continuously & it poses no problem for the utility.

During the occurrence of a system outage, when several groups of generators can go out of-step with each other, it may be desirable to have selected islands where there is a minimal mismatch between load and generation. Switching operations carried out to split the system into such self-sufficient regions is called intentional islanding.

1.3 Unintentional Island

Sudden and unpredicted islanding is termed as unintentional islanding which mainly results due to the failure of anti-islanding techniques resulting in electrical isolation of an energized portion [5]. The energized portion will continue to supply power to the loads present in the island affecting the safety concerns for the utility personnel.

A section of the grid having balanced load and generation may become isolated from the rest of the grid by a sudden opening of a switch or a circuit breaker that causes the disconnection of the feeder from the grid. A common form of disconnection would typically arise from a momentary ground fault on the feeder, which is detected by the feeder ground relay and results

in tripping of the feeder circuit breaker. Such an event is described in Figure 1. The single line to ground fault shown in the Figure1 is assumed to be transient in nature [6]. This fault could cause operation of utility breaker shown as a disconnection point suggested by the given Figure 1.

However, the transient fault may be undetectable by the DG and cause to exist after opening of the utility breaker. In this scenario, an unintentional island is formed after opening of the utility breaker. After disconnection from the grid, this island may be initially deficient in active and reactive power. The deficiency of active power is balanced by the release of kinetic energy from the rotating machinery connected to the system, and hence reduction in system frequency [6]. The deficiency of reactive power is mainly balanced by the export of reactive power from the embedded synchronous generator. An islanding event, such as described in this section, can be conveniently illustrated by a frequency and voltage versus time graph of Figure 2.

1.4 Implications of Inadvertent Islanding

Inadvertent islanding presents a number of safety, commercial, power quality, and system integrity problems [7]. In summary, the major issues are:

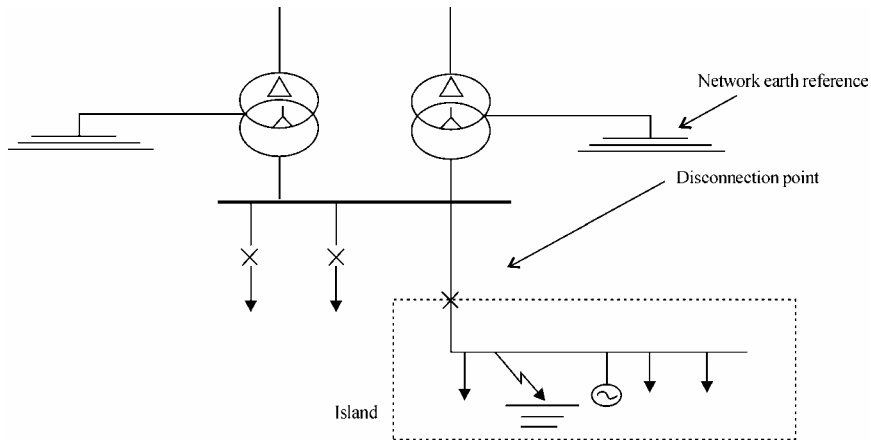


Figure 1. Ground fault disconnection

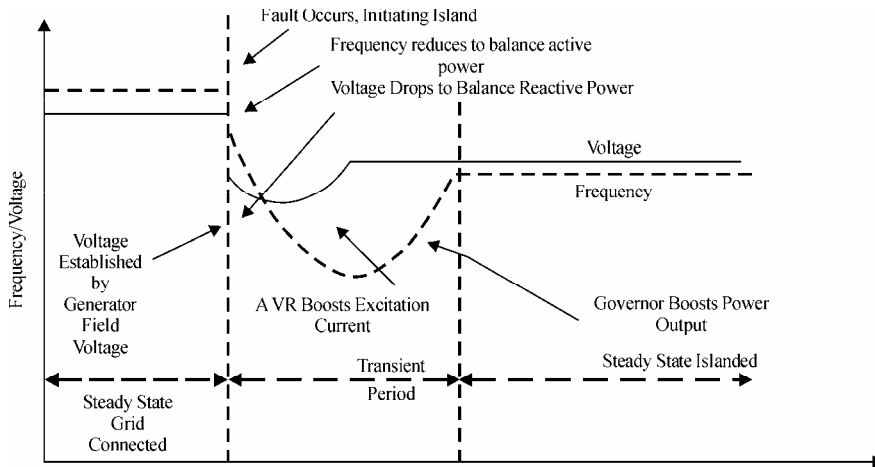


Figure 2. Voltage and frequency response

- 1) Line worker safety can be threatened by DG sources feeding a system after primary sources have been opened and tagged out.
- 2) Public safety can be compromised as the utility does not have the capability of de-energizing downed lines.
- 3) The voltage and frequency provided to other customers connected to the island are out of the utility's control, yet the utility remains responsible to those customers.
- 4) Protection systems on the island are likely to be uncoordinated, due to the drastic change in short circuit current availability.
- 5) The islanded system may be inadequately grounded by the DG interconnection.
- 6) Utility breakers or circuit reclosers are likely to reconnect the island to the greater utility system when out of phase.

2. System Configuration

The parameters used for the simulation of the above model of an Induction Generator based wind turbine are as follows:

2.1 Induction Generator

A 3-phase squirrel cage induction generator with a nominal power of 843KVA, 690V (ϕ - ϕ), 50 HZ is used for the above system with the parameters shown in Table 1.

Table 1. Induction generator parameters

Parameter	Unit	
Stator Resistance	R1	0.0045 Ω
Stator Leakage Reactance	X1	0.0513 Ω
Magnetizing Reactance	Xh	2.2633 Ω
Rotor Reactance(referred to Stator)	X'2	0.066 Ω
Rotor Resistance(referred to Stator)	R'2	0.004 Ω
Magnetizing Resistance	Rfe	83.3 Ω

2.2 Three Phase Transformer

A Y_g/Δ (D1) configuration of three phase (2-winding) transformer is used with a nominal power of 1MVA with following primary/Secondary Windings given in Table 2. Parameters used for the simulation of three phase PI section Line was given in Table 3.

2.3 Grid

A three-phase source with internal R-L impedance is used to implement a grid which is connected to the wind Generator through a T-Line & Transformer. The three phase Short-circuit Level at base voltage of 33KV is 25MVA with X/R ratio of 10.

2.4 Load

A 3-Phase resistive load of 675KW is used which is connected at the terminals of wind turbine. Simple wind farm based on fixed speed wind turbines is connected to a grid through a T-Line at Point of Common Connection (PCC).

Table 2. WG transformer parameters

Parameters	Primary Winding	Secondary Winding
Voltage (ϕ - ϕ) rms(KV)	33	0.690
Resistance(R) pu	0.0125	0.039
Inductance(L) pu	0.0125	0.039

Table 3 Parameters for PI section transmission line

Parameters	Positive Sequence	Zero Sequence
Resistance(Ω /Km)	0.1153	0.413
Inductance(mH/Km)	1.05	3.32
Capacitance(μ F/Km)	11.33	5.01

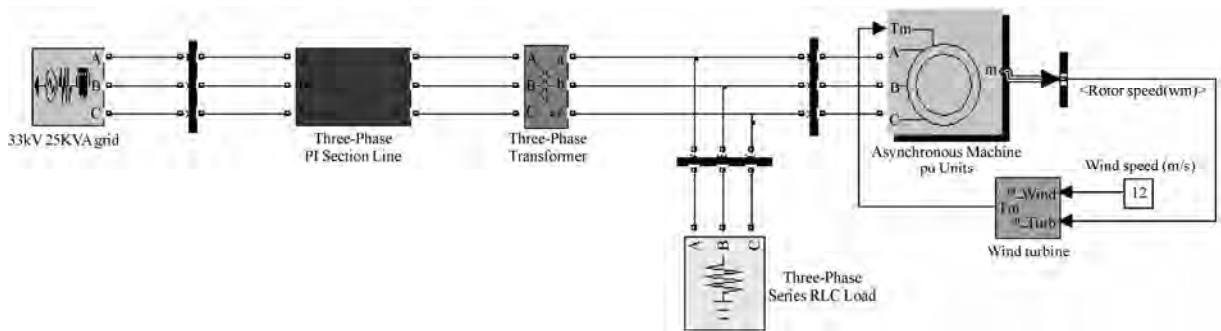


Figure 3. System configuration in SIMULINK

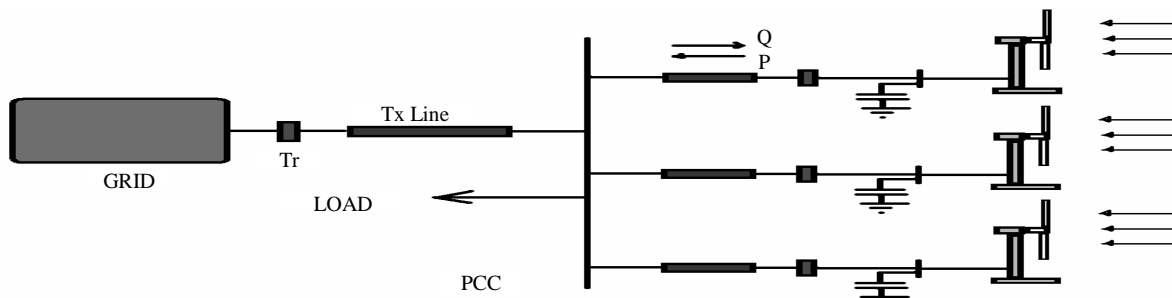


Figure 4. Outline of grid connected wind farm

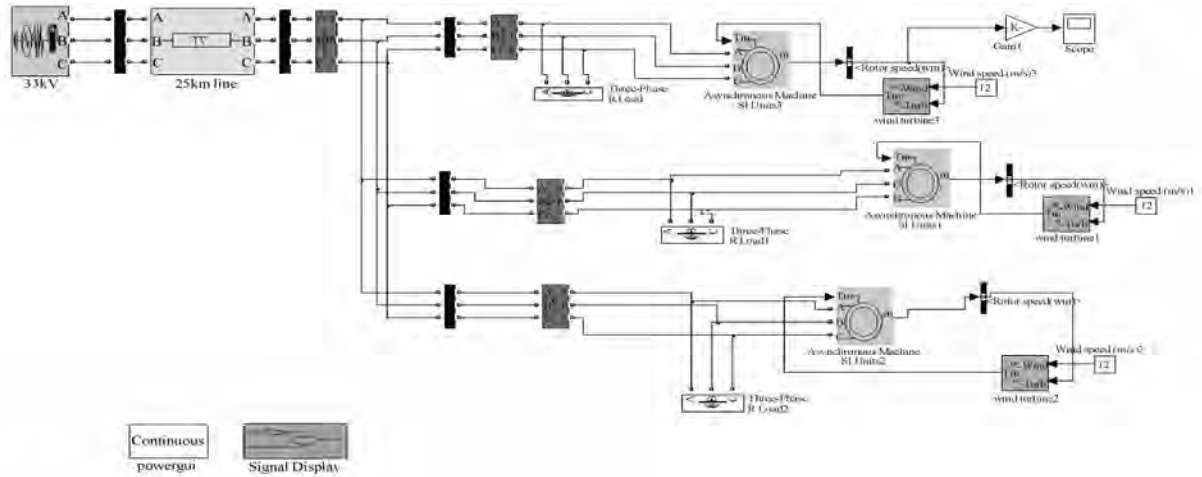


Figure 5. Wind farm connected to grid using SIMULINK

The second module of the paper deals with the Implementation of a Wind Farm & its Impact on Grid during Islanding which can be categorized as:

- 1) Wind Farm Configuration in SIMULINK.
- 2) Impact on Grid during Disconnection of a Wind Generator.

2.5 Wind Farm Configuration

A Wind Farm with three Identical Wind Turbines connected together to form a Wind farm of capacity 2.25MW is shown in the Figure 5.

In implementing a wind farm connected to a grid through a PCC needs a separate step-up Transformer at the PCC which is finally connected to the grid via Pi section T-Line. The difference between a single wind Turbine connected to a grid & a wind farm connected to grid can be seen by an additional Transformer's & Individual short transmission lines connecting each Generator to

PCC with their parameters mentioned below.

2.6 Transformer

With nominal power 10MVA a 33/66KV transformer with same parameters specified before.

2.7 T-Line

Short transmission lines connecting Individual Wind generators are of length 1 Km each with same parameters specified before.

The Islanding of a Wind turbine model is shown in Figure 6 using SIMULINK. The Impact of Disconnection of one of WG from the rest of the network is implemented here by Inserting a 3-phase breaker in series with the same WG & PCC in which switching of all the three phases from closed to open condition takes place after 1.5 Sec of operation of WG.

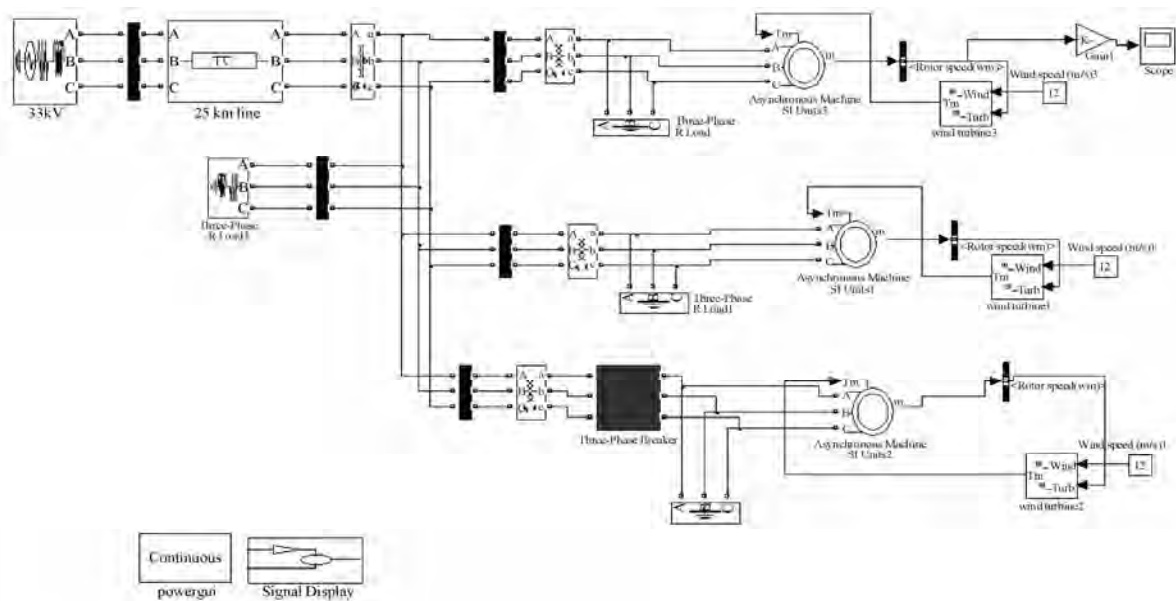


Figure 6. Islanding of a simulated wind turbine model

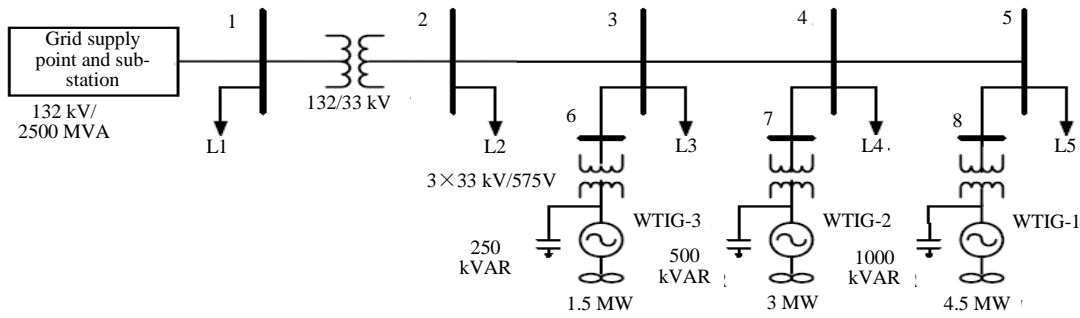


Figure 7. Network layout used for simulation [8]

The parameters for the Breaker are Transition Time: 1.5 Sec, Breaker Resistance: 0.001 Ω, Snubber Resistance: 0.000001 Ω, Snubber Capacitance: ∞.

Figure 7 is implemented in SIMULINK to Simulate Unintentional Islanding Condition.

2.8 Induction Generator

A 3-phase squirrel cage induction generator with a nominal power of 1.66MVA, 575V (φ-φ), 60 HZ is used for the above system with the parameters shown in Table 4.

A grounding Transformer is used to create a grounding point at the secondary side (Δ) of grid 47MVA transformer with $X_0=4.7 \Omega$ [8].

Table 4. Parameters for induction generator [8]

Parameter	Unit	
Stator Resistance	R1	0.004843 pu
Stator Leakage inductance	L1	0.1248 pu
Magnetizing Inductance	Lm	6.7 pu
Rotor inductance ref to Stator	L'2	0.1791 pu
Rotor Resistance ref to Stator	R'2	0.004347 pu

Table 5. Three phase transformer parameters [8]

Parameters	3-Phase 4MVA transformer (Yg/Yn)		47MVA grid side transformer Yg/Δ(D1)	
	Primary Winding	Secondary Winding	Primary Winding	Secondary Winding
Voltage (φ-φ) rms(KV)	33	0.575	132	33
Resistance(R) pu	0.025/30	0.025/30	0.08/30	0.08/30
Inductance(L) pu	0.025	0.025	0.08	0.08

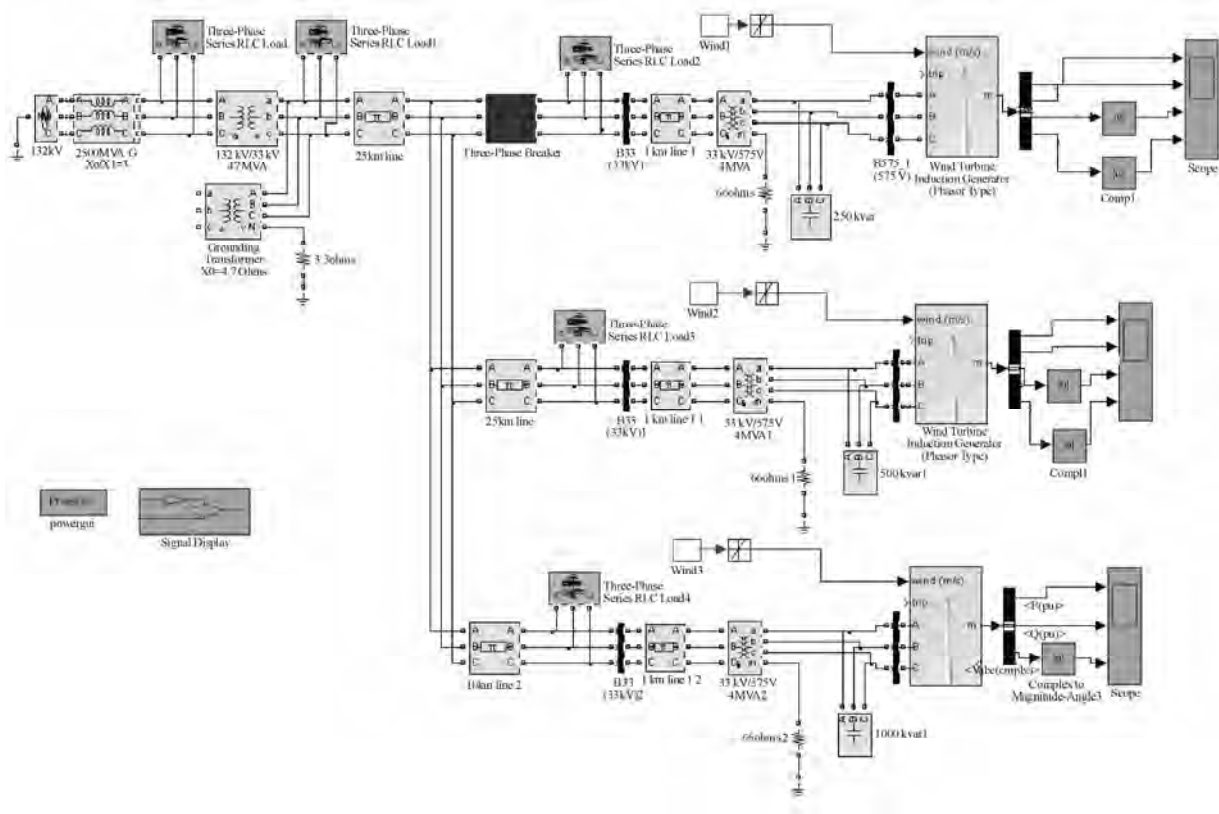


Figure 8. Simulated model for unwanted islanding

2.9 Grid

A three-phase ideal voltage source along with a 3-phase mutual inductance block is used a grid with a capacity of 2500MVA & $X_0/X_1=3$ [8].

3. Case Studies and Results

3.1 Normal Condition without any Compensation

For a Wind Farm of 2.25 MW under normal working condition, following results were obtained.

The waveform of P & Q at the Wind Generator terminals is shown in Figure 9. The waveform of P & Q at the Grid terminals are shown in Figure 10. The waveform of V, I, P & Q at the load terminals are shown in Figure 11. The loading conditions without any reactive power compensation are $Load = (750+360j)*3$, $C1=C2=C3=0$.

It is found that the requirement of reactive power by Induction generators without compensation is fulfilled by the grid which results in large deviation from the standard voltage values.

3.2 Islanding Condition

Following results were obtained under Islanding condition. The waveform of P & Q at the Wind Generator terminals are shown in Figure 12. The Frequency Response at the Wind Generator Terminal is shown in Figure 13. The waveform of V, I, P & Q at the Grid terminal are shown in Figure 14. The waveform of V, I, P & Q at the Load terminal are shown in Figure 15.

3.3 Unintentional Islanding Condition

Following results were obtained under Unintentional

Islanding condition where Islanding can be detected by conventional method.

For $P_G=1.5MW$, $Q_G=-750 KVAR$, $P_L=1.2MW$, $Q_L=20 KVAR$, $Q_C=250KVAR$.

The waveform of V, I, P & Q at islanded Wind Generator terminals are shown in Figure 16.

Table No. 6 shows the simulated results of the Voltage at Generator Terminal for the clearing time. And Table 7 shows the IEEE Standards for Interconnection system response to abnormal voltages.

From the waveform as $df/dt=1.19 HZ/Sec$, $\Delta f = 2.38HZ$, $f' = f - \Delta f = 57.62HZ$.

It is found that Islanding can be detected by the Conventional methods based on local parameters. Thereafter Islanding can be prevented in accordance with IEEE 1547 standards.

Table 6. Voltages at WG terminal ($P_L=1.2MW$)

4 SEC	6 SEC
0.961 pu	0.46 pu

Table 7. IEEE 1547 standard (for voltage)

Voltage Range (% of Base Voltage)	Clearing Time
$50 \leq V \leq 88$	2 Sec

Table 8. IEEE 1547 standard (for frequency)

WG size	Frequency range	Clearing Time
$>30KW$	$<(59.8-57)$	Adjustable 0.16s to 0.3s

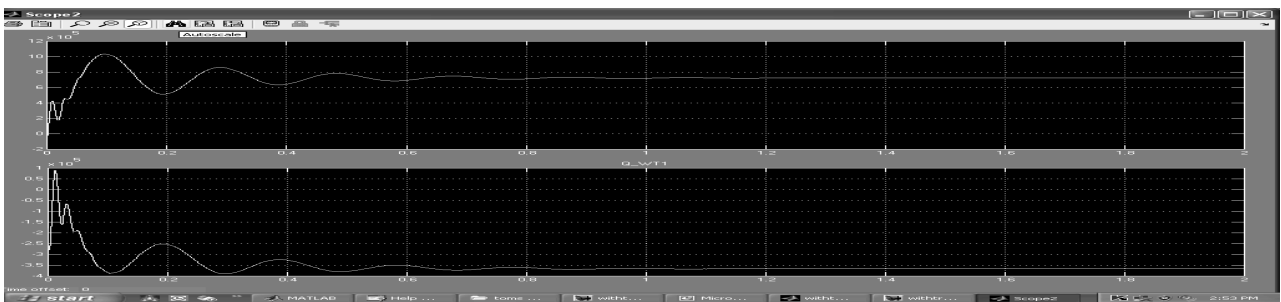


Figure 9. P & Q waveform at WG terminals

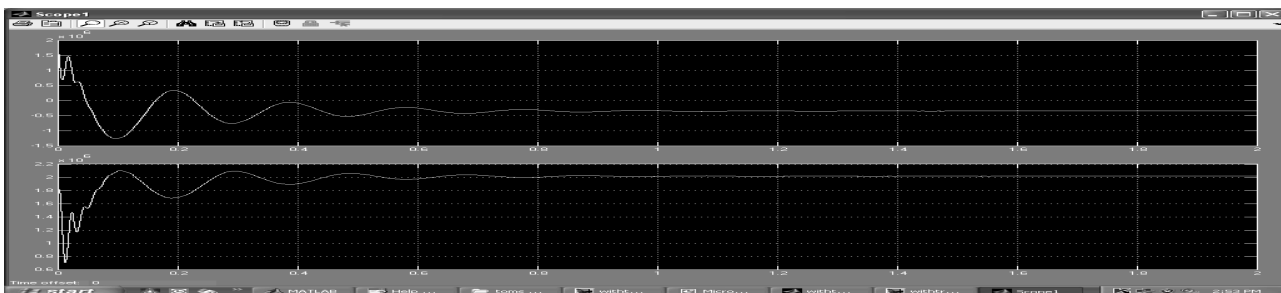


Figure 10. P & Q waveform at grid terminals

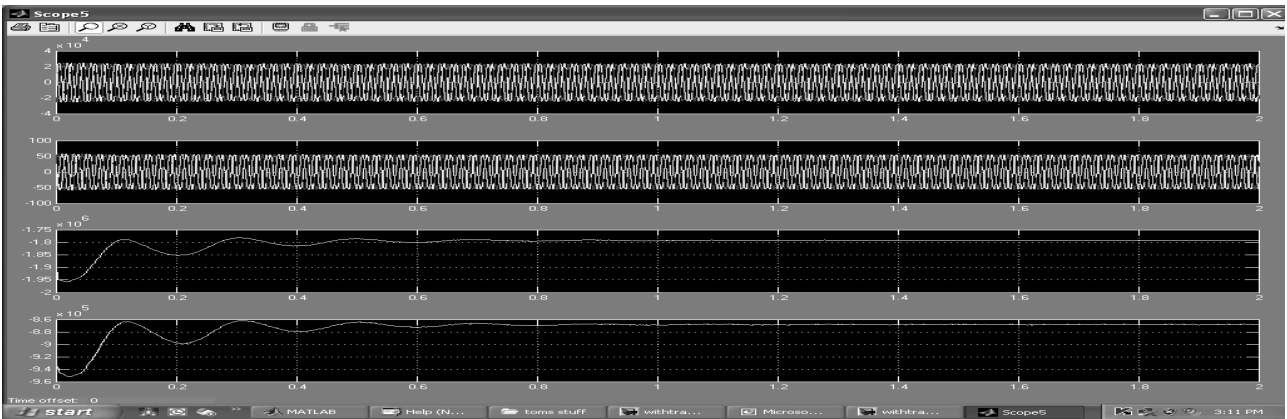


Figure 11. V, I, P & Q waveform at load end

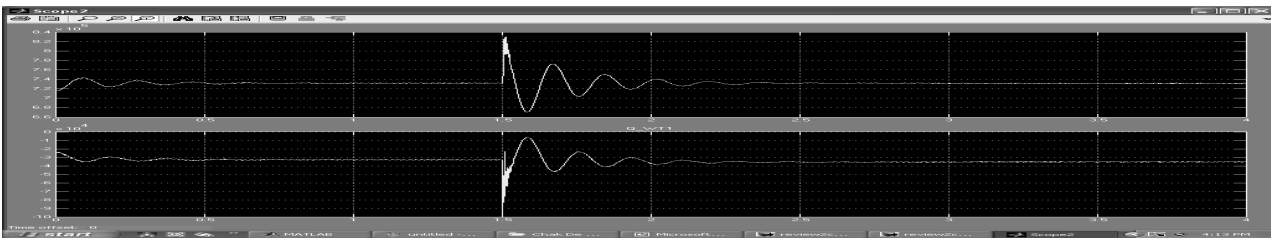


Figure 12. P & Q waveform at WG terminal during disconnection of one WG

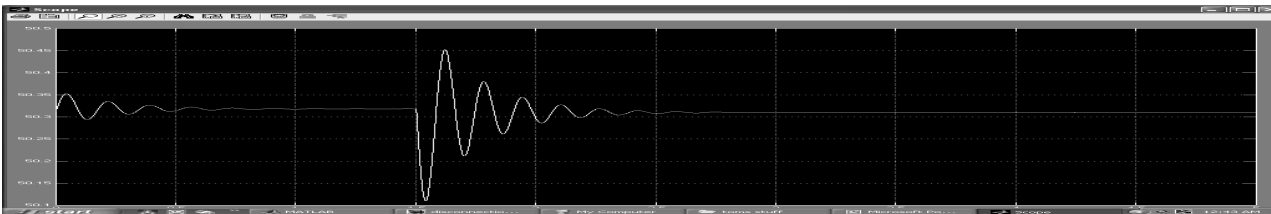


Figure 13. Frequency response at WG terminal

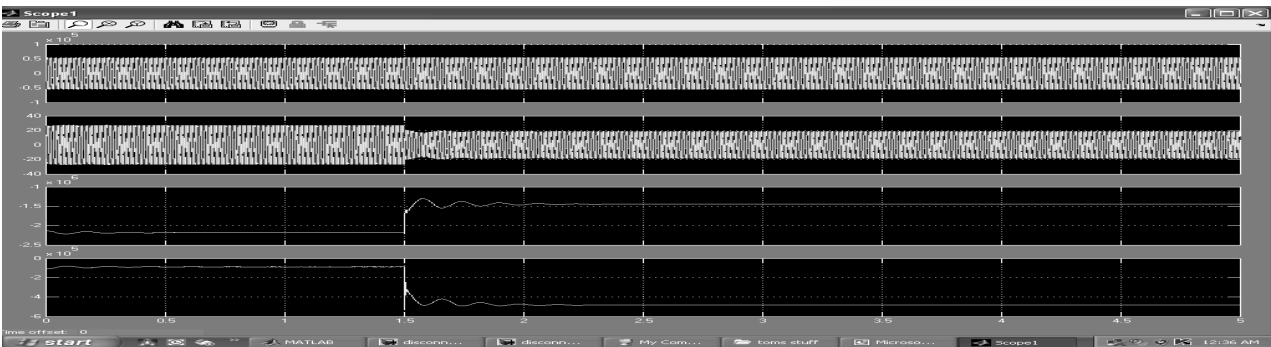


Figure 14. V, I, P & Q waveform at grid end

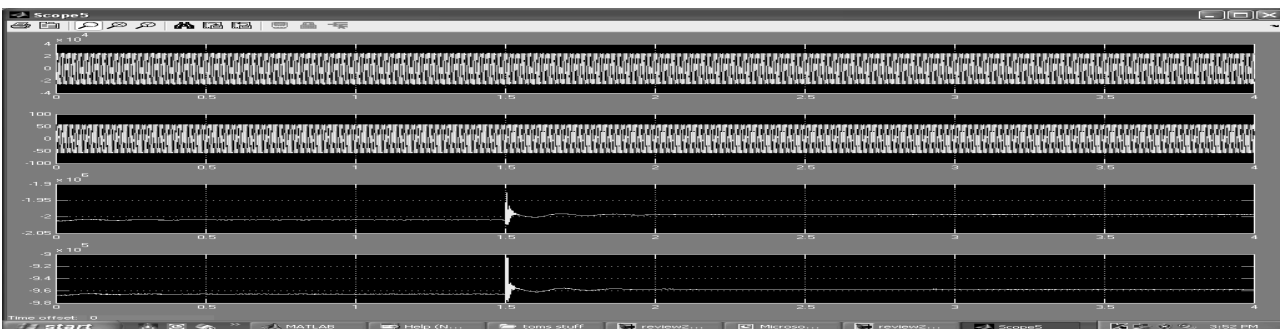


Figure 15. V, I, P & Q waveform at load terminal

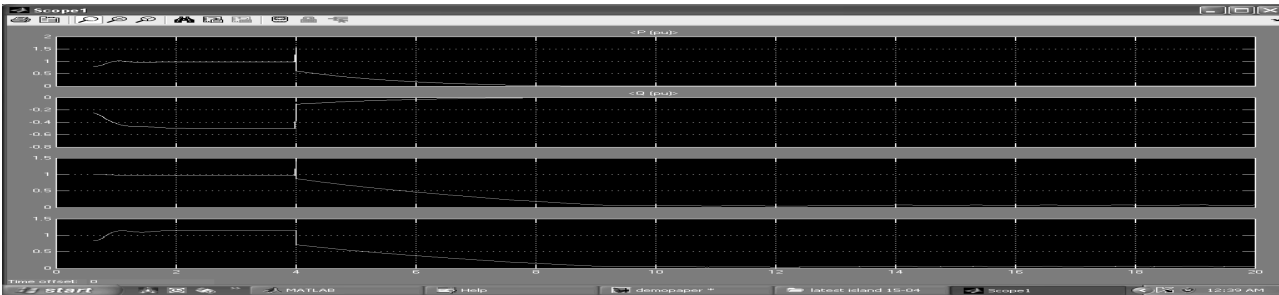


Figure 16. V, I, P, Q waveform at islanded WG end ($P_L=1.2$ MW)

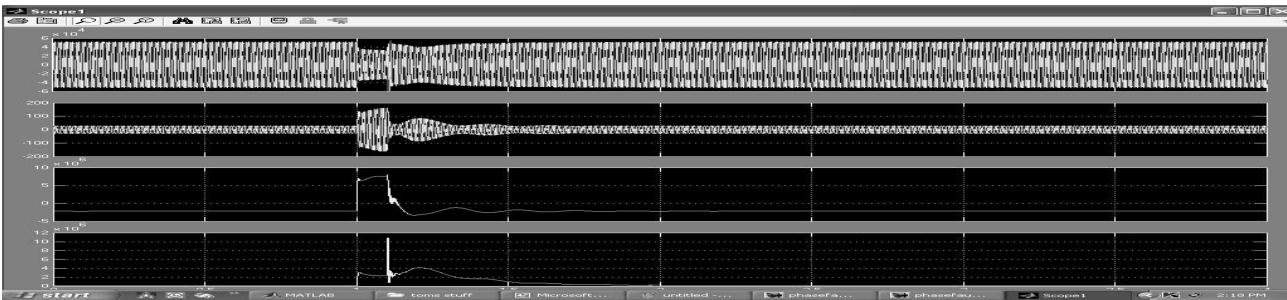


Figure 17. Waveform of V, I, P, Q at Grid terminal during 3 phase fault at $t= 1$ sec

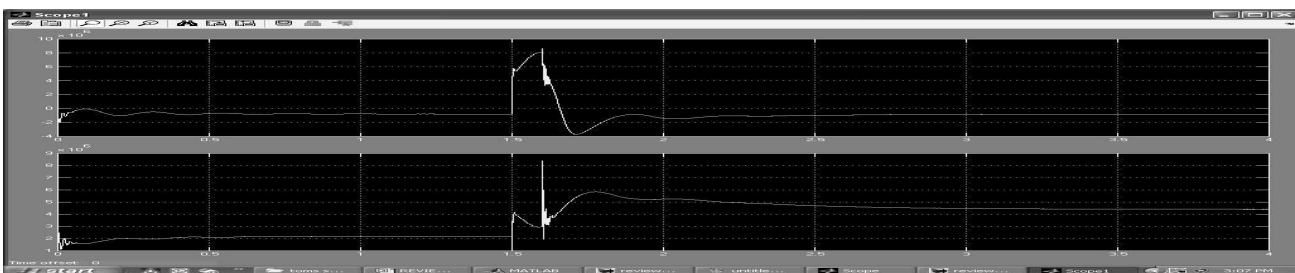


Figure 18. Waveform of P, Q at grid terminals during 3 phase fault at $t=1$ sec (wind farm capacity= 4.5MW, grid =25MVA)

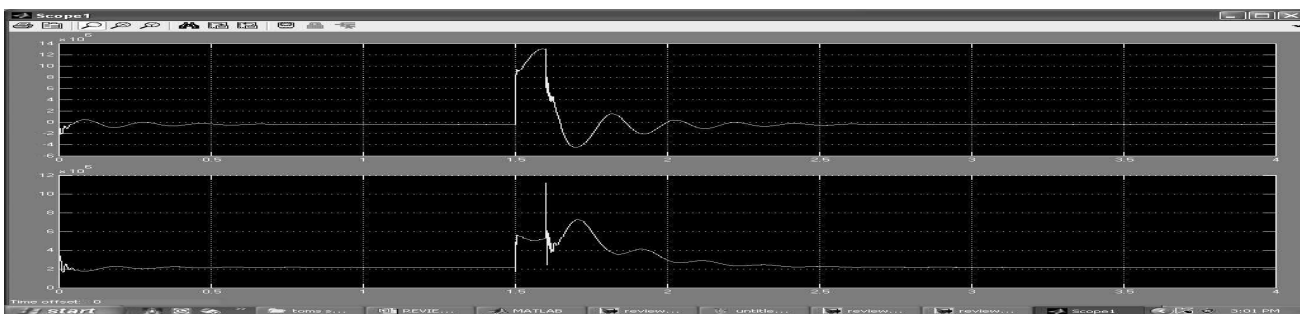


Figure 19 Waveform of P, Q at grid terminals during 3 phase fault at $t=1$ sec (wind farm capacity=4.5MW, grid=50MVA)

Table 8 shows the IEEE Standards for Interconnection system response to abnormal frequencies.

The Impact of 3-phase to ground fault is analyzed by considering the Wind Farm Capacity of 2.25MW and 4.5MW.

3.4 Wind Farm Capacity of 2.25MW

In Figure 17, response of 3 phase fault at grid terminals is shown when the capacity of wind farm is 2.25 MW & that of Grid is 25MVA. The fault is initiated at $t= 1$ sec & gets self cleared at $t=1.1$ sec.

3.5 Wind Farm Capacity of 4.5MW

When the capacity of the grid is doubled to 50 MVA, following response is obtained at grid terminals.

4. Conclusions

This paper demonstrates the impact of islanding during-power evacuation from wind turbines. It is found that the problems associated with power evacuation from wind farms entirely depends on the network topology. A Smaller generating system (i.e. for 2.25MW) can sustain

and function stably with a grid capacity of 25MVA. To keep the system in stable, the grid capacity has to be increased doubly (i.e. 50 MVA). It is found that Index based methods for anti-islanding doesn't ensure prevention from islanding as Index threshold could change due to change in system load, generation and configuration. The Voltage based Anti-Islanding technique fails to detect Islanding if the transfer of reactive power from grid to wind farm is kept minimum. The Islanding of single wind turbine has very little impact on nearby wind turbines and grid if it is detected in the given time.

The impact of three phase fault power evacuation from wind turbines is found that the problems associated with power evacuation from wind farms entirely depends on the network topology.

When the capacity of the Wind farm is doubled, system events results in unstable operation of the network. Instability can be seen from the changed operation condition after the fault is cleared at 100ms. The impact is minimised by increasing the capacity of the grid to 50 MVA.

The oscillation in frequency is not acceptable where deviation is more than 5 Hz. Maximum oscillation is observed when the wind farm capacity is observed when the wind farm capacity is 4.5 MW.

REFERENCES

- [1] S. Santoso and H. T. Le, "Fundamental time-domain wind turbine models for wind power studies," *Renewable Energy* 32, pp. 2436–2452, 2007.
- [2] K. C. Divya and P. S. N. Rao, "Models for wind turbine generating systems and their application in load flow studies," *Electric Power Systems Research* 76, pp. 844–856, 2006.
- [3] C. Diduch, J. Yin, and L. C. Chang, "Recent developments in islanding detection for distributed power generation," *Large Engineering Systems Conference*, pp. 124–128, 2004.
- [4] S. I. Jang and K. H. Kim, "An islanding detection method for distributed generations using voltage unbalance and total harmonic distortion of current," *IEEE Transactions on Power Delivery*, Vol. 19, No. 2, April 2004.
- [5] IEEE Standard 15477M, "Standard for interconnecting distributed resources with electric power systems," June 2003.
- [6] N. Farhan, A. Rajesh, and V Y. Mohammad, "Unintentional islanding and comparison of prevention techniques," *Proceedings of 37th Annual North American Conference*, pp. 90–96, 2005.
- [7] R. A. Walling and N. W. Miller, "Distributed generation islanding-implications on power system dynamic performance," *Proceedings of the IEEE/PES, Summer Power Meeting, Chicago, July 2002*.
- [8] S. Panda and N. P. Padhy, "Investigating the impact of wind speed on active and reactive power penetration to the distribution network," *International Journal of Electrical Systems Science and Engineering*, Vol. 1, No. 1, ISSN 1307–8917, 2008.

Some Advances in the Application of Weathering and Cold-Formed Steel in Transmission Tower

Fengli Yang¹, Junke Han¹, Jingbo Yang¹, Zheng Li¹

¹China Electric Power Research Institute, Beijing, China
Email: yangfl1@epri.ac.cn, flyangbj@tom.com

Received January 12th, 2009; revised February 4th, 2009; accepted February 16th, 2009.

ABSTRACT

Application of weathering and cold-formed steel in transmission lines can reduce steel consumption and environmental pollution. Some advances in the studies on the weathering and cold-formed steel in transmission tower are introduced. Firstly, corrosion-resistant tests of weathering steel samples under different simulating technical atmospheres were carried out separately for 240 hours. It shows that the corrosion degree of joint samples is higher than that of single chip samples, and the corrosion-resistant performance of weathering steel is superior to common carbon steel. The corrosion-resistance of weathering steel meets with the requirement of transmission tower. Secondly, experiments and finite element analysis for cold-formed angles and a 220kV prototype tower were completed, and the stability coefficient fitting curves as well as the modification formulas of slenderness ratio for cold-formed members were determined. According to the structural characteristics of transmission towers, four sections of cold-formed angles with different sections and slenderness ratios were selected in this study. The finite element model well predicted the buckling behaviour of the cold-formed members. Ultimate loads calculating by the fitting curve were well agreed to the experimental values, especially for the members with small slenderness ratios. Weight of the cold-formed steel tower can be reduced by more than 5 percent after considering the strength enhancement. Cost of the weathering and cold-formed steel transmission tower is nearly equivalent to that of hot-rolled steel tower with hot galvanizing.

Keywords: *Weathering Steel, Cold-Formed Steel, Bolted Joint, Corrosion-Resistant Test, Prototype Test, Buckling Analysis, Transmission Tower*

1. Introduction

With the increasing demand of electric power and the construction of resource-saving and environment-friendly society, higher requirements for the power grid have been proposed. Anticorrosion by hot galvanizing can cause environmental pollution and endanger human health. Hot rolled angles have been mainly used for transmission lines in China, and hot galvanizing is the unique anticorrosion technology for transmission tower. As for a rather small number of the sizes of hot rolled angles, steel waste has been widely existed in the design and product process of transmission tower by replacing small sizes with large sizes [1]. With the developing of electric power industry and steel industry as well as the strengthening of human awareness of environmental conservation, new types of steel should be used in transmission tower structures.

As the first country of developing and using weathering steel, weathering steel was applied in transmission towers early in American. In 1961, non-spraying weathering steel was used for two transmission towers in Massachusetts. Then weathering steel was applied in a 350 miles transmission line of Pennsylvania [2]. However,

weathering steel hasn't been used for transmission towers in China.

Cold-formed steel has been mainly applied to the light steel structures including the frame system of factory building, thin-walled steel truss, grid and reticulated shell structure. With the increasing of cold-formed steel in the industrial and civil buildings, the design theory has been made gradually perfected, and the major design basis is the Technical code of cold-formed thin-wall steel structures (Ministry of Construction of People's Republic of China) [3]. However, cold-formed steel has not been applied to transmission towers in China, and the structural design of transmission tower isn't suitable to indiscriminately copy that of the common light steel structure for its structural specialties. The theoretical and experimental study on the cold-formed members in transmission towers hasn't been developed.

Cold-formed steel has been used in transmission towers for several years in some countries, which include Italy, American, Canada, Britain, the former Soviet Union and Mexico etc. Ten to eighteen percent steel can be saved by the application of cold-formed steels in transmission towers comparing with using hot rolling angles.

Sponsored by State Grid Corporation of China.

Some specifications about cold-formed angles of transmission towers have been regulated in the American Design of Latticed Steel Transmission Structures [4] (ASCE) and the European Overhead Electrical Lines Exceeding AC 45kV [5] (CENELEC).

The objective of this paper is first to study the corrosion-resistance performance of weathering steel. Corrosion-resistant tests of weathering steel samples under different simulating technical atmospheres were carried out. Then, experiments and finite element analysis for cold-formed angles and a 220kV prototype tower were completed, the stability coefficient fitting curves as well as the modification formulas of slenderness ratios for cold-formed members were determined. Finally, the weight comparison analysis and economic analysis of the transmission tower using weathering and cold-formed steel was accomplished.

2. Application Study on Weathering Steel

In order to solve the problem of environmental pollution by using hot galvanizing technology, new types of weathering steel named by JT steel for transmission tower were developed by Jinan Steel&Iron Corporation. For investigating the corrosion-resistance performance of JT weathering steel, some experiments on the corrosion-resistance performance of single samples and bolted joint samples under different simulating atmosphere were carried out. The corrosion rates of the samples under different corrosion environment were obtained.

2.1 Experiments on Single Samples

Many studies have been completed on the corrosion-resistance performance of the single samples by JT steel. The research results are as follows [6].

Interior accelerated corrosion tests on the single samples of JT steel, CortenA steel and common carbon steel were compared under different simulating corrosion circumstances, which includes salt-fog corrosion, dry-wet alternate and moist heat. It shows that the corrosion rate decreases with time for all three types of steels. The corrosion-resistance performance of JT steel is better than that of CortenA steel and especially for common carbon steel.

2.2 Experiments on Bolted Joint Samples

The connections of bolted joints aren't tightening, and the steam-water interfaces can generate easily [7]. The corrosion-resistant performance of bolted joints is going to be studied. The schematic diagram of bolted joints is shown in Figure 1. The dimension unit in Figure 1 is millimeter.

The single chip and joint samples of JT weathering steel and common carbon steel were handled according to the structural characteristics of transmission towers, and the corrosion-resistant tests simulating technical atmosphere corrosion, sea atmosphere corrosion and acid rain atmosphere corrosion were carried out separately for 240 hours. Corrosion rates of the samples were measured, and the corrosion appearances and energy spectrum diagrams

were also analyzed. The macroscopic and microscopic corrosion morphology of JT steel bolted joint and common carbon steel bolted joint under simulating industrial atmosphere are shown in Figure 2 and Figure 3, respectively. It can be seen that the corrosion degree of carbon steel bolted joint is more serious than that of JT steel bolted joint.

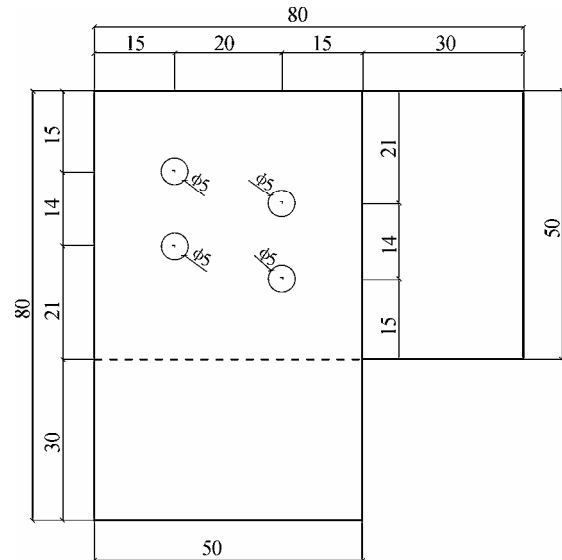
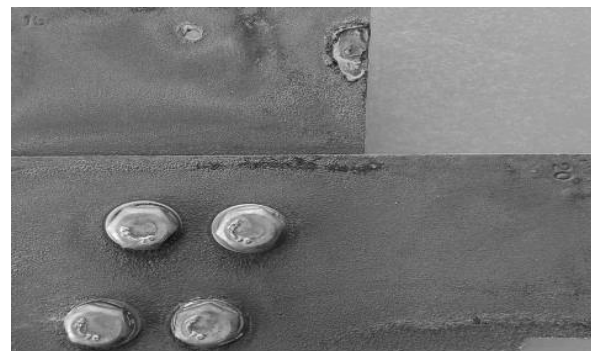


Figure 1. Experimental bolted joint sample



(a) JT steel



(b) carbon steel

Figure 2. Macroscopic corrosion morphology under simulating industrial atmosphere

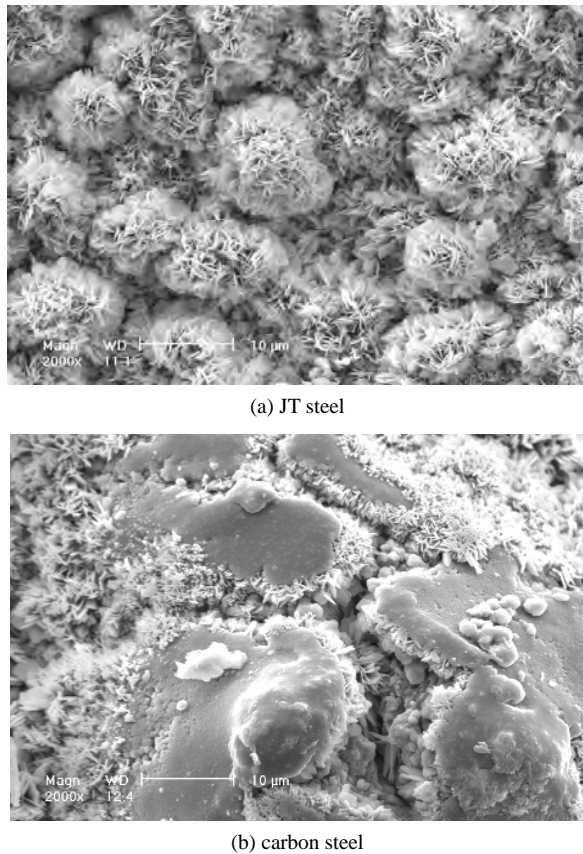


Figure 3. Microscopic corrosion morphology under simulating industrial atmosphere

The corrosion rates of the bolted joints of JT steel and common carbon steel are presented in Table 1. The corrosion rate of common carbon steel is about two times higher than that of the JT steel.

According to the analysis of the test results, the corrosion-resistant performances of the bolted joints of weathering steel and common carbon steel were compared. It shows that the corrosion degree of joint samples is higher than that of single chip samples, and the corrosion-resistant performance of JT weathering steel is superior to common carbon steel. The corrosion resistant performance of JT steel is not worse than that of Corten series, which has been used in the transmission towers of American. The test results provide important reference and foundation for the extension and application of JT weathering steel in transmission towers.

Table 1. Corrosion rates of the bolted joint samples

Samples	Weight loss by corrosion (g·dm ⁻²)	Average weight loss by corrosion (g·dm ⁻²)	Average Corrosion rate (g·m ⁻² ·h ⁻¹)
JT-1	2.90		
JT-2	3.50	3.22	1.34
JT-3	3.27		
Common carbon steel-1	6.10		
Common carbon steel-2	6.55	6.32	2.63

3. Application Study on Cold-Formed Steel

Cold-formed structures are mainly different from hot rolling steel structures in material molding style, which reflects the section and material property as well as the calculating theory [8,9]. Cold-formed steel member has the advantages of reasonable section shape, high integral stiffness and ultimate load. Cold-formed steel is suitable for tension and compression member, and the application of cold-formed steel makes full use of the material property and decreases the structural weight. Cold-formed steel can be machined in arbitrary dimension and shapes, and it may avoid the material waste in the fixed-length production of members. The reasonable sections of the members can be machined for different parts of a transmission tower. For example, the use of inequiaxial cold-formed angles for diagonal members can fully utilize the material property. In short, application of cold-formed steel in transmission towers will decrease steel consumption and acquire remarkable economic benefit.

As for solving the problems in the design method of cold-formed transmission tower, experimental and finite element analysis study on the design method for cold-formed steel members in transmission tower has been carried out in this project, which includes experiments and numerical analysis on members and prototype tower. The weight and cost of cold-formed steel tower was compared with those of hot rolled steel tower when meeting with same loading conditions.

3.1 Experiments and Finite Element Analysis on Members

Sections of the tested members include equal angle and equal lipped angle. Load versus strain analysis was carried out for the tested members. As shown in Figure 4, equal angles and equal lipped angles are expressed by Lx-x-z and Lx-x-y-z, respectively, which x, y and z separately represent the length of leg, the length of lip and the thickness of angles. The section properties of angles are shown in Table 2.

Based on the applicable design specifications of transmission towers, the slenderness ratios of axial compression members are from 0 to 120, and the slenderness ratios and quantities of experimental members are given in Table 3.

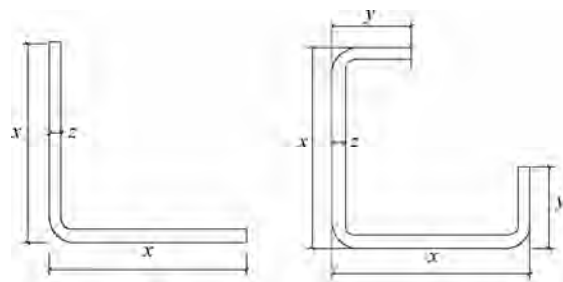


Figure 4. Types of member sections

Table 2. Dimensions of tested sections

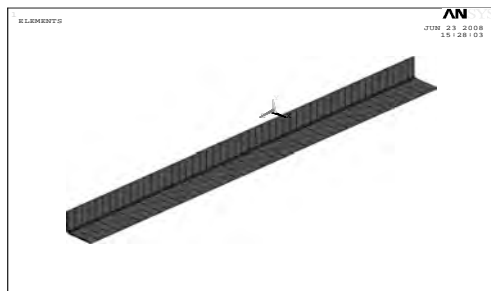
Section	Area (cm ²)	Parallel axis radius of gyration (cm)	Minimum axis radius of gyration (cm)
L70×70×5	6.59	2.19	1.34
L70×70×24×4	6.68	2.46	1.77
L160×160×60×10	39.33	5.66	4.15
L180×180×65×12	52.32	6.32	4.60

Table 3. Parameter description for tested members

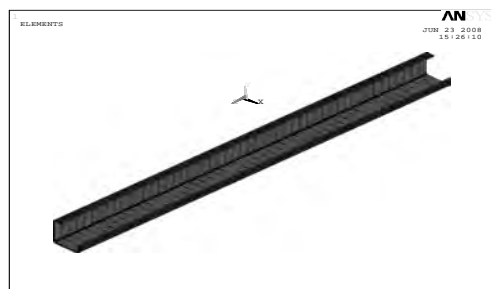
Section	Slenderness ratio	Quantities
L70×70×5	70, 80, 90, 100, 110	15
L70×70×24×4	50, 60, 70, 80, 90, 100, 110	21
L160×160×60×10	40, 60, 80	9
L180×180×65×12	40, 60, 80	9

The finite element program ANSYS was applied for the simulation of tested members. Four-node shell elements SHELL181 were used in this model. The SHELL181 element has six degrees of freedom at each node and is suitable for analyzing thin to moderately-thick shell structures. The element is well-suited for linear, large rotation, and large strain nonlinear applications. The finite element mesh size of 5mm×5mm (length by width) was used for the flat portions and a finer mesh size was used at the corners. Figure 5 shows the unreformed shape of a typical finite element mesh for an equal angle member and an equal lipped angle member.

It was stated in Young [9] that the residual stresses have a negligible effect on the ultimate load of the member. Hence, only initial overall geometric imperfections were considered in the finite element model. According to the Technical Code of Cold-formed Thin-wall Steel Structures (Ministry of Construction of People’s Republic of China), the initial overall geometric imperfections were considered by a sine curve with a magnitude of L/750 at the middle of the member.



(a) Equal angle



(b) Equal lipped angle

Figure 5. Finite element model

In the finite element model, the ends of the members were fixed in all degrees of freedom except for the translation in the direction of the applied load and the rotation around the longitudinal direction. The nodes other than at the two ends were free to translate and rotate in any direction. Static uniform loads were applied on centroid point of the loaded end, as in the experimental investigation. The nonlinear geometry parameter (*NLGEOM) was included to deal with the large deformation analysis in ANSYS.

As shown in Figure 6, a bilinear stress-strain curve for the flat and corner portions of members was applied in the analysis. Buckling modes and ultimate loads of the tested members were obtained by nonlinear buckling analysis.

The modes of buckling for tested members are presented in Figure 7. Load versus strain analysis was carried out for two sections of members with two slenderness ratios. The load versus strain behaviour of equal angle members and equal lipped angle members were obtained from the test results. For slender members, the behavior is symmetrical and the lips are in tension throughout the loading ranges. The heels of the sections of equal angle and equal lipped angle are always in compression indicating the neutral axis passed through the opposite corners. An unsymmetrical behavior is noticed in the case of stub members. It can be seen that the buckling mode of the slender members is flexure and that of the stub members is torsional-flexure. The ultimate loads of the tested members can be obtained by experimental analysis.

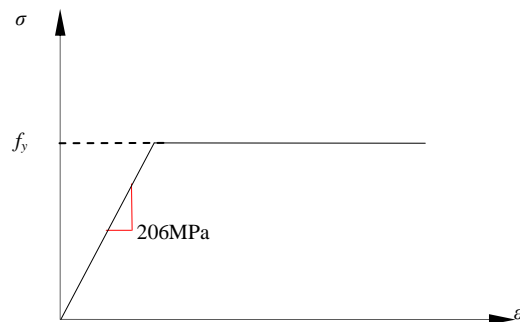


Figure 6. Stress-strain curve of the cold-formed steel



(a) Flexural buckling



(b) Torsional-flexure buckling

Figure 7. Buckling modes of tested members

Through the analysis of the experimental and analytical results, stability coefficient fitting curve and modification formulas of slenderness ratios for cold-formed members in transmission towers were determined. The ultimate loads calculating by the fitting curve are well agreed to the experimental values, especially for the members with small slenderness ratios. Some modification suggestions were proposed for the calculation of axial compression cold-formed angles.

The minimum radius of gyration was used to determine the slenderness ratio (λ) of the tested member. For calculation of the stability coefficients, the nondimensional slenderness ratios (λ_0) is given as:

$$\lambda_0 = \frac{\lambda}{\pi} \sqrt{\frac{f_y}{E}} \tag{1}$$

where f_y =yield stress and E =elastic modulus of cold-formed steels.

According to the ordinary range of slenderness ratios in the Chinese Technical Regulation of *Design for Tower and Pole Structures of Overhead Transmission Line* [10] (NETC) and the American *Design of Latticed Steel Transmission Structures*, stability coefficient curve of the axial compression cold-formed members with different slender ratios from 10 to 250 was fit for the sake of convenience of engineering application.

With reference to the applicable division methods of the stability coefficient curve, the stability coefficient curve of cold-formed members was divided into three parts as $0 < \lambda_0 \leq 1.2$, $1.2 < \lambda_0 \leq 2.5$ and $\lambda_0 > 2.5$. Most nondimensional slenderness ratios (λ_0) of the tested members were in the first part of $0 < \lambda_0 \leq 1.2$, and the other two parts of curves were fit by the finite element analysis results.

Expression of the fitting curves is given as follows.

For $0 < \lambda_0 \leq 1.2$

$$\varphi = 1 - 0.3205\lambda_0^2 \tag{2}$$

By the fitting of the results of finite element analysis, the other parts of expressions of the fitting curves were obtained and given as follows.

For $1.2 < \lambda_0 \leq 2.5$

$$\varphi = -0.1021 + 0.4863\lambda_0^{-1} + 0.3389\lambda_0^{-2} \tag{3}$$

For $\lambda_0 > 2.5$

$$\varphi = 0.0315\lambda_0^{-1} + 0.8352\lambda_0^{-2} \tag{4}$$

For the axial compression members with the slenderness ratios of 0 to 250, stability coefficients comparison of the fitting curves with the curves of applicable design standards for transmission towers is shown in Figure 8.

The yield stress of the members is 345MPa. It is noticed that the fitting curve is between the curves of the Chinese and American standards for the design of transmission towers, and the maximum variation is about 5%.

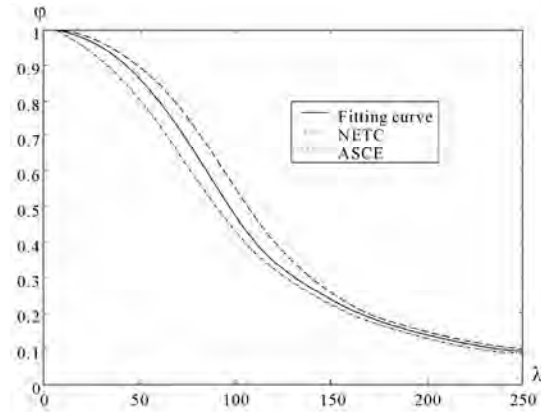


Figure 8. Comparison of stability coefficients

For different constraint conditions, the modification formulas of slenderness ratios are shown in Table 4.

3.2 Experiments and Numerical Analysis on Prototype Tower

According to the research results of cold-formed steel members, a 220kV prototype transmission tower using cold-formed steel was designed. For the convenience of weight comparison, the design conditions of the cold-formed steel tower were the same with those of a typical hot-rolled steel tower.

1) After full-stress analysis of the cold-formed steel transmission tower under 68 load cases including wind load and broken load etc, 19 types of cold-formed steel were selected which shown in Table 5.

For checking the design methods of bearing capacity for cold-formed transmission tower, the prototype strength test of the 220kV tower was completed in the tower and pole test station of China Electric Research Institute. The test tower and longitudinal loading tower were shown in Figure 9.

Table 4. Modification formulas

Constrained Conditions	Modification Formulas
Axial compression at one end, eccentric compression at the other end	$K\lambda=27.29+0.832\lambda$
Eccentric compression at two ends	$K\lambda=52.87+0.727\lambda$
Unconstrained at two ends	$K\lambda=18.80+0.875\lambda$
Constrained at one ends	$K\lambda=32.61+0.741\lambda$
Constrained at two ends	$K\lambda=32.14+0.709\lambda$

Table 5. Types of cold-formed steel for prototype tower

Type	Steel Class	Type	Steel Class
L40×40×3	Q235B	L75×75×6	Q345B
L40×40×4	Q235B	L82×82×6	Q345B
L46×46×4	Q235B	L85×85×6	Q345B
L50×50×4	Q235B	L90×90×6	Q345B
L56×56×4	Q235B	L90×90×7	Q345B
L56×56×5	Q235B	L102×102×7	Q345B
L63×63×5	Q235B	L106×106×8	Q345B
L63×63×5	Q345B	L110×110×9	Q345B
L70×70×5	Q345B	L115×115×9	Q345B
L70×70×6	Q235B		



Figure 9. Test tower and loading tower

Eight testing load cases include wind load, broken load and installation load. Displacements of key points and strains of key members under different load cases were measured. The numerical analysis results especially the displacements meet well with those of experimental results.

Overloading case of this test is the load case under 60 degree wind. When the overloading percent reached 65 percent, the tower wasn't destroyed. It shows that the cold-formed tower can meet the load cases, and it has much overage. The most important reason is that the design strength in numerical analysis is much less than the real yield strength of cold-formed steel. There is no upper limit for the strength classification of steel in China. The bearing capacity of tower structure can be enhanced greatly if the yield strength of cold-formed steel is much higher.

2) Weight comparison of cold-formed steel tower and hot-rolled steel tower is shown in Table 6. After using cold-formed steel, weight of the tower body and legs was reduced by 4.6 percent and 1.7 percent respectively, and the total weight of tower was reduced by 4.0 percent.

The strength enhancement of 10 percent by the cold forming effect was not considered in the design of transmission tower. The tests results show that the strength enhancement can be used. Weight of cold-formed steel tower can be reduced by more than 5% percent after considering the strength enhancement.

4. Conclusions

Application of weathering and cold-formed steel in transmission lines can reduce energy consumption and environmental pollution. Some advances in the studies on the weathering and cold-formed steel in transmission towers are introduced. Study on the application of weathering steel and cold-formed steel was completed in this paper.

Table 6. Weight comparison

Position	Hot-rolled Tower (kg)	Cold-formed Tower (kg)	Weight Reduce Percent (%)
Body	4125.7	3935.0	4.6
Leg	1130.7	1111.7	1.7
Total	5256.4	5046.7	4.0

Firstly, corrosion-resistant tests of weathering steel samples under different simulating technical atmospheres were carried out separately for 240 hours. It shows that the corrosion degree of joint samples is higher than that of single chip samples, and the corrosion-resistant performance of weathering steel is superior to common carbon steel. The corrosion-resistance performance of weathering steel meets with the requirement of transmission tower.

Secondly, experiments and finite element analysis for cold-formed angles and a 220kV prototype tower were completed. According to the structural characteristics of transmission towers, four sections of cold-formed angles with different sections and slenderness ratios were selected in this study. The finite element model well predicts the buckling behavior of the cold-formed members. Experiments and finite element analysis for the ultimate loads of the compression cold-formed angles were carried out, and the load-strain curves as well as the ultimate loads of experimental members were obtained. The experimental ultimate loads were compared with those of calculated by the applicable standards, and it shows that the applicable standards aren't adaptive to the strength design of compression cold-formed members of transmission tower in China. The stability coefficient fitting curve and modification formulas of slenderness ratios for cold-formed members in transmission towers were determined. The ultimate loads calculating according to the fitting curve are well agreed to the experimental values, especially for the members with small slenderness ratios. Some modification suggestions were proposed for the calculation of compression cold-formed angles, which provides important reference and basis for the application of cold-formed steels in transmission towers.

Finally, compared with the traditional hot-rolled steel transmission tower, application of cold-formed steel can reduce steel consumption by not less than 5 percent. The cost of the weathering and cold-formed steel transmission tower is equivalent to that of hot-rolled steel tower with hot galvanizing. So application of this new style steel can bring great social effects and economic returns.

5. Acknowledgment

This research was carried out within the science and technology project of State Grid Corporation of China. Name of the project is *Study on the Application of Weathering and Cold-formed Steel in Transmission Tower*. The project number is SGKJ [2007]117. The authors would like to thank the sponsor of State Grid Corporation of China.

REFERENCES

- [1] C. H. He, "Feasibility discussion on application of high strength cold-formed section steel in transmission tower," [J]. *Steel Construction*, 19(74), pp. 35-37, 2004.

- [2] Beijing Electric Power Construction Research Institute of SGCC, "Study on the application on weathering steel and cold-formed steel in transmission tower [R]," Beijing, 2007.
- [3] Ministry of Construction of People's Republic of China, Chinese Technical code of cold-formed thin-wall steel structures: GB50018-2002 [S], Beijing, 2003.
- [4] American Society of Civil Engineers, Design of Latticed Steel Transmission Structures: ASCE110-97 [S], USA, 1998.
- [5] European Committee for Electrotechnical Standardization. Overhead electrical lines exceeding AC 45 kV: EN50341-1 [S], 2001.
- [6] B. S. Gu, B. Wang, X. C. Ji, M. S. Xia, and J. H. Liu, "Study on Corrosion of JT245 Weathering Steel," [J]. Journal of Steel and Iron Research, 17(6), pp. 55-58, 2005.
- [7] F. L. Yang, J. K. Han, J. B. Yang, M. S. Xia, and Z. Y. Wang, "Study on corrosion-resistant performance tests of weather-proof steel node used in transmission towers," [J]. Electric Power Construction, 29(9), pp. 23-28, 2008.
- [8] S. J. Mohan, S. R. Shabeen, and G. M. S. Knight, "Behavior of cold formed lipped angles in transmission line towers," [J]. Thin-Walled Structures, 44, pp. 1017-1030, 2006.
- [9] B. Young, "Experimental investigation of cold-formed steel lipped angle concentrically loaded compression members," [J]. Journal of Structural Engineering, 131(9), pp. 1390-1396, 2005.
- [10] National Economy and Trade Commission of PRC. Technical Regulation of design for tower and pole structures of overhead transmission line [S]. DL/T5154-2002, China Electric Press, 2002.

Identification of Lightning Stroke and Fault in the Travelling Wave Protection

Guibin Zou¹, Houlei Gao¹, Wenbo Su², Dapeng Wang²

¹School of Electrical Engineering, Shandong University; ²EPRI Shandong Electric Power Corporation, China.
Email: guibinzou@yahoo.cn; houleig@sdu.edu.cn

Received January 8th, 2009; revised January 31st, 2009; accepted February 11th, 2009.

ABSTRACT

To resolve the impact of transient high frequency signals induced by lightning stroke on the travelling wave protection of transmission line, a novel identification algorithm is proposed. Using the characteristics of symmetric current waveform induced by lightning stroke without causing fault and that of asymmetric current waveform generated by fault within a very short time interval, the waveform of transient current above and below time-axes are integrated respectively. First, through comparing the relative ratio of them with threshold value, the primary criterion identifying fault and lightning stroke is constructed; Secondly, to improve the reliability of discrimination between lightning stroke with and without causing fault, according to the difference of them, the secondary criterion is also defined. The simulation results and analysis demonstrate that the proposed integral criterions are valid and correct.

Keywords: Transmission Line, Travelling Wave Based Protection, Lightning Stroke, Characteristic of Waveform, Criterion

1. Introduction

Travelling wave protection or transient component based protection is capable of achieving ultra high speed fault detection, and hence it has been focused by electrical engineers all over the world for tens of years. However, its reliability is always affecting application of protection in real power grid. The waveforms of transient current induced by lightning stroke and fault are similar, so lightning stroke is one of main influence factors which lead to low reliability of transient component based protection. Therefore, to improve the reliability of travelling wave protection or transient component based protection, it is a key to identify fault and disturbance of lightning stroke without causing fault correctly.

For these disturbances induced by lightning striking on transmission line, in recent years many specialists carried out a series of theoretical research, and obtained some useful results [1,2,3,4,5,6,7]. But most of previous identification principles used wavelet analysis tool to extract spectrum energies of different frequency bands of transient current signal, and according to energy differences, identification algorithms are implemented. Generally, these algorithms are complicated and difficult to use in practice. Different from the former identification methods, a novel integration based combined criterions are presented in this paper. Theoretical analysis and simulation results confirm that this identification algorithm is simple and has high reliability and sensitivity.

2. Characteristic Analysis of Transient Signal

From high voltage engineering we can know that lightning stroke is classified into two categories: one is direct lightning stroke and the other is indirect lightning stroke. Indirect lightning does not directly strike on transmission line and thus, the amplitude of over-voltage of line is low. For EHV/UHV transmission lines, since their towers are very high, it has not damage to them in general. But the probability of lightning striking directly on those lines is high [8]. When lightning directly strikes on transmission line, due to lightning current with high amplitude directly injects into the line, and hence serious over-voltage is caused. Direct lightning stroke is most serious high frequency disturbance to the transient component based protection, and it is focused on below.

When lightning stroke happens, the magnitude and waveform of lightning current are related to many factors, such as position and environment of transmission line, season and climate. So its amplitude and waveform are random. Although lightning currents have some big differences among different lightning strokes, the actual measured data demonstrate that they are all pulse waves with single pole. Moreover, its waveform is close to pair exponential curve as shown in Figure 1.

This waveform is expressed as in (1)

$$i = I_0(e^{-at} - e^{-bt}) \quad (1)$$

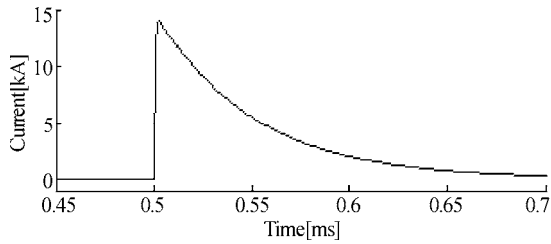


Figure 1. Waveform of lightning current

where I_0 is the peak value of lightning current; α and β are coefficients of attenuation. IEC defined a normal pair exponential lightning wave using front time t_f and time to half-value t_n . Time t_f is about $1 \sim 4\mu s$ and its mean value is $2.6\mu s$. Time t_n is about $20 \sim 90\mu s$, which mean value is $43\mu s$.

Using PSCAD/EMTDC, a model of 500kV power transmission system is constructed as shown in Figure 2. The line is frequency-dependent and balanced transposition. Tower is conventional horizontal structure, and on its top two shield lines are equipped. The line MN is object researched and site of measurement R lies in end M . Sampling frequency is 1 MHz. Stray capacitance of busbar is supposed as $C_s=0.01\mu F$. Supposing general fault and lightning stroke with or without causing fault occur at site f away from end M 50 km, observing their characteristics of transient current waveforms respectively.

2.1 Waveform Characteristic of Lightning Stroke without Causing Fault

Lightning stroke causing fault has already resulted in line fault, so the relay should operate and cut the faulted line immediately; but lightning stroke without causing fault has not led to line fault actually, the relay should not operate. Therefore, the transient component based protection must correctly discriminate the waveform differences between lightning stroke without causing fault and general fault. There are two kinds of causes which lead to

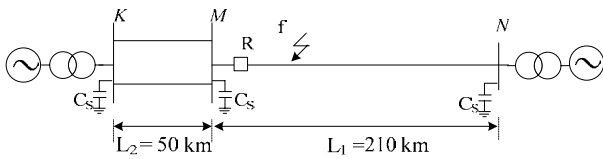


Figure 2. Model of 500kV power transmission system

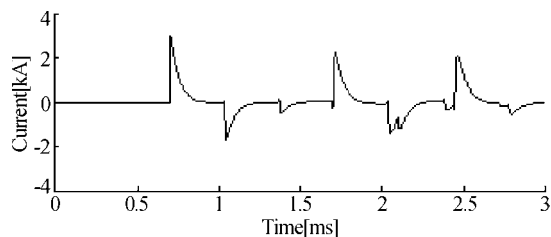


Figure 3. Aerial mode current of lightning stroke without causing fault

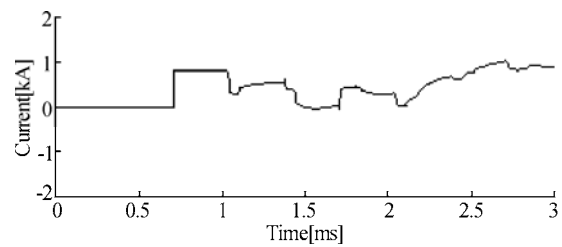
lightning fault, one is shield failure and the other is back flashover. As mentioned in section 2, the towers of EHV/UHV transmission lines are very high, the back flashover rarely happens, so in the following simulation we only consider lightning fault resulting from shield failure. Due to electromagnetic coupling exists among different phases, Clark transform is applied and aerial mode current is analyzed. Figure 3 shows aerial mode current waveform of transient component when tiny lightning stroke without causing fault occurs.

From Figure 3, it can be seen that wave peaks of current traveling wave induced by lightning stroke appear by turns above and below the time axes, and these wave peaks become attenuation gradually along time axes. Alternation frequency and attenuation speed are related to the length of line and structure of busbar. The polarity, wave shape and amplitude of the initial wave peak reflect the characteristics of lightning wave. The sequent wave peaks with same polarity are reflection wave of forward busbar and the wave peaks with opposite polar come from reflection wave of backward busbar. Since the actual transmission line is not lossless, during reflection and refraction of current wave, the wave peak continues to be attenuated and disappear in the end.

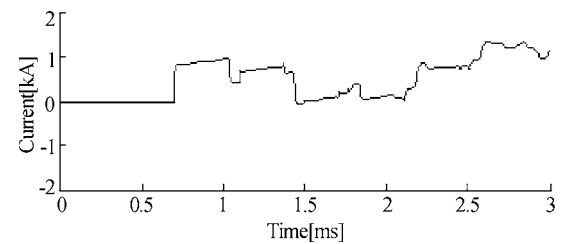
2.2 Waveform Characteristic of Ordinary Line Fault

Supposing a fault of phase A to ground and that of phase A to phase B occur on the line respectively. Fault earth resistance of single phase fault is 50Ω and fault inception angle is 60° . Figure 4 (a) and (b) show aerial mode current waveform of fault component respectively.

In Figure 4, it is obvious that the initial current signal contains much high frequency components owing to reflection and refraction of traveling wave. The top of initial wave peak is relative smooth close to a line, and its upward edge and downward edge are all very steep. In a very short time interval, the waveform generally lean to



(a) Fault of phase A to ground



(b) Fault of phase A to B

Figure 4. Aerial mode current waveform of fault

one side of time axis, sometime waveform crosses zero, which is related to fault inception, configuration of busbar, *et al.* But as a whole, the wave shape shows a characteristic of flat variation.

2.3 Waveform Characteristic of Lightning Stroke with Causing Fault

Lightning strokes with causing fault actually include that lightning directly strikes on transmission line and tower, and further leads to insulation flash. For a same transmission line, the level enduring lightning of lightning striking on line is far lower than that of lightning striking on tower. Although their levels are different, the characteristics of current waveform induced by lightning stroke causing short-circuit are consistent, i.e. fault component of transient current is generated together by lightning current and power frequency extra voltage at fault site. In simulation, the amplitude of lightning current is 25kA. Figure 5 shows aerial mode current waveform when lightning stroke with causing fault occurs.

Figure 5 shows that fault component current synchronously possesses these characteristics of two kind waveforms above mentioned: in the initial part of waveform, lightning wave makes a main effect, the positive and negative wave peaks appear alternately, and subsequent waveform displays some characteristics of short circuit fault. Within a short time interval, waveform leans to one side of time axis.

3. Criterion of Identification

According to above analysis, after transmission line is disturbed, within a very short time, the characteristics of transient current waveform are concluded as follows:

- Generally, the current waveform induced by lightning stroke without causing fault is symmetrical. The wave peaks of current traveling wave appear alternately above and below the time-axes, and peak values become attenuation gradually and until zero.
- As a whole, the transient current waveform generated by line fault shows a characteristic of smooth variation. In general, it leans to one side of time axis, sometimes crosses time axis.
- For the current waveform induced by lightning stroke causing fault, in its initial part the wave shape displays some characteristics of lightning wave, and after tens or hundreds of microseconds, which shows the characteristics of waveform of fault.

According to the characteristic differences of transient current waveforms generated by different disturbances, the integral criteria are defined. The transient current waveform above and below time axis are integrated respectively as follows:

$$I_+ = \int_{t_0}^{t_0+\tau} i_+(t) dt \quad (2)$$

$$I_- = \int_{t_0}^{t_0+\tau} |i_-(t)| dt \quad (3)$$

where $i_+(t)$ and $i_-(t)$ are fault component current above and below time axis respectively; I_+ and I_- are integral values above and below time axis respectively within time-window τ ; t_0 is inception moment when relay detects break of transient current. Owing to the symmetry of current waveform induced by lightning stroke without causing fault, I_+ and I_- have a similar value; but for fault of line, the waveforms demonstrate they have a big difference. For lightning stroke causing fault, I_+ and I_- are in between them above mentioned. To enlarge relative ratio value of I_+ and I_- , and calculate their difference, two formulas are defined as follows:

$$\lambda = \frac{\max(I_+, I_-) - \min(I_+, I_-)}{\min(I_+, I_-)} \quad (4)$$

$$S = |I_+ - I_-| \quad (5)$$

where λ is relative ratio value of I_+ and I_- , and S is their difference. In engineering calculation, discrete formulas of (2) and (3) are following:

$$I_+ = \sum_{k=n_1}^{n_2} i_+(k) \quad (6)$$

$$I_- = \sum_{k=n_1}^{n_2} i_-(k) \quad (7)$$

where k , $i(k)$ are sampling point and instantaneous value of fault component current respectively; n_1 is the initial sampling point where the break of transient current is detected. The number of points between n_1 and n_2 reflects a length of time-window. To improve speed of calculation and take waveform differences of transient current generated by different disturbances into account, the length 1ms of time-window is adopted in simulation.

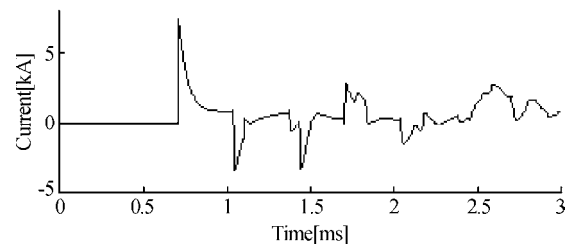


Figure 5. Waveform of lightning stroke causing fault

Table 1. Values of integration, λ and S after difference disturbances

	$I_+/(kA)$	$I_-/(kA)$	λ	$S/(kA)$
Lightning stroke without causing fault	172.2344	125.1907	0.3758	47.0437
Fault of phase A to ground	455.6549	4.1076	109.9307	451.5474
Fault of phase A to B	578.9154	2.7437	209.998	576.1717
Fault induced by lightning stroke	867.2476	292.8195	1.9617	574.4281

For sampling frequency 1MHz, the number of sampling points is 1000. Table 1 shows simulation results of fault and lightning stroke with and without causing fault from measurement site 60km.

Data of Table 1 show: when lightning stroke without causing fault occurs, integral values I_+ and I_- are similar, moreover values λ and S are all small; when fault occurs, the difference between values I_+ and I_- is big, meanwhile values λ and S are all big; when a fault induced by lightning stroke occurs, the difference between values I_+ and I_- is also big, and value λ is in between that of short-circuit and that of lightning stroke without causing fault, but value S is very big. Therefore, integral identification criterions are defined as follows:

- First, the primary criterion is defined. Threshold value λ_i is set as 1, if condition $\lambda > k_1 \lambda_i$ (k_1 is coefficient of reliability, its value is supposed as 1.2) is met, the disturbance of line is directly thought as fault and relay should operate rapidly.
- Secondly, to improve the reliability of identification of lightning stroke with and without causing fault, an additional criterion is defined. Threshold value S_i is set as 100 kA (its value is related to the sampling frequency and the length of time-window), if condition $\lambda_i < \lambda < k_1 \lambda_i$ is met, at the same time value S meets condition $S > k_1 S_i$, the disturbance of line is also determined as fault, relay should operate correctly. Otherwise, it is discriminated as lightning stroke without causing fault or other disturbance, and relay should not operate.

4. Simulation and Analysis

Based on analyzing waveform characteristics of fault component currents induced by various disturbances, the integral identification criterions are presented. But magnitude of transient current is affected by many factors, such as fault inception conditions, amplitude of lightning current, position of disturbance, configuration of busbar, *et al.*, furthermore those factors possibly influence the reliability and sensitivity of integral criterions. Therefore using 500kV power transmission system model shown in Figure 2, the different disturbances are supposed in order to confirm validity of criterions.

4.1 Simulation Results and Analysis for Different Faults

Different faults of line will generate different fault component currents, and possibly affect the reliability of criterions. These factors include position of fault, fault inception angle, fault resistance and type of fault. According to those factors above mentioned, Table 2 listed corresponding simulation results.

From Table 2 we can see: for various faults from busbar M 60km, values λ are far bigger than 1.2; for these faults with different inception angles, corresponding values λ are also bigger than 1.2; for fault of close to measurement site (from busbar M 1km), remote-end fault

(from busbar M 209km), corresponding values λ are all higher than threshold value 1.2. These faults with little inception angle and big fault resistance would directly affect magnitude of transient current. But simulation results show: for two special types of faults, although the additional criterion S is less than 100kA, the primary criterion λ is far higher than 1.2. Therefore, whatever conditions of fault are, the integral criterions can make a correct discrimination, moreover they have a very high reliability.

4.2 Simulation Results and Analysis for Lightning Stroke without Causing Fault

It is well known that lightning stroke is random, and the magnitude of lightning current is related to many factors. Generally, for transmission line with shield line, when the magnitude of lightning current is less than a special value (such as 20kA, related to configuration of line), lightning can strikes on line [9]. The position of lightning stroke and the magnitude of lightning wave will have an influence on magnitude of transient current. For various conditions of lightning stroke, Table 3 gives corresponding simulation results.

From Table 3 we can see: within a definite magnitude of lightning current, whichever phase lightning strikes on and wherever position of lightning stroke is, the corresponding values λ are all less than 1.2; in general, the bigger magnitude of lightning current is, the stronger current traveling wave induced by lightning stroke is, moreover value S may be bigger than 100kA, but it hardly has any influence on value λ . Therefore, using the primary criterion, relay can easily discriminates the disturbance as lightning stroke without causing fault or other disturbance, and criterion has also a high reliability.

Table 2. Simulation results for different faults

T	L/(km)	$\theta/(^\circ)$	R/(Ω)	$I_+/(kA)$	$I_-/(kA)$	λ	S/(kA)
Ag	60	60	50	453.5737	4.1860	107.3542	449.3877
AC	60	—	—	605.1117	3.4286	175.4883	601.6830
BCg	60	—	—	188.6978	1.1684	160.4997	187.5294
Bg	60	0	50	0	54.2867	$+\infty$	54.2867
Bg	60	90	50	11.9809	230.5606	18.2440	218.5797
Ag	1	60	50	519.8879	120.9268	3.2992	398.9611
Ag	209	60	50	561.9304	0	$+\infty$	561.9304
Cg	60	45	0	0	187.8609	$+\infty$	187.8609
Cg	60	45	500	0	47.9672	$+\infty$	47.9672

Note: T – type of fault; L – distance from busbar M; θ – fault inception angle; R – fault resistance.

Table 3. Simulation results for lightning stroke without causing fault

P	L/(km)	$I_0/(kA)$	$I_+/(kA)$	$I_-/(kA)$	λ	S/(kA)
A	1	15	173.6715	126.2587	0.3755	47.4127
A	10	15	173.6151	126.1870	0.3759	47.4281
A	209	15	262.1816	269.3711	0.0274	7.1895
B	60	15	167.5774	124.7613	0.3432	42.8161
C	60	3	45.0860	76.0670	0.6872	30.9810
C	60	10	158.1048	235.8736	0.4919	77.7688
C	60	20	319.8308	464.3272	0.4518	144.4964

Note: P – phase of lightning stroke; I_0 – amplitude of lightning current.

Table 4. Simulation results for lightning stroke with causing fault

P	$L/(km)$	$I_0/(kA)$	$L_r/(kA)$	$I_r/(kA)$	λ	$S/(kA)$
A	1	25	1093.2	497.0937	1.1992	596.1001
A	60	25	848.9874	292.8628	1.8989	556.1246
A	209	25	986.5050	490.0102	1.0132	496.4948
B	60	30	937.8617	363.1981	1.5822	574.6636
A	60	30	937.8592	363.1872	1.5823	574.6720
A	60	40	1122.0	510.3125	1.1985	611.6837

4.3 Simulation Results and Analysis for Lightning Stroke Causing Fault

For lightning stroke causing fault, to check its influence on integral criterions, in simulation adding magnitude of lightning current to 25kA and above, the insulation flash of line occurs, Table 4 lists simulation results.

Simulation results from Table 4 show: when lightning stroke causing fault occurs, values λ are bigger than those of lightning stroke without causing faults but less than those of faults, and possibly be between λ_i and $k_1\lambda_i$, but values S are far bigger than 100kA. Though low value λ possibly lowers the sensitivity of primary criterion, a big value S improves the sensitivity of additional criterion enormously. Therefore, using the primary and additional criterions together can improve the reliability of identification of lightning stroke without causing fault.

5. Conclusions

Correct identification of lightning stroke disturbance is a foundation for the reliability of travelling wave protection or transient component based protection. After analyzing the current waveform characteristics of fault and lightning strokes with and without causing fault in detail, the integral identification criterions are proposed. Within a short time-window, transient current waveforms above and below time axis are integrated respectively, further their relative ratio is defined as primary criterion and their difference is defined as additional criterion. Simulation results and analysis demonstrate: for ordinary fault

and lightning stroke without leading to line fault, the primary criterion has a high reliability of identification; for lightning strokes with and without causing fault, sometimes the sensitivity of primary criterion is low, but additional criterion has a high sensitivity. Therefore, the proposed integral criterions can correctly identify general fault and disturbance of lightning stroke, moreover have a high reliability.

REFERENCES

- [1] G. Wang, H. F. Li, J. C. Zhao, and M. Wu, "Identification of transients on transmission lines caused by direct lightning strokes based on multiresolution signal decomposition," Proceedings of the CSEE, Vol. 24, pp. 139–144, 2004.
- [2] D. J. Si, H. C. Shu, X. Y. Chen, and J. L. Yu, "Study on characteristics and identification of transients on transmission lines caused by lightning stroke," Proceedings of the CSEE, Vol. 25, pp. 64–69, 2005.
- [3] H. F. Li, G. Wang, and J. C. Zhao, "Study on characteristics and identification of transients on transmission lines caused by indirect lightning stroke," Proceedings of the CSEE, Vol. 24, pp. 114–119, 2004.
- [4] J. D. Duan, B. H. Zhang, Z. G. Hao, and H. X. Ha, "Identification of lightning and fault in the EHV transmission line transient-based protection," Automation of Electric Power Systems, Vol. 28, pp. 30–35, 2004.
- [5] X. L. Dong, Y. Z. Ge, and X. Z. Dong, "Effect of lightning on protection based on travelling wave," Proceedings of CESS, Vol. 22, pp. 74–78, 2002.
- [6] J. F. Ren, J. D. Duan, and B. H. Zhang, "Identification of lightning disturbance in ultra-high-speed transmission line protection," The 2th IEEE/PES Transmission and Distribution Conference, Dalian, China, pp. 14–18, 2005.
- [7] H. X. Ha and B. H. Zhang, "The study on identification of fault and lightning strokes in boundary protection for EHV transmission lines," Relay, Vol. 31, pp. 1–5, 2003.
- [8] X. J. Wei and W. H. Wu, "The analysis of lightning protection for EHV and UHV transmission lines in Russia," High Voltage Engineering, Vol. 24, pp. 76–79, 1998.
- [9] A. F. Imece, D. W. Durbak, H. Elahi, *et al.*, "Modeling guidelines for fast front transients," IEEE Transactions on Power Delivery, 11, pp. 493–506, 1996.

Desulphurization Characteristic of Industry Alkaline Wastes during Coal Combustion

Bin Zheng¹, Chunmei Lu²

¹School of Traffic and Vehicle Engineering, Shandong University of Technology, China, ²School of Energy and Power Engineering, Shandong University, China.

Email: zhengbin@sdut.edu.cn; cml@sdu.edu.cn

Received January 13th, 2009; revised February 5th, 2009; accepted February 17th, 2009.

ABSTRACT

The desulphurization characteristics of four sorts of industry alkaline wastes and one sort of limestone were studied by means of flue gas analyzer and the high temperature tube reactor. Pore structure and desulphurization product characteristic were investigated respectively by mercury porosimeter and XRD diffraction technology. The reasons why wastes and limestone hold the different desulphurization capability were deeply discussed. The result shows that white clay and carbide slag could capture the release of sulfur at 800-1100°C. Salt slurry and red mud could capture the release of sulfur at first stage at 800-900°C. But when the experimental temperature rises to 1000°C, the sulfur capture abilities of them depress. Pore structures of waste are higher than that of limestone. This makes the sulfation reaction goes further. To sum up, wastes have better sulfur capture ability.

Keywords: Industry Alkaline Waste, Desulphurization, Pore Structure, XRD, Limestone

1. Introduction

Combustion desulphurization technology has been concerned as an important development direction of coal clean technology. Natural limestone has been widely used as desulphurization sorbent because it contains a great amount of CaO. But the actual operating result is that limestone's desulphurization efficiency and CaO conversion fraction are not high in the fluidized bed furnace, and in other combustion mode, its efficiency is even lower [1]. When the limestone is added excessively, ash and CO₂ in the flue gas will increase greatly.

With the rapid development of Chinese industry, the accumulation and discharge of industry wastes become more and more serious, which pollutes the environment. Only a small number of wastes are used as building material. And some useful matters are reclaimed from these wastes. Many industry alkaline wastes contain a great deal of CaO and alkali Oxide [2,3,4,5,6,7], which can react with SO₂ directly. If these alkaline wastes can be used as desulphurization sorbent, the purpose of using waste to treat pollution will be achieved. The desulphurization characteristics of four sorts of industry alkaline wastes and one sort of limestone are studied by means of flue gas analyzer and the high temperature tube reactor in this paper. Pore structures of industry alkaline wastes and limestone are investigated by mercury porosimeter. Desulphurization product characteristics are analysed by

XRD diffraction technology.

2. Experiments

2.1 Materials

Four sorts of industry alkaline wastes and one sort of limestone are used as samples in this experiment. White clay comes from Laiwu. Red mud comes from Zibo. Carbide slag comes from Jinan. Salt slurry comes from Binzhou. Limestone comes from Zibo. The samples' chemical composition is analysed according to GB3286. The results are given in Table 1. The coal sample is lean coal which comes from Huangtai. Proximate and sulfur form analysis of the coal is shown in Table 2.

2.2 Procedure

The desulphurization characteristics of sorbents were studied in desulphurization experimental reactor (Figure 1). The mass of the coal sample is 100±0.1mg. The coal sample is added into the sorbent at the rate of Ca/S=2. The SO₂ of flue gas was analyzed by MSI flue gas analyzer.

The phase composition of desulphurization product was analyzed by target D/MAX-B X-ray diffractometer. The pore structure was studied by Poromaster60 mercury porosimeter.

Sulfur capture ability of sorbent is judged by the variable amount of SO₂ released from the coal after adding desulphurization sorbent. The ratio of SO₂ released is calculated by the formula (1):

Project Supported by National Natural Science Foundation of China (No.59976019), Shandong Natural Science Foundation (No. Y2003F07).

$$V_{SO_2} = \frac{M_s \times \int_{t_0}^t C_{(t)} V_t dt}{M \times S_t \times M_{SO_2}} \times 100\% \quad (1)$$

Where M_s is the mole mass of sulphur, M_{SO_2} is the mole mass of SO_2 , $C_{(t)}$ is the concentration of SO_2 at time t , V_t is flux of flue gas, M is the mass of coal and S_t is the sulphur containing ratio in coal.

3. Results and Discussion

3.1 Desulphurization Characteristics of Wastes

The desulphurization characteristics of sorbents were studied at 800-1200°C, as is shown in Figure 2.

SO_2 is released through two stages in coal combustion. The rate curve shows tow-peak structure. FeS and aromatic sulfur in the coal will release when temperature is above 1000°C. The rate curve shows one-peak structure at 800-900°C [8].

Only SO_2 at first stage is released at 800°C (Figure 2). The rate curve shows one-peak structure. The ultimate ratio of SO_2 released is 53%. When limestone is added into coal, the amount of SO_2 released decreases. When the industry alkaline wastes are added into the coal, the amount of SO_2 released decreases obviously. Salt slurry's effect is the most outstanding. There is almost no SO_2 released and the ultimate ratio of SO_2 released is only 11.7%. White clay's effect is obvious and the rate is 13.5%. Red mud and carbide slag also can capture the release of SO_2 at first stage. Wastes can resist SO_2 released. Sulfur capture ability of wastes higher than lime-

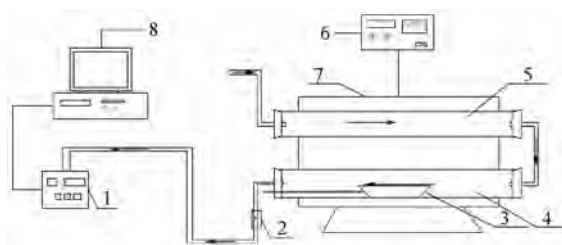


Figure 1. Schematic diagram of the experimental apparatus (1-flue gas; analyzer; 2-flowmeter; 3-test sample; 4-reactor; 5-preheater; 6-thermostat; 7-tube heater; 8-computer)

Table 1. Chemical composition analysis of test sample (%)

Sample	LOSS	SiO ₂	Al ₂ O ₃	Fe ₂ O ₃	CaO	MgO	Σ
1 [#] white clay	36.2	10.7	0.86	0.21	48.5	1.8	98.27
2 [#] red mud	19.1	18.4	11.2	10.01	36.95	1.87	97.53
3 [#] carbide slag	28.5	2.8	1.5	0.2	66.4	0.1	99.5
4 [#] Limestone	43	2.1	0.46	0.2	51.6	2.5	99.86
5 [#] salt slurry	33.5	11.91	2.64	1.77	33.96	13.9	97.68

Table 2. Proximate and sulfur form analysis of coal

Proximate analysis (%)				Sulfur form analysis (%)				Net calorific power (Q _{net,ar} /kJ·kg ⁻¹)
M _{ad}	A _{ad}	V _{ad}	FC _{ad}	S _t	S _s	S _p	S _o	
1.14	32.31	14.41	52.14	1.88	0.06	1.16	0.66	20696

stone's always. According to XRD pattern of sulfur retention at 800°C (Figure 3), it is clear that after adding white clay, carbide slag and red mud, the main desulphurization product is CaSO₄. The diffraction maximum of CaSO₄ is clearly higher than that of desulphurization product caused by adding limestone. It shows that white clay, carbide slag and red mud are more easily react with SO_2 directly. Besides CaSO₄, there is MgSO₄ in the sulfur retention with salt slurry. MgSO₄'s diffraction maximum is high. It shows that magnesium-based matters in salt slurry can capture the release of SO_2 at first stage, which improves salt slurry's sulfur capture ability. Least CaSO₄ is produced after limestone is added, and CaO still exists in great amount. It is because limestone's calcination speed is slower, which results in worst desulphurization efficiency.

At 900°C, the amount of SO_2 released increases obviously and the ultimate ratio is 94%. When experimental samples are added into the coal, the amount of SO_2 released decreases greatly. But the change of each material's effect is greatly different. White clay's desulphurization effect is the most outstanding, and the ultimate ratio of SO_2 released is about 21%. 73% is reduced compared with coal's ratio. Carbide slag shows better desulphurization efficiency at such temperature, and its ratio is about 38%. 56% is reduced compared with coal's ratio. When red mud and salt slurry are added into the coal, the ratios reduce 39% and 47% respectively.

At 1000°C, since FeS and aromatic sulfur in the coal begin to release in great amount, the late stage appears in the process of SO_2 released. Limestone doesn't reduce SO_2 released amount at first stage, but no SO_2 is released at late stage. The ratio of SO_2 released reduces 54%. After white clay and carbide slag are added, the amount of SO_2 released reduces obviously at first stage and no SO_2 is released at late stage nearly. The ratios reduce 70% and 66% respectively. Red mud and salt slurry have better desulphurization performance at first stage, but have no efficiency at late stage, which makes their desulphurization efficiency depress, and the ratios reduce 35% and 36% respectively.

At 900-1000°C, white clay can capture the release of sulfur at first and last stage. White clay's desulphurization performance is the best. This is because its represents better micro-structural characteristics, which prepares for rapid pyrolysis of CaCO₃, adsorption of SO_2 and sulfation reaction. Carbide slag also has better sulfur capture ability, only second to white clay. The reason is that carbide slag contains rich Ca(OH)₂. Ca(OH)₂ will be decomposed into CaO at about 400°C. So it can react with SO_2 early and capture SO_2 . Carbide slag represents better micro-structural characteristics of inner pore similarly. Salt slurry and red mud contains magnesium-based matter and so they can react with SO_2 directly at lower temperature. They represent better micro-structural characteristics, which is good for the full sulfation reaction. Therefore they can capture the release of sulfur at first stage. But the stability of MgSO₄ is poor. The sulfate is

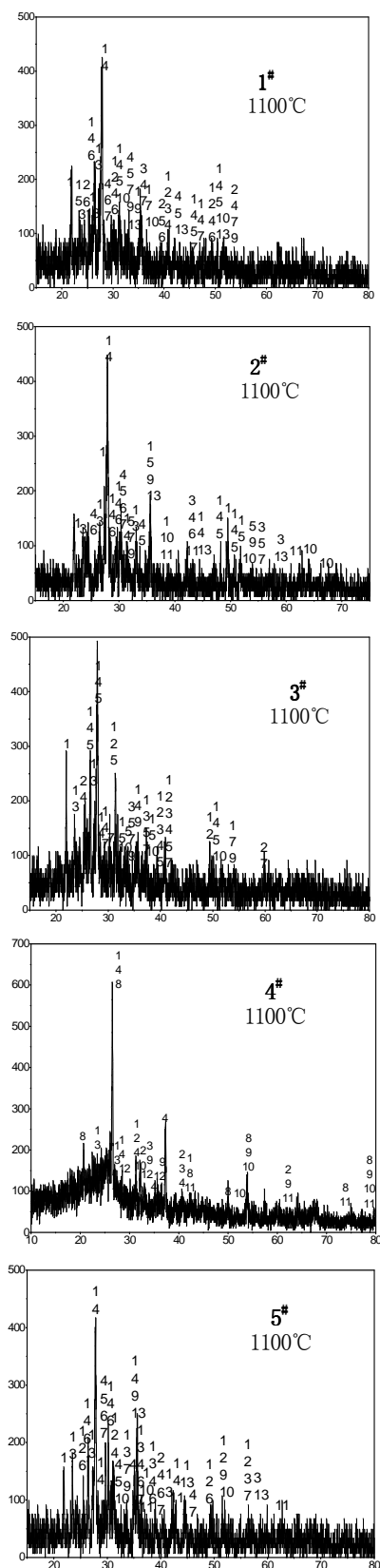


Figure 4. XRD pattern of sulfur retention from wastes in 1100°C (1- $\text{CaAl}_2\text{Si}_2\text{O}_8$; 2- CaSO_4 ; 3- $\text{Ca}_3\text{Al}_6\text{O}_{12}\cdot\text{CaSO}_4$; 4- $2\text{C}_2\text{S}\cdot\text{CaSO}_4$; 5- $\text{Ca}_2(\text{SiO}_4)$; 6- CaSiO_3 ; 7- $\text{Ca}_3\text{Fe}_2(\text{SiO}_4)_3$; 9- Fe_2O_3 ; 10- CaO ; 11- MgO ; 12- Al_2SiO_5 ; 13- Al_2O_3)

At 1100°C, after white clay, carbide slag and limestone are added; SO_2 is captured at first and late stage. The ratios of SO_2 released reduce 54%, 38% and 53% respectively. After salt slurry and red mud are added, though they can capture the release of sulfur at first stage, they can do nothing to the sulfur released at late stage. The ratios of SO_2 released reduce only 3%-10%. Desulphurization efficiency is decreased significantly.

XRD pattern of sulfur retention at 1100°C shows that the main desulphurization products of white clay and carbide slag are CaSO_4 , $\text{Ca}_3\text{Al}_6\text{O}_{12}\cdot\text{CaSO}_4$ and $2\text{C}_2\text{S}\cdot\text{CaSO}_4$ (Figure 4). The diffraction maximum of $\text{Ca}_3\text{Al}_6\text{O}_{12}\cdot\text{CaSO}_4$ and $2\text{C}_2\text{S}\cdot\text{CaSO}_4$ is significant, showing large quantity. It is obvious that during the reaction process, considerable part of CaSO_4 forms thermal stable phases $\text{Ca}_3\text{Al}_6\text{O}_{12}\cdot\text{CaSO}_4$ and $2\text{C}_2\text{S}\cdot\text{CaSO}_4$, which enhances the sulfur capture ability.

Figure 4 shows that compared with desulphurization product at 800°C, the main desulphurization product of salt slurry and red mud are $\text{Ca}_3\text{Al}_6\text{O}_{12}\cdot\text{CaSO}_4$ and $\text{Ca}_5(\text{SiO}_4)_2\text{SO}_4$ at 1100°C, only with a small amount of CaSO_4 . There is even no CaSO_4 in red mud. From the diffraction maximum value, the value of $\text{Ca}_3\text{Al}_6\text{O}_{12}\cdot\text{CaSO}_4$ and $\text{Ca}_5(\text{SiO}_4)_2\text{SO}_4$ is small, showing smaller amount and poor desulphurization efficiency. Salt slurry and red mud contains alkali metal compound and a considerable part of Ca^{2+} reacts with such compound and forms $\text{CaAl}_2\text{Si}_2\text{O}_8$, $\text{Ca}_2(\text{SiO}_4)$, CaSiO_3 and $\text{Ca}_3\text{Fe}_2(\text{SiO}_4)_3$ etc. as shown by Figure 4. It decreases calcium's active center and so it can't capture high-temperature sulfur and SO_2 decomposed by CaSO_4 , which weakens sulfur capture ability.

At 1200°C, when experimental samples are added, desulphurization efficiency is poor and the ratios of SO_2 released reduce only 3%-19%. The reason is that because of serious high temperature sintering of experimental sample, sulfate produced at initial reaction stage is rapidly decomposed again, which deteriorates wastes' sulfur capture ability. Wastes basically cannot capture the release of sulfur at such temperature.

To sum up, after white clay and carbide slag are added, the amount of SO_2 released is reduced significantly at first and late stage. White clay and carbide slag could capture the release of sulfur at 800-1100°C. After salt slurry and red mud are added, the amount of SO_2 released is reduced significantly at first stage. Salt slurry and red mud could capture the release of sulfur at 800-900°C. But when the experimental temperature is above 1000°C, the sulfur capture abilities of them depress. After limestone is added, the amount of SO_2 released is hardly reduced at first stage. Its resistance to SO_2 precipitation is lower to experimental wastes at 800-900°C. But when the experimental temperature rises to 1000°C, limestone could capture the release of sulfur.

3.2 Temperature Characteristics of Wastes

As is shown by Figure 2, when white clay and carbide slag are added, the ratios of SO_2 released reduce over

50% and over 40% respectively at 800-1100°C. And at 900-1000°C, the ratios could reduce over 70% and 56% respectively. The range of optimum desulphurization temperature is wide and desulphurization performance is good. White clay and carbide slag represent good microstructure characteristics. So sulfation reaction could process in the inner particles and high temperature desulphurization phase is easily formed at high temperature, which makes their desulphurization performance better. When salt slurry and red mud are added, the ratios reduce over 40% at 800-900°C, showing better sulfur capture ability. When the temperature rises to 1000°C, because of poor sulfur capture ability at late stage, decomposition of desulphurization product and serious sintering, the sulfur capture abilities of them depress. Limestone has poor desulphurization capacity at 800-900°C, because of its hard calcinations and bad microstructure. With the rise of temperature, limestone is calcined fully, which improves the sulfur capture ability a little. When temperature rises to 1200°C, industry alkaline wastes and limestone hardly have any desulphurization capability because of serious sintering. So the optimum desulphurization temperature window of white clay is 800-1100°C, carbide slag's is 800-1050°C, and salt slurry and red mud's is 800-950°C.

3.3 Microstructure Characteristics of Wastes

The inner microstructure of desulphurization sorbent greatly influences its sulfur capture ability [9,10]. Micro-pore structure of samples was studied by mercury porosimeter in this paper. The samples include original samples and test samples after calcinations at 850°C and 1050°C. The testing results were analyzed and characteristic parameters were got, including pore size distribution, porosity and specific area (Table 3 and Table 4).

Table 3 and Table 4 show that the pore structure of wastes' and limestone's original samples are greatly different. The pore size distribution of wastes is similar to that of limestone, with micropore and mesopore taking the main part. But porosity and specific area of wastes are higher than that of limestone.

Table 3. Aperture and porosity of test sample

Sample	Original sample		850°C Calcined sample		1050°C Calcined sample	
	Pore size (μm)	Porosity (%)	Pore size (μm)	Porosity (%)	Pore size (μm)	Porosity (%)
white clay	0.004-0.2	13.216	0.0045-0.3	19.665	0.005-1	22.329
carbide slag	0.004-0.2	25.083	0.0045-0.3	21.717	0.005-1	15.166
red mud	0.004-0.2	13.269	0.005-0.045	25.549	0.5-1	6.073
limestone	0.011-0.302	0.099	0.008-2.5	16.175	0.005-1	19.354

Table 4. Specific area of test sample (m^2/g)

Sample	Original sample	850°C Calcined sample	1050°C Calcined sample
	white clay	2.915	8.267
carbide slag	15.069	8.602	6.269
red mud	7.715	9.602	2.915
limestone	0.097	3.715	3.071

This makes wastes react with SO_2 more easily at initial reaction stage. Porosity and specific area of limestone are smaller, which makes limestone have poor sulfur capture ability at initial reaction stage.

The pore structure of white clay after calcinations at 850°C is improved. The pore size distribution is wider. Porosity and specific area increase greatly, which makes SO_2 diffuse easily and sulfation reaction process goes further in the inner particles. With the rise of temperature, its pore size distribution becomes further wider, and porosity increases continuously. Because of sintering, its specific area decreases a little at 1050°C. But the general situation is better. This makes it still represents higher sulfur capture ability, which is in accordance with the above desulphurization experiment results. Carbide slag represents porous structure and its specific area is huge. With calcinations reaction and sintering reaction go simultaneously, the pore size distribution of carbide slag becomes wider, which makes SO_2 deep into the particles easily and makes sulfation reaction go further. Though its specific area and porosity decrease with rise of temperature, they are still higher, and so carbide slag still represents better sulphur capture ability. Red mud contains large amount of Al_2O_3 and Fe_2O_3 . They react with produced CaO and form $\text{CaO}\cdot\text{Al}_2\text{O}_3$, $3\text{CaO}\cdot\text{Al}_2\text{O}_3$, $\text{CaO}\cdot\text{Fe}_2\text{O}_3$ and $2\text{CaO}\cdot\text{Fe}_2\text{O}_3$ at 850°C, which makes microstructure worse, the quantity of macropore and mesopore decrease. The pore size distribution of red mud becomes narrow after calcinations. Liquid eutectic solution accelerates ion migration and diffusion, which destroys crystal lattice of CaO . Irregular pore is formed. The specific area and porosity of red mud increase. With rise of temperature, $\text{CaO}\cdot\text{Al}_2\text{O}_3$, $3\text{CaO}\cdot\text{Al}_2\text{O}_3$, $\text{CaO}\cdot\text{Fe}_2\text{O}_3$ and $2\text{CaO}\cdot\text{Fe}_2\text{O}_3$ accelerate sintering. Pore structure of red mud changes, which causes plugging of pore or formation of molten pore or macropore. The specific area and porosity decrease rapidly and sulphur capture ability is reduced. The change of limestone's microstructure with rise of calcination temperature is similar to that of white clay's. But porosity and specific area of limestone are lower and its sulphur capture ability is worse than white clay's.

4. Conclusions

The desulphurization characteristics of samples had been studied at 800-1200°C. White clay and carbide slag could capture the release of sulfur at 800-1200°C. Salt slurry and red mud could capture the release of sulfur at first stage at 800-900°C, and when temperature rises to 1000°C, the sulfur capture ability of them decreases. Within the range of experimental temperature, industry alkaline wastes represent better temperature characteristics. The optimum desulphurization temperature window of white clay is 800-1100°C, carbide slag's is 800-1050°C, and salt slurry and red mud's is 800-950°C. According to the test of mercury porosimeter, the original samples and calcined samples of the wastes have better pore size dis-

tribution, higher porosity and specific area. This makes SO₂ deep into the inner particles and sulfation reaction go further. But because of sintering, specific area and porosity of red mud become smaller with rise of temperature. Sulfur capture ability of red mud decreases. Compared with limestone, industry alkaline wastes represent better desulphurization characteristics and temperature characteristics. They may be a new sort of desulphurization sorbent.

5. Acknowledgment

This research was supported by National Natural Science Foundation of China (No. 59976019) and Shandong Natural Science Foundation (No.Y2003F07 and No.Y 2006F63) and Zibo Research Programme (No. 20062502).

REFERENCES

- [1] C. M. Lu and Y. Z. Wang, "Study on evaluation regularities and absorption characteristics of sulfur during coal combustion," *Journal of Coal Science & Engineering*, 4, pp. 80–86, 1999.
- [2] J. Cheng, J. H. Zhou, and J. Z. Liu, "Dynamic characteristics of catalytic clean coal combustion with additives," *Proceedings of the CSEE*, 22, pp. 128–131. 2002.
- [3] J. N. Wang and D. F. Chen, "Experiments on the utilization of discards from the chemical industry substitutes for the conventional absorbents of desulfurization," *Energy Research and Information*, 16, pp. 45–48, 2000.
- [4] S. Q. Cheng, Y. B. Feng, and C. M. Lu, "Study on the kinetics of desulphurization of shells," *Proceedings of the CSEE*, 25, pp. 80–85, 2005.
- [5] Y. Tan, C. T. Li, and G. M. Zeng, "Promotion effect of additives on sulfur capture during coal combustion with carbide slag," *Journal of Fuel Chemistry and Technology*, 33, pp. 767–770, 2005.
- [6] K. H. Han, J. L. Zhao, and C. M. Lu, "Kinetic analysis of the effect of additive on the desulfurization activity," *Environmental sciences*, 27, pp. 219–223, 2006.
- [7] Z. S. Yuan, D. Y. Wu, and S. D. Wang, "Study on sulfur retention of integrated additive during coal combustion," *Journal Fuel Chemistry and Technology*, 30, pp. 36–40. 2002.
- [8] K. H. Han and C. M. Lu, "Study on the characteristics of sulfurous pollutant with different coal in one-dimensional flame," *Journal of China Coal Society*, 29, pp. 594–597, 2004.
- [9] G. A. Simons and A. R. Garman, "Small pore closure and the deaction of the limestone sulfation reaction," *AICHEJ*, 32, pp. 1491–1499, 1986.
- [10] S. K. Mahuli, R. Agnihotri, and C. Shrinivas, "Pore-structure optimization of calcium carbonate for enhanced sulfation," *AICHEJ*, 43, pp. 2323–2335, 1997.

The Online Assessment of Electric Distribution Network Load Capability

Haoming Liu¹, Zhenkun Li¹, Kun Yu¹, Xingying Chen¹

¹College of Electrical Engineering, Hohai University, Nanjing, P. R. China
Email: liuhaom@hhu.edu.cn

Received January 27th, 2009; revised February 20th, 2009; accepted March 2nd, 2009.

ABSTRACT

To improve the security and reliability of a distribution network, several issues, such as influences of operation constraints, real-time load margin calculation, and online security level evaluation, are with great significance. In this paper, a mathematical model for load capability online assessment of a distribution network is established, and a repetitive power flow calculation algorithm is proposed to solve the problem as well. With assessment on three levels: the entire distribution network, a sub-area of the network and a load bus, the security level of current operation mode and load transfer capability during outage are thus obtained. The results can provide guidelines for prevention control, as well as restoration control. Simulation results show that the method is simple, fast and can be applied to distribution networks belonged to any voltage level while taking into account all of the operation constraints.

Keywords: *Distribution Network, Online Security Assessment, Loading Capability, Variable Step-Size Repetitive Power Flow, Load Transfer*

1. Introduction

The distribution network transmits the electricity from load centers to the customers. The accurate real-time assessment of its load capability and the allowable load margin is of great significance. Because the sufficient power supply capability is a prerequisite to ensure the distribution network operate securely and reliably. Especially with the development of distribution management system (DMS) and distribution automation system (DAS), the selection of an economic operation mode of the distribution network with the variation of the load is possible [1], which makes it more necessary to evaluate the load capability of the current operation, and to change the operation mode immediately in order to avoid violation and faults. Only in this way it is possible to ensure the security and reliability while pursuing the economic object. When there are faults have taken place in the distribution network, the load of the non-fault section should be transferred to its adjacent feeder immediately in order to reduce the range and time of outage. Thus it is needed to evaluate the load acceptability of its adjacent feeder to determine the load quantity that can be transferred. For these reasons, it is of great significance to investigate the load capability of a power distribution network.

With the in-depth going of the electricity market, the research of the load capability of transmission networks is paid more attention and certain achievements are obtained [2,3,4]. But the research of load capability of distribution network is little. The few studies were only

through the statistical indexes [5,6,7,8], such as the capacity to load ratio of substations and the average of line load ratio, which can be just used for the qualitative assessment in general terms. The results may be helpful to the distribution network planning and upgrading, but can't provide any information used for the real-time control of the distribution network. Furthermore, these methods can not take into account the constraint of bus voltage limits. So it is necessary to propose a feasible load capability assessment method and an effective algorithm to meet the problem while considering various operation constraints.

In this paper, the mathematical model of the load capability online assessment of distribution network is established, and the improved variable step-size repetitive power flow is proposed to solve the problem. The evaluation is carried out in three perspectives: the entire distribution network, a sub-area of the network and a load bus. According to the assessment results of the whole network, the security of the current operation condition is divided into three levels: high, medium and low, which determines weather or not to take the prevention control. During outage the load transfer capability is obtained through the load capability assessment of a load bus. Simulation is carried out on two distribution networks, and the results show that the proposed method is simple and fast, and can be applied to distribution networks belonged to any voltage level while taking account into all the operation constraints.

2. The Real-Time Assessment of Distribution Network Load Capability

2.1 The Mathematical Model of the Load Capability Assessment

The load capability of a distribution network refers to how much load the network can sustain before any operation constraint violated when given a load variation pattern, such as the constraints of bus voltage or branch power. It is determined by the operation mode of the distribution network and the load variation pattern. The restructuring of distribution network, the changes of transformer taps or the switching of reactive power compensation equipments would have impacts on the load capability. So it is time-varying and must be assessed online based on the practical operation condition.

In the power transmission system the main factors that limit the power transmission capability are thermal limitation, line-voltage-drop limitation and stability limitation [2]. In the process of assessment of distribution network, the former two factors are taken into account and the stability limitation is ignored here. In this paper, the maximum power that is determined by the thermal limit of lines and the rated power of transformers are used as their upper load limits. And assuming that the higher voltage level power network can provide sufficient electricity, and the load growth pattern is that the load growth is proportional to the actual load.

According to the above, the objective function of load capability of distribution network can be formed as

$$\max S = \sum_{j \in D} (S_{0j} + kS_{dj}) \quad (1)$$

where, D is the area to be assessed, the total number of the bus in D is N , S is the maximum load that can be supplied in area D , S_{0j} and S_{dj} are the actual load and the base quantity of the load variation of bus j respectively, here we take $S_{dj} = S_{0j}$, k is the multiples of load growth. So the first item of the objective function is the sum of all the actual loads. In this paper, D is considered as three instances, they are the whole network, a sub-area of the distribution network, and just one node.

The constraints include power flow constraint, the capacity limits of lines and transformers, and voltage magnitude limits. The formulas are as follows:

$$A\mathbf{i} = \mathbf{I} \quad (2)$$

$$V_{Lk} \leq V_k \leq V_{Uk} \quad (3)$$

$$i_l \leq i_{l\max} \quad (4)$$

$$S_t \leq S_{t\max} \quad (5)$$

where A is the bus-branch conjunction matrix, \mathbf{i} is the branch current vector, \mathbf{I} is the nodal injection current vector, V_k , V_{Lk} and V_{Uk} are the voltage magnitude, lower and upper limits of the bus k respectively, i_l and $i_{l\max}$ are

the current and its upper limit of line l , S_t and $S_{t\max}$ are the power flow and its upper limit of transformer t .

2.2 The Classification of Load Capability Assessment

According to the area to be assessed, the load capability assessment can be divided into three categories.

1) The assessment for the whole network

In this type of assessment, the loads power of all the buses in the whole distribution network will increase proportionally and continuously until any constraint works. Based on the maximum total power, the load capability and how much more load the network can sustain will be known under the certain operation condition. So it can be used to judge whether the current operation condition could bear a certain load fluctuations, also provide a signal to determine whether the prevention control should be started up.

Assuming if the loads increase to be K times of the original loads when reaching a constraint, that is, if the loads increase more there will be a violation occurrence. Thus, K could be used to indicate the load capability. In Equation (1), when S reaches maximum, the value of variable k is expressed as k_{\max} , then $K=1+k_{\max}$. It is obvious that the value of K is greater than or equal to 1. The larger its value is, the better the load ability is and the higher the security level is. So K can be used as a security index of the distribution network. In this paper, the security level is defined as three grades: high, medium and low. If $K > 2$, the security level is high, which means if all the loads is doubled the distribution network can still run normally, and no prevention control is needed. If $1.5 < K < 2$, the allowable load margin is acceptable and the security level is medium. Although the prevention control is not needed yet, the operation condition should be paid more attention. If $1 < K < 1.5$, the security level is considered as low, prevention control should be taken immediately to change the current operation condition. Otherwise there would be violation occurrence if the load has any fluctuation.

2) The assessment for a sub-area

The loads in the sub-area to be assessed increase proportionally and other loads remain unchanged until a constraint works. The load capability acquired could be used to judge whether new load can be connected into the sub-area and how much loads can be connected.

3) The assessment for a load bus

Except the load of the bus that is assessed, all the other loads remain unchanged. So the maximum load that the bus can supply is obtained. The result is very useful for restoration control, because generally the adjacent feeders are connected together by tie switches which are open in normal operation, once there is a fault in a feeder, the loads of which should be translated to its adjacent feeders from tie switches as more as possible in order to reduce the range and time of outage. In the process of translation, the load capability of the bus, that will accept new load, should be assessed in order to know how much load can

be transferred. Many literatures on service restoration neglected the translation capability, and made the assumption that the adjacent feeders can accept all the loads that need to be translated [9]. This is inconsistent with the fact.

3. The Repeated Power Flow and its Application in Load Capability Assessment

3.1 The Introduction of Repeated Power Flow

The essence of load capability assessment for the distribution network is to acquire a critical point under a given load increase pattern. At the critical point, even if there is a little load incensement, there will be a violation occurrence. So the critical point means the maximum load that a network or a bus can supply, and then the load capability will be determined. Repeated power flow (RPF) is one of the effective methods to calculate the critical point. The core idea is while varying a parameter continuously, the power flow calculation is done repeatedly until there is a violation occurrence. RPF has been used in the calculation of the available translation capability (ATC) in the transmission network [10,11].

The realization process of the assessment based on RPF is as follows, based on the actual operation condition and the load variation pattern S_d , increasing the loads according an appropriate step h , calculating the power flow, judging if there is a violation, if not increasing the load continuously, otherwise decreasing step size. Iteration is done until the tolerance meets the requirement. The operation point that just one constraint action is the critical point and the load at the operation point is the maximum load the network can supply.

3.2 The Strategy of Step Size Adjustment

In the process of assessment the selection of an appropriate step size h is very important. If the step size is large the accuracy would be inadequate, or if the step size is too small the algorithm would converge slowly. In this paper, automatic step size variation method is introduced to search the critical point. If in one iteration there is no violation the step size will remain unchanged and search forward continuously. Otherwise, if one violation occurs, the step size will be reduced by half. The iteration is repeated continuously until the step size h is reduced to satisfy the accuracy requirement. The detailed steps are as follows:

- 1) Fix the initial step size $h_0 > 0$ and convergence tolerance $\varepsilon > 0$;
- 2) Define the load variation pattern S_d , let S be the actual load S_0 , $h=h_0$, $K=1$;
- 3) If $h > \varepsilon$, go to next step; else if $h < \varepsilon$, the calculation is ended and return S and K . S means the maximum load capability. So $S-S_0$ is the allowable load margin. K is the ratio of the maximum load that the network can supply and the actual load;
- 4) Calculate $S'=S+hS_d$;

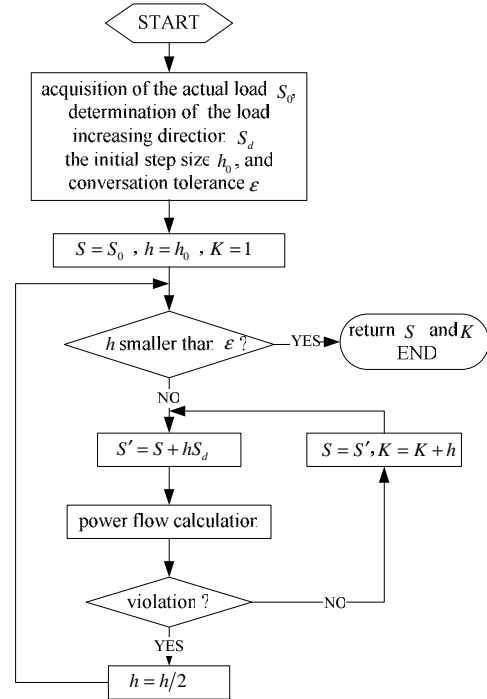


Figure 1. Flow chart of distribution network load capability assessment based on improved variable step-size RPF

5) Run power flow calculation based on the load S' to check if there is any violation, if not continue next step, otherwise jump to step 7);

6) Let $S=S'$, jump to step 4);

7) Reduce the step size by half, $h=\frac{h}{2}$, go to step 3).

The flow chart of distribution network load capability assessment based on RPF is as shown in Figure 1.

3.3 The Advantages of Variable Step-Size RPF

The algorithm for load capability assessment used in this paper has following advantages:

The application range is wide and all the constraints that the distribution network has can be taken into account; The algorithm is simple and the results are accurate; The burden of the variable step-size RPF calculation is low. Generally the maximum load capability is not far away from the actual operation point. So in the computation process if the initial step size $h_0=2$, along with the load increment there will be violation occurrence within about 4 times iteration. If the convergence tolerance $\varepsilon=2^{-10}$, the power flow calculation times is not more than 14 in the whole assessment process. So the burden of calculation is lower absolutely compared with the intelligence algorithms, and it is suitable to solve load capability assessment problem online.

4. Simulation Analysis

In order to verify the feasibility of the proposed algorithm, two examples are simulated. One is a radial distribution network with long feeders of 10kV. The other is a multi voltage level distribution network.

4.1 Case 1

Figure 2 shows the network configuration of the test system that is from an actual city distribution network. The voltage level is 10 kV. It consists of 42 buses, 41 branches and 24 distribution transformers, all the branches are buried or aerial cables. Bus 20 is connected with an adjacent feeder through a tie switch. The sum of current load is $1610+j700$ kVA. The upper limits of transformers and cables are their rated power and thermal limits respectively. The allowable fluctuation range of voltage magnitude is $1 \pm 5\%$.

MATLAB[®] 6.5 is adopted here to program. Running the power flow calculation, it can be known that the lowest voltage in the distribution network is 0.972 and the power flow in every branch is allowable. Assuming the initial step size $h_0=2$ and the convergence tolerance $\varepsilon=10^{-3}$, load capability assessment is carried out in three aspects.

1) The assessment for the whole network

The assessment for the whole network is convergent after 11 iterations with the CPU time for about 0.437 seconds. From the assessment results, it can be known that the network can sustain $2848.9+j1238.7$ kVA loads, which is 1.77 times of the base instance. So the security meets requirement and the current operation condition needn't to be changed.

2) The assessment for a sub-area

Assuming the sub-area consists of 6 buses, they are bus 15-20. The assessment is convergent after 12 iterations, and the maximum loads in the sub-area can reach $1491.5+j648.5$ kVA under the current operation condi-

tion while other loads remain unchanged, which is 3.3848 times of the base instance, and the voltage magnitude of bus 20 reaches its lower limit.

3) The assessment for a load bus

In the network, bus 20 is connected to another feeder. If there is a fault in the feeder, the loads can be transferred to bus 20 via closing the tie switch. The load capability assessment of bus 20 is $1007.2+j437.9$ kVA, and the load transferred to bus 20 should be less than the amount. Otherwise, the power flow in the branch between bus 2 and 3 would exceed its upper limit.

In the simulation process it is found that the voltage magnitude constraint often effects and limits the load capability, so it is not reasonable to assess the load capability without voltage magnitude constraint.

4.2 Case 2

The second simulation example, which is shown in Figure 3, is part of a multi voltage level actual network, including three 220kV substations, four 110kV substations and six 35kV substations. There are 51 buses, 7 three-winding transformers, 10 double winding transformers and 25 lines. There are tie lines between the 3 220kV substations. However, in the normal operation state they are running separately in order to avoid electromagnetic loop. So the whole distribution network can be divided into three independent areas by the dash and dot line as shown in Figure 3. The load in all of the whole distribution network is $121.88\text{MW}+68.36\text{MVar}$. The allowable fluctuation range of voltage magnitude of 35kV and 110kV is $1 \pm 10\%$ and that of 10kV is $1 \pm 5\%$.

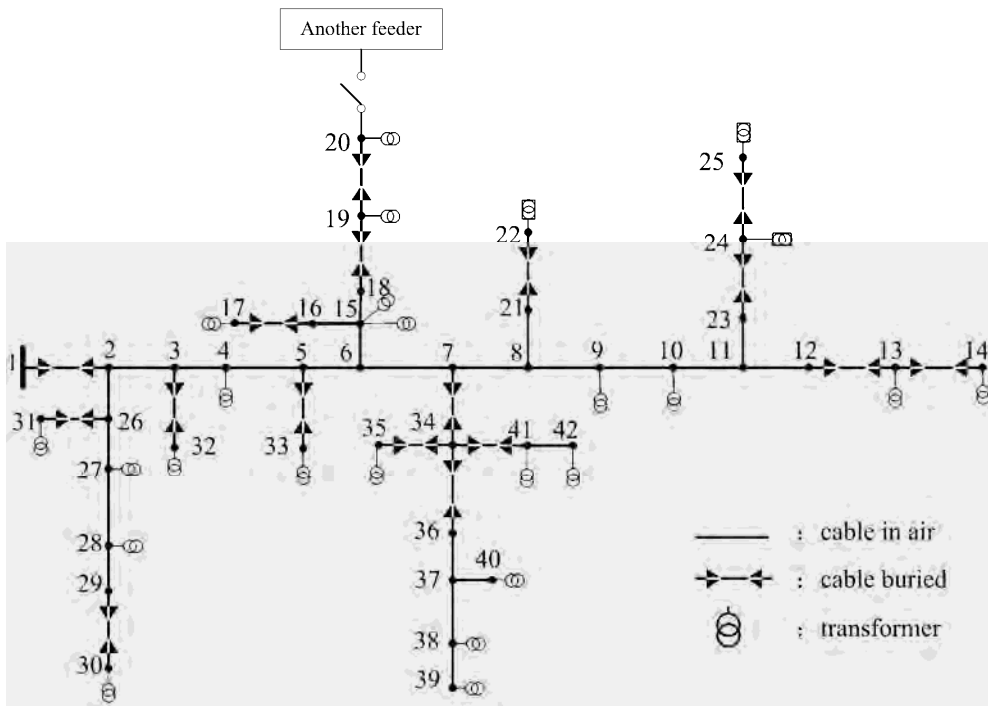


Figure 2. A 10 kV distribution network consists of 42 buses

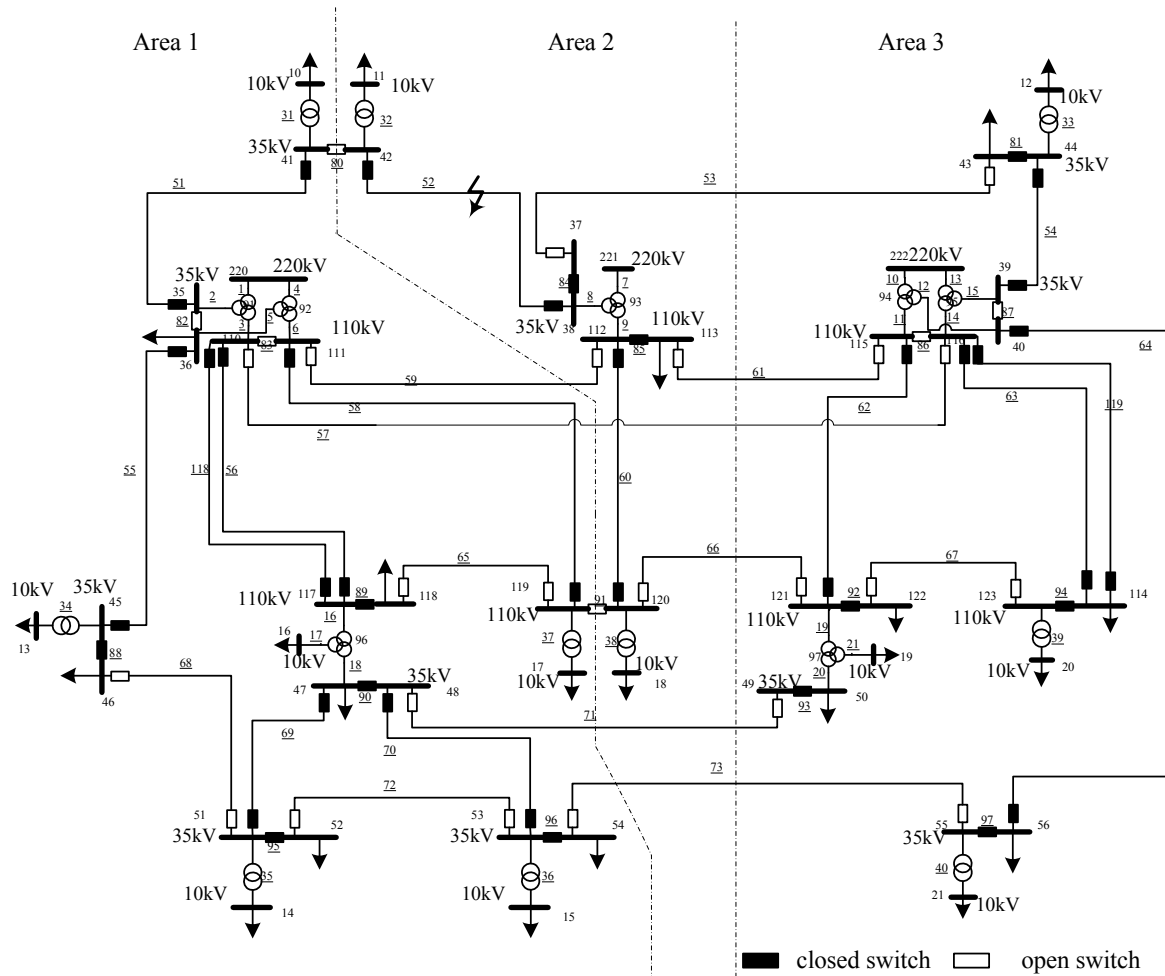


Figure 3. A multi-voltage level distribution system containing 51 buses

Table 1. The loading capability evaluation results of the three areas

		Area 1	Area 2	Area 3
Base instance	Active power (MW)	51.09	22.19	48.60
	Reactive power(MVar)	32.11	9.36	26.89
Remaining load margin	Active power (MW)	38.17	31.43	27.50
	Reactive power(MVar)	23.99	13.26	15.22
Maximum load increase multiple <i>K</i>		1.7471	2.4164	1.5659
Active constraint		The power of transformer among Bus 117, 16 and 47 exceed limit.	The voltage of Bus 11 is over limit.	The power of transformer among Bus 222, 115 and 40 exceed limit.

1) The load capability assessment of 3 areas is all carried out and the results are shown in Table 1. The load increase multiple *K* of Area 2 is maximal among the 3 areas, which is up to 2.4164. So the load fluctuate enduring ability is best in the area. The remaining load increase allowance of Area 1 is maximal, which is 38.1693MW + 23.9894MVar. The security of the 3 areas all meets requirements.

2) If there is a short circuit fault in line 52, the switches on the two ends of the line should be opened in order to isolate the fault. And the load supplied by Bus 42 should be transferred to Bus 41 of Area 1. Thus the load capability of Bus 41 should be evaluated real timely to decide

whether the lost load can be restored, that is, whether or not some load should be cut.

The maximum load that can be supplied by Bus 41 can be obtained by the method proposed in the paper, and the value is 19.12MW+12.70MVar, otherwise the current of Line 51 will exceed limit. So the remaining load margin is 13.52MW+8.98MVar, which can supply the entire lost load. Therefore no load needs to be cut; just close the tie switch 80 then the entire load will be restored.

As discussed above, the load capability assessment results, such as the maximum load that the network can supply and the allowable load margin, can provide a sci-

entific signal to determine whether the prevent control or restoration should be started.

5. Conclusions

Many research works on the distribution network reconfiguration have been done in order to minimize the power loss by adjusting the operation mode with the load variation. Although the total loss decreases, it brings forward new challenges to the distribution network's security and reliability. This paper proposed an online load capability assessment strategy, which could figure the security level timely. The allowable load margin acquired can be used to determine whether to take the prevention control. The maximum load that can be transferred after outage is of great significance in the restoration control. The variable step-size RPF algorithm has a low calculation burden and is suitable to solve load capability assessment problem online.

REFERENCES

- [1] S. Koizumi, M. Okumura, and T. Yanase, "Application and development of distribution automation system in TEPCO," *Proceedings of IEEE Power Engineering Society General meeting*, Vol. 3, pp. 2429–2435, 2005.
- [2] R. D. Dunlop, R. Gutman and P. P. Marchenko, "Analytical development of loadability characteristics for EHV and UHV transmission line," *IEEE Transactions on Power Apparatus and System*, 98, pp. 606–613, 1979.
- [3] H. D. Chiang, A. J. Flueck, K. S. Shah, and N. Balu, "CPFLOW: A practical tool for tracing power system steady-state stationary behavior due to load and generation variations," *IEEE Transactions on Power Systems*, 10, pp. 623–634, 1995.
- [4] S. Greene, I. Dobson and F. L. Alvarado, "Sensitivity of transfer capability margins with a fast formula," *IEEE Transactions on Power Systems*, 17, pp. 34–40, 2002.
- [5] *Energy and Electric* [1993] No. 228. (1999), "The planning and designing rule of urban power network," 1st edition, China Electric Power Press, Beijing.
- [6] X. Li, P. Li, X. Zhu, G. Peng, and Y. Ou, "Evaluation construction size of district high voltage distribution networks," *Automation of electric power systems*, 31, pp. 46–50, 2007.
- [7] R. E. Brown, A. P. Hanson, H. L. Willis, F. A. Luedtke, M. F. Born, and N. C. Raleigh, "Assessing the reliability of distribution systems," *IEEE Computer Applications in Power*, 14, pp. 44–49, 2001.
- [8] J. Zhang, D. Luo, J. Yao, and W. Li, "Research on value of capacity-load ratio in urban power network planning based on the economical analysis," *Relay*, 35, pp. 39–43, 2007.
- [9] S. Curcic, C. S. Ozveren, and K. L. Lo, "Computer-based strategy for the restoration problem in electric power distribution systems," *IEEE Proceedings-Generation, Transmission and Distribution*, 144, pp. 389–398, 1997.
- [10] O. Yan and C. Singh, "Assessment of available transfer capability and margins," *IEEE Transactions on Power Systems*, 17, pp. 463–468, 2002.
- [11] M. H. Gravener, and C. Nwankpa, "Available transfer capability and first order sensitivity," *IEEE Transactions on Power Systems*, 14, pp. 512–518, 1999.

Complex Dynamics Analysis for Cournot Game with Bounded Rationality in Power Market

Hongming Yang¹, Yongxi Zhang¹

¹College of Electrical and Information Engineering, Changsha University of Science and Technology, China.
Email: yhm5218@hotmail.com

Received January 20th, 2009; revised February 11th, 2009; accepted February 23rd, 2009.

ABSTRACT

In order to accurately simulate the game behaviors of the market participants with bounded rationality, a new dynamic Cournot game model of power market considering the constraints of transmission network is proposed in this paper. The model is represented by a discrete differential equations embedded with the maximization problem of the social benefit of market. The Nash equilibrium and its stability in a duopoly game are quantitatively analyzed. It is found that there are different Nash equilibriums with different market parameters corresponding to different operating conditions of power network, i.e., congestion and non-congestion, and even in some cases there is not Nash equilibrium at all. The market dynamic behaviors are numerically simulated, in which the periodic or chaotic behaviors are focused when the market parameters are beyond the stability region of Nash equilibrium.

Keywords: Chaos, Dynamic Model, Nash Equilibrium, Power Market

1. Introduction

Some foundation industries, such as electric power, aviation, telecommunication, railroad, etc., are traditionally thought of having natural monopoly characteristics. With the development of technology, economy and society, in recent years these industries have been undergoing a market reformation tide of deregulation and competition, in order to reduce the cost and price of monopoly industry and promote the enhancement of social economy benefit. All these industries have the natural monopoly network with the complex inherent physical property, by which the market participants can provide commodity services. The complex monopoly network causes the reformation and operation of market to be more complicated and difficult than that of general commodity market, especially for the reformation of electric power industry.

In the process of reformation and operation of market, how to effectively master and supervise the dynamic market behaviors is an important research topic, especially for the power market whose reformation is carried out in its infancy stage. Taking an extreme example of California power market, the neglected study of the dynamic market behaviors led to a severe situation causing the electric power wholesale price to rise sharply and thus affecting the power supply to a lot of customers. This happened in less than three years of market operation, which has made a great impact on the economy of California and even the USA [1].

The system of market economy is essentially a dynamic system, which is mathematically represented by the differential or difference equations. In the dynamic

theory of economics, there are a lot of differential or difference dynamic models, such as the classical cobweb model describing the variation of the supply and demand, the Cournot dynamic model reflecting the oligopoly market, the Haavelmo model describing the economic growth problem, and so on [2,3]. Based on these models, the analysis and control of the stable, periodic and chaotic dynamic evolution of the market economy system are investigated, and a series of results have been yielded [4,5]. However, the complex inherent physical property of network and the particularity of market transaction in the market with the monopoly network are not taken into account in these models and methods. Therefore, in view of the characteristics of power market, the research on the dynamic evolution of power market is carried out by some scholars.

The research on the dynamics of power market was first launched by F. L. Alvarado *et al.*, via a set of one-order differential equations of power generations and consumptions. This work provides insights to the conditions for the evolving process converging to the market equilibrium, i.e., the stability condition of power market [6,7]. With the same dynamic model, a series of sufficient conditions are given to determine the stability of power market in Reference [8]. Reference [9] establishes the difference equations by taking the electricity price as a variable, and analyzes the stability condition needed for the electricity price converging to the equilibrium. Although the results achieved are interesting, these models are established based on a perfect competitive model. It

neglects the game behaviors of generation companies as well as their impacts on the electricity price, and thus it can not rationally describe the actual power market.

In order to accurately simulate the game behaviors of the market participants, the oligopolistic game models in economics are further introduced to research the dynamics of power market. References [10,11] adopt the Cournot model to establish the differential equations of the dynamic power market. Then, the market equilibrium of the generation quantities is calculated under the given demand function, and the varying curve of electricity price converging to the equilibrium is numerically simulated. In References [12,13], the dynamic differential or difference equations are established based on the perfect competitive model, the Stackelberg game model and the Cournot game model, respectively. However, the constraints of power network and their impacts on the electricity price are not taken into account, nor are the stability analysis of the market equilibrium involved. In Reference [14], the evolutionary game is introduced to establish the dynamic evolutionary differential equations by taking the generation bids as variables. However, the constraints of power network are not taken into account, too.

Consequently, not only the rational game behaviors of market participants but also the inherent physical properties of power network need to be considered in the dynamic modeling of power market. In addition, due to the complex dynamic characteristics of the actual power market, in some cases there exists no market equilibrium at all, or even if there is, it might lie in the non-stability region of the market equilibrium. It is significant for the market operators to study the dynamic behaviors of the power market associated with these cases.

Therefore, the aim of this paper is to make a thorough study concerning the dynamic Cournot game behaviors of the power market with bounded rationality under the consideration of the power network constraints. The following aspects are focused:

1) A new dynamic Cournot game model of power market, represented by the difference equations embedded with the maximization problem, is proposed. The remarkable characteristic of the model is twofold: it adopts a dynamic adjustment where the limit point is the Nash equilibrium of power market; and the system of discrete difference equations embedded with the maximization problem considers the constraints of power network.

2) The existence and stability of Nash equilibrium for a duopoly game are quantitatively analyzed with different market parameters under different operating conditions of power network;

3) The dynamic behaviors of power market, especially the periodic and chaotic dynamic behaviors when the market parameters are beyond the stability region of equilibrium, are numerically simulated.

2. Dynamic Cournot Game Model of Power Market with Bounded Rationality Considering Network Constraints

2.1 Dynamic Cournot Game Model with Bounded Rationality

Power market is different from general competitive commodity market, in which the production of power energy needs very high cost and technology, and there are finite electric power producers. This nature of electric power industry implies that power market does not have the characteristic of perfect competitive market, but should belong to an oligopolistic market. In economics, several kinds of game models have been proposed to simulate the oligopolistic behaviors of market participants. The Cournot game model is most commonly used which simulates the competition of output quantities between the oligopolists [15].

Recently, the static Cournot models are applied to analyze the Nash equilibrium of power market [16,17]. In this case, the game of market participants is done based on a fully rationality. Each participant has complete market information (including the competitors' profit functions) when he makes his optimal production decision. If there is a Nash equilibrium in the market, the oligopolists can move straight (in one shot) to the Nash equilibrium. The process is independent of the initial condition and does not relate to any dynamic adjustment of power market.

However, in the actual power market, the market participants are not fully rational and unable to know the competitors' production decision and profit functions. They are unable to reach the equilibrium condition at once. In fact, each participant is bounded rational and can only decide the production strategy according to his expected marginal profit at each period. For each market participant, the evaluation of his own marginal profit is more accurate than the prediction of the competitors' outputs [18,19]. Therefore, the market participants play a Cournot game with bounded rationality in a dynamic adjustment process described as follows.

In the market operation, a generation producer decides the optimal production strategy according to its own generation cost and market information in order to obtain maximum profit. The optimal decision problem can be mathematically written as

$$\max_{q_i} \pi_i = P_i q_i - C_i(q_i) \quad (1)$$

where $C_i(q_i)$ is the generation cost of generation company at node i ; P_i is the electricity price at node i , which is decided by the Independent System Operator (ISO). By applying the marginal profit function of a generation company, the optimal generation quantities can be obtained.

$$\frac{\partial \pi_i}{\partial q_i} = P_i + \frac{\partial P_i}{\partial q_i} \cdot q_i - \frac{\partial C_i(q_i)}{\partial q_i} = 0 \quad (2)$$

Due to the lack of global information of power market, each generation company adjusts its supply quantities for obtaining more benefit according to the local estimate of its own marginal profit. The mathematical model of the adjustment mechanism of the generation quantities, i.e., the dynamic Cournot game model with bounded rationality is

$$\begin{aligned} q_i(t+1) &= F_i(q_i(t)) = q_i(t) + \alpha_i(q_i(t)) \frac{\partial \pi_i}{\partial q_i(t)} \\ &= q_i(t) + \alpha_i(q_i(t)) \left[P_i + \frac{\partial P_i}{\partial q_i(t)} \cdot q_i(t) - \frac{\partial C_i(q_i(t))}{\partial q_i(t)} \right] \\ &\quad (i=1, \dots, N) \end{aligned} \quad (3)$$

where $q_i(t)$, $q_i(t+1)$ are the generation quantities of the generation company at node i at time t and $t+1$; $\alpha_i(q_i(t))$ is a positive function which gives the extent of the production variation of the i th generation company following a given profit signal. If $\alpha_i(q_i(t))$ is assumed to be a linear function, then $\alpha_i(q_i(t)) = \alpha_i q_i$ can be obtained, where the positive constant α_i is called the speed of adjustment.

From (3) it can be seen that in order to cause the generation company to obtain a more economical profit in the power market, if its marginal profit is greater than 0, the generation company will increase q_i in the next time; otherwise, the generation company will decrease q_i in the next time.

2.2 ISO Optimization Model

In the power market, the decision behaviors of market participants should be checked by the ISO to satisfy the inherent physical characteristics of power network and ensure the security of power system operation. In the centralized market clearing, on the premise that the supply quantities of the generation companies are known (which can be determined by the dynamic Cournot game model of the market participants in (3)), the ISO allocates the market demand to maximize the total market benefit with satisfying the power network constraints, such as the power balance constraint and the line flow constraints. The mathematical model based on the DC power flow can be expressed as follows:

$$\begin{aligned} \max \quad & e^T B(d) + B_N(d_N) \\ \text{s.t.} \quad & e^T d + d_N = e^T q + q_N \\ & H(q-d) \leq K \end{aligned} \quad (4)$$

where N is the total number of nodes (where node N is assumed to be the slack node), L is the total number of lines; $d, q \in R^{N-1}$ are the nodal demand and generation power vectors excluding the slack node N , d_N, q_N are the demand and generation power at the slack node N ; $H \in R^{L \times (N-1)}$ denotes the transfer admittance matrix that

represents the sensitivity of the nodal power injection to line power flow; $e \in R^{N-1}$ is a vector of all ones; $K \in R^L$ is the vector of maximum power flow on the transmission line; $B(d) \in R^{N-1}$ is the vector of the nodal benefit of consumer excluding the slack node N , $B_N(d_N)$ is the benefit of consumer at the slack node N , and assumed as

$$B(d_i) = a_i d_i - 0.5 b_i d_i^2 \quad (i=1, \dots, N) \quad (5)$$

where a_i, b_i are the linear and quadratic coefficients of the consumer benefit function.

The Lagrange function for the optimization problem in (4) can be set up (in the constraints of line power flow, only the equality constraints are taken into account):

$$\begin{aligned} L &= e^T B(d) + B_N(d_N) - \lambda (e^T d + d_N - e^T q - q_N) \\ &\quad - \mu^T (\ddot{H}(q-d) - \ddot{K}) \end{aligned} \quad (6)$$

where λ, μ are the Lagrange multipliers for the power balance constraint and the line flow constraints; \ddot{H}, \ddot{K} are the matrices H, K excluding the terms corresponding to the non-congestion lines.

By $\partial L / \partial d = 0, \partial L / \partial d_N = 0$, the function relationship between the electricity price and the generation quantities can be obtained as follows:

1) When the congestion occurs in the power network,

$$\begin{aligned} P_N &= \frac{\partial B_N(d_N)}{\partial d_N} = \lambda = a - b(q_N + e^T \ddot{H}^{-1} \ddot{K}) \\ P &= \frac{\partial B(d)}{\partial d} = \lambda e - \ddot{H}^T \mu = a e - b(q - \ddot{H}^{-1} \ddot{K}) \end{aligned} \quad (7)$$

2) When the congestion does not occur in the power network,

$$\begin{aligned} P_N &= \lambda = a - \frac{b}{N} (e^T q + q_N) \\ P &= \lambda e = a e - \frac{b}{N} (e^T q + q_N) e \end{aligned} \quad (8)$$

where $P \in R^{N-1}$ is the nodal price vector excluding the slack node N , P_N is the nodal price at the slack node N .

From (7) and (8), it can be concluded that when there is no congestion in the power network, all nodal prices are identical; while during congestion, the nodal prices are different and related to the congestion conditions of power network. With the change of congested lines, the matrices \ddot{H}, \ddot{K} is varied, and then the function relationship between the nodal price and generation quantities is changed.

A further analysis is performed with an example of simple power market as shown in Figure 1. There are two zonal markets connected by a transmission line with capacity k . The electricity prices of the two zonal markets are P_1, P_2 , with the demand quantities being d_1, d_2 and the generation quantities as q_1, q_2 .

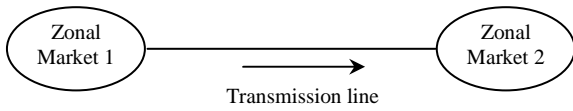


Figure 1. Structure of power market

For simplicity, the benefit of consumers is identical in these two zonal markets. In the calculation, suppose node 2 is the slack node, the positive direction of line power flow denoted by the arrow in Figure 1.

By establishing the optimization model in (6), the function relation between the zonal prices and the generation quantities are deduced from (7) and (8). When the transmission line is not congested, the zonal prices are

$$P_1 = P_2 = a - \frac{b}{2}(q_1 + q_2) \quad (9)$$

In this case, the power flow on the transmission line satisfies:

$$-k \leq q_1 - d_1 = \frac{(q_1 - q_2)}{2} \leq k$$

i.e., $-2k \leq q_1 - q_2 \leq 2k$.

When the transmission line is congested and its power flow is k , the zonal prices are

$$P_1 = a - b(q_1 - k), P_2 = a - b(q_2 + k) \quad (10)$$

Similarly, when the line power flow is $-k$, the zonal prices are

$$P_1 = a - b(q_1 + k), P_2 = a - b(q_2 - k) \quad (11)$$

Therefore, under the consideration of power network constraints, the price function of power market exhibits the following piecewise form:

$$P_1 = \begin{cases} a - b(q_1 + k) & q_1 - q_2 < -2k \\ a - \frac{b}{2}(q_1 + q_2) & -2k \leq q_1 - q_2 \leq 2k \\ a - b(q_1 - k) & q_1 - q_2 > 2k \end{cases} \quad (12)$$

$$P_2 = \begin{cases} a - b(q_2 - k) & q_1 - q_2 < -2k \\ a - \frac{b}{2}(q_1 + q_2) & -2k \leq q_1 - q_2 \leq 2k \\ a - b(q_2 + k) & q_1 - q_2 > 2k \end{cases} \quad (13)$$

Figure 2 shows the piecewise continuous curve of electricity price function in the zonal market 1.

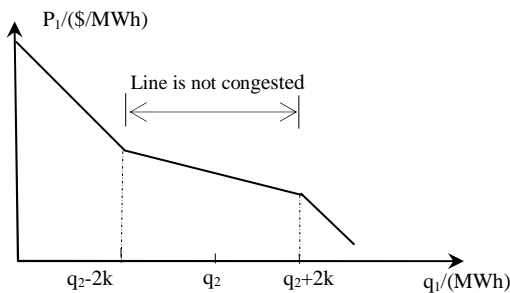


Figure 2. Curve of electricity price of zonal market 1

2.3 Dynamic Model of Power Market

The dynamic model of power market is an integration of the dynamic Cournot game model with bounded rationality, i.e., the discrete difference equations in (3), and the maximization model of market benefit considering the power network constraints, i.e., the optimization model in (4). Therefore, the dynamic model of power market is represented by the discrete difference equations embedded with the optimization problem. Compared with the existing dynamic models, the remarkable characteristics of the proposed one are

1) The market participants need not have global market information, such as the market demand and the competitors' cost. They decide their generation quantities by estimating their own marginal profit. This decision process reflects the actual situation of the economic system to a certain extent, indicating some feasible and rational features.

2) If the dynamic system is finally able to converge to the equilibrium condition, i.e. $\partial \pi_i / \partial q_i(t) = 0$, each generation company reaches its own maximum profit and is unable to improve the profit only by changing its own generation strategies. In this situation, the market reaches the condition of Nash equilibrium.

3) $\partial \pi_i / \partial q_i(t)$ is the marginal profit function. From (3), it can be observed that if $\partial \pi_i / \partial q_i(t) > 0$, the generation company will increase q_i in the next time; otherwise, the generation company will decrease q_i .

4) The system of discrete difference equations embedded with the optimization problem considers the impact of the power network constraints on the behaviors of the market participants. It can indicate that the dynamic model of power market is more complex than that of general commodity market.

For a duopoly Cournot game as shown in Figure 1, the dynamic Cournot model of power market with bounded rationality considering the power network constraints is

$$\begin{cases} q_1(t+1) = q_1(t) + \alpha_1 q_1(t) [a - c_1 - bk - 2bq_1(t)] \\ q_2(t+1) = q_2(t) + \alpha_2 q_2(t) [a - c_2 + bk - 2bq_2(t)] \end{cases} \quad (14)$$

if $q_1(t) - q_2(t) < -2k$

$$\begin{cases} q_1(t+1) = q_1(t) + \alpha_1 q_1(t) [a - c_1 - bq_1(t) - 0.5bq_2(t)] \\ q_2(t+1) = q_2(t) + \alpha_2 q_2(t) [a - c_2 - 0.5bq_1(t) - bq_2(t)] \end{cases} \quad (15)$$

if $-2k \leq q_1(t) - q_2(t) \leq 2k$

$$\begin{cases} q_1(t+1) = q_1(t) + \alpha_1 q_1(t) [a - c_1 + bk - 2bq_1(t)] \\ q_2(t+1) = q_2(t) + \alpha_2 q_2(t) [a - c_2 - bk - 2bq_2(t)] \end{cases} \quad (16)$$

if $q_1(t) - q_2(t) > 2k$

3. Nash Equilibrium and Local Stability of Power Market

3.1 Nash Equilibrium of Power Market

Definition 1: A Nash equilibrium for (1) is a vector $q^* = (q_1^*, q_2^*, \dots, q_i^*, \dots, q_N^*)$ such that for each participant i , given all other participants' output q_{-i}^* , q_i^* maximizes the i th participant's profit, that is $q_i^* \in \arg \max \pi_i(q_i, q_{-i}^*)$.

In the dynamic model (3), if $q_i(t+1) = q_i(t)$, the market arrives at a fixed point. It is called the equilibrium point in economics, where the fixed point $q_i(t) = 0$ is the boundary equilibrium point. It is easy to verify that the nonzero fixed point is the Nash equilibrium point.

For the duopoly dynamic game in the simple power market as shown in Figure 1, represented by (14), (15), (16), the equilibrium points of the market are analyzed under the different operating conditions of power network, i.e., congestion or non-congestion. In the model, suppose the generation cost function is in linear form, i.e.,

$$C_1(q_1) = c_1 q_1, C_2(q_2) = c_2 q_2 \quad (17)$$

where c_1, c_2 are the marginal generation costs.

If $-2k \leq q_1 - q_2 \leq 2k$, the transmission line is not congested. By solving the fixed points in (15), we can have at most 4 equilibrium points:

$$q^0 = (0, 0), q^1 = \left(\frac{a-c_1}{b}, 0 \right), q^2 = \left(0, \frac{a-c_2}{b} \right),$$

$$q^* = \left(\frac{2(a+c_2-2c_1)}{3b}, \frac{2(a+c_1-2c_2)}{3b} \right)$$

where q^0, q^1, q^2 are the boundary equilibriums, and q^* is the Nash equilibrium. Due to the satisfaction of the conditions $-2k \leq q_1 - q_2 \leq 2k$, $q_1, q_2 \geq 0$, only the equilibrium points q^1, q^2 and q^* are effective if $0 < a-c_1 \leq 2bk$, $0 < a-c_2 \leq 2bk$, $a+c_2-2c_1 \geq 0$, $a+c_1-2c_2 \geq 0$, $-bk < c_1-c_2 \leq bk$.

If $q_1 - q_2 < -2k$ or $q_1 - q_2 > 2k$, the transmission line is congested. By solving the fixed points in (14), we can have at most 4 equilibrium points:

$$q^0 = (0, 0), q^1 = \left(\frac{a-c_1-bk}{2b}, 0 \right), q^2 = \left(0, \frac{a-c_2+bk}{2b} \right),$$

$$q^* = \left(\frac{a-c_1-bk}{2b}, \frac{a-c_2+bk}{2b} \right)$$

Due to the satisfaction of the conditions $q_1 - q_2 < -2k$, $q_1, q_2 \geq 0$, only the equilibrium points q^2 and q^* are effective if $a-c_1 > bk$, $c_1-c_2 > 2bk$. By solving the fixed points in (16), we can have at most 4 equilibrium points:

$$q^0 = (0, 0), q^1 = \left(\frac{a-c_1+bk}{2b}, 0 \right), q^2 = \left(0, \frac{a-c_2-bk}{2b} \right),$$

$$q^* = \left(\frac{a-c_1+bk}{2b}, \frac{a-c_2-bk}{2b} \right)$$

Due to the satisfaction of the conditions $q_1 - q_2 > 2k$, $q_1, q_2 \geq 0$, only the equilibrium points q^1 and q^* are effective if $a-c_2 > bk$, $c_2-c_1 > 2bk$.

From the above analysis, it is found that there are different Nash equilibriums in the power market under different operational conditions of power network, such as congestion and non-congestion, while in some cases there is no Nash equilibrium at all if the market parameters satisfy $bk < |c_1 - c_2| < 2bk$.

3.2 Local Stability of Nash Equilibrium

The local stability of equilibrium point is studied based on the complex plane of the eigenvalues of the Jacobian matrix of the mapping

$$q(t+1) = F(q(t))$$

Definition 2: For a dynamic system $x(t+1) = F(x(t))$.

($x \in R^N$), with a fixed point q , if all the eigenvalues of the Jacobian matrix $\nabla F(q)$ is less than 1 in modulus, there exists an open neighbourhood I of q . When $x \in I$, such that

$$\lim_{t \rightarrow \infty} x(t) = q$$

here, q is called the local stable fixed point [20].

If $-2k \leq q_1 - q_2 \leq 2k$, the transmission line is not congested, the Jacobian matrix $\nabla F(q)$ is denoted as

$$\nabla F(q) = \begin{bmatrix} 1 + \alpha_1(a-c_1-2bq_1-0.5bq_2) & -0.5bq_1 \\ -0.5bq_2 & 1 + \alpha_2(a-c_2-0.5bq_1-2bq_2) \end{bmatrix}$$

when the market lies in the Nash equilibrium point

$$q^* = \left(\frac{2(a+c_2-2c_1)}{3b}, \frac{2(a+c_1-2c_2)}{3b} \right),$$

the eigenvalue equation of the Jacobian matrix $\nabla F(q^*)$ is:

$$\lambda^2 - (2 - \alpha_1 b q_1^* - \alpha_2 b q_2^*) \lambda$$

$$+ 1 - \alpha_1 b q_1^* - \alpha_2 b q_2^* + \frac{3}{4} \alpha_1 \alpha_2 b^2 q_1^* q_2^* = 0$$

The stability condition of Nash equilibrium point is $|\lambda_1| < 1, |\lambda_2| < 1$, and thus the market parameters should satisfy:

$$4\alpha_1 b q_1^* + 4\alpha_2 b q_2^* - 16 < 3\alpha_1 \alpha_2 b^2 q_1^* q_2^* - 4\alpha_1 b q_1^* - 4\alpha_2 b q_2^* < 0 \quad (18)$$

when the market equilibrium point is $q^1 = \left(\frac{a-c_1}{b}, 0 \right)$,

the two eigenvalues of the Jacobian matrix $\nabla F(q^1)$ are

$$\lambda_1 = 1 - \alpha_1(a-c_1) < 1$$

$$\lambda_2 = 1 + \frac{1}{2}\alpha_2(a + c_1 - 2c_2) > 1$$

Thus, the boundary equilibrium point q^1 is unstable. Similarly, it is easy to prove that the boundary equilibrium point q^2 is unstable too.

If $q_1 - q_2 < -2k$, the transmission line is congested, the Jacobian matrix $\nabla F(q)$ is denoted as

$$\nabla F(q) = \begin{bmatrix} 1 + \alpha_1(a - c_1 - bk - 4bq_1) & 0 \\ 0 & 1 + \alpha_2(a - c_2 + bk - 4bq_2) \end{bmatrix}$$

when the market lies in the Nash equilibrium point $q^* = \left(\frac{a - c_1 - bk}{2b}, \frac{a - c_2 + bk}{2b} \right)$, the stability condition of Nash equilibrium point is:

$$\alpha_1 b q_1^* < 1, \quad \alpha_2 b q_2^* < 1 \quad (19)$$

when the market equilibrium point is $q^2 = \left(0, \frac{a - c_2 + bk}{2b} \right)$, one of the eigenvalues of the Jacobian matrix $\Delta F(q^2)$ is greater than 1. Thus, the boundary equilibrium point q^2 is unstable.

If $q_1 - q_2 > 2k$, it is easy to prove similarly that the boundary equilibrium point q^1 is unstable, and while the Nash equilibrium point q^* is stable if $\alpha_1 b q_1^* < 1, \alpha_2 b q_2^* < 1$.

Therefore, in the dynamic Cournot game, whether the market can finally converge to a certain Nash equilibrium point is decided by the market parameters and the line flow limits, i.e.,

1) When the difference between the marginal cost of generation companies is less than bk , i.e., $-bk < c_1 - c_2 < bk$ (the other market parameters satisfy $a + c_2 - 2c_1 \geq 0, a + c_1 - 2c_2 \geq 0$) and the market parameters satisfy the condition in (18), the generation quantities of generation companies do not greatly differ in different zonal markets. Thus, the transmission line can not be congested. In this situation, if the generation quantities fall inside the stability region of Nash equilibrium, the market will be able to gradually converge to the Nash equilibrium point

$$q^* = \left(\frac{2(a + c_2 - 2c_1)}{3b}, \frac{2(a + c_1 - 2c_2)}{3b} \right) \quad (20)$$

2) When the difference between the marginal cost of generation companies is greater than $2bk$, i.e., $|c_1 - c_2| > 2bk$ (the other market parameters satisfy $a - c_1 > bk$ or $a - c_2 > bk$) and the market parameters satisfy the condition in (19), the generation quantities of generation companies greatly differ in different zonal markets. Thus, the transmission line is congested. In this situation, if the generation quantities fall inside the stability region of Nash

equilibrium, the market will be able to gradually converge to the Nash equilibrium point

$$q^* = \left(\frac{(a - c_1 - bk)}{2b}, \frac{(a - c_2 + bk)}{2b} \right)$$

or

$$q^* = \left(\frac{(a - c_1 + bk)}{2b}, \frac{(a - c_2 - bk)}{2b} \right) \quad (21)$$

3.3 Effect of Market Parameters on Stability

The equation in (18) gives the stability condition of Nash equilibrium if the line is not congested. Figure 3 shows the corresponding stability region of Nash equilibrium point in the plane of the adjustment speeds (α_1, α_2) , which is bounded by the portion of hyperbola, i.e.,

$$3\alpha_1\alpha_2b^2q_1^*q_2^* - 8\alpha_1bq_1^* - 8\alpha_2bq_2^* + 16 = 0$$

where:

$$A_1 = \left(\frac{3}{a + c_2 - 2c_1}, 0 \right), \quad A_2 = \left(0, \frac{3}{a + c_1 - 2c_2} \right) \quad (22)$$

For the values (α_1, α_2) inside the stability region, the Nash equilibrium is stable. From Figure 3, the increment of the adjustment speeds will reduce the stability margin when the other parameters are fixed. If the adjustment speeds go beyond the stability region, the Nash equilibrium point loses its stability through a period-doubling bifurcation.

If the parameter a , the maximum electricity price of electric power, is increased and the other parameters $\alpha_1, \alpha_2, c_1, c_2$ are fixed, the stability region becomes smaller, as can be easily deduced from (22). Otherwise, if the parameter a is reduced, the stability of Nash equilibrium can be reinforced.

If the other parameters are fixed, an increment of the marginal generation cost c_1 causes a displacement of the point A_1 to the right and of A_2 downwards. Instead, an increment of the marginal generation cost c_2 causes a displacement of the point A_1 to the left and of A_2 upwards. In both cases, the effect on the stability of Nash equilibrium point depends on the position of the point

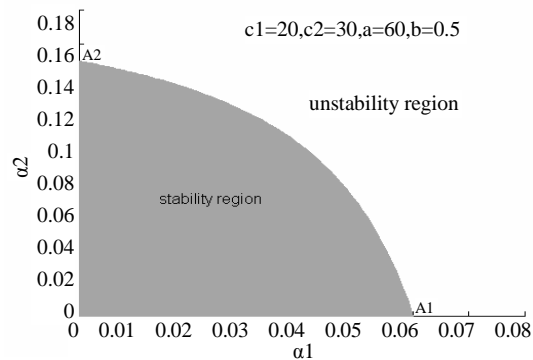


Figure 3. Stability region of Nash equilibrium under non-congestion

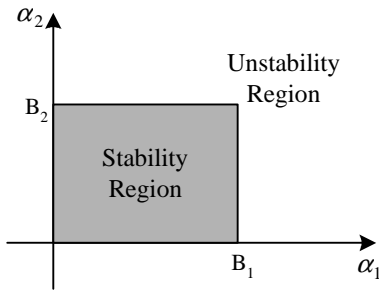


Figure 4. Stability region of Nash equilibrium under congestion

(α_1, α_2) . In fact, if the point (α_1, α_2) is above the diagonal $\alpha_1 = \alpha_2$, i.e., $\alpha_1 < \alpha_2$, an increment of c_1 can destabilize the Nash equilibrium point, whereas an increase of c_2 reinforces its stability. The situation is reversed if $\alpha_1 > \alpha_2$.

The equation in (19) gives the stability condition of Nash equilibrium if the line is congested. Figure 4 shows the corresponding stability region of Nash equilibrium point in the plane of the adjustment speeds (α_1, α_2) .

where:

$$B_1 = \left(\frac{2}{a - c_1 - bk}, 0 \right), B_2 = \left(0, \frac{2}{a - c_2 + bk} \right)$$

if $c_1 - c_2 > 2bk$

$$\text{or } B_1 = \left(\frac{2}{a - c_1 + bk}, 0 \right), B_2 = \left(0, \frac{2}{a - c_2 - bk} \right)$$

if $c_2 - c_1 > 2bk$ (23)

From Figure 4, the increment of the adjustment speeds (α_1, α_2) and the maximum price a can cause a loss of stability of Nash equilibrium, and while the increment of the marginal cost c_1 and c_2 can reinforce its stability.

Therefore, the power market can be kept in the stable equilibrium condition by the following measures in the actual operation.

1) The plentiful competition is introduced to reduce the difference between the generation marginal cost of generation companies in the power market; and the rational power network planning can improve the transfer capacity of lines, in order to keep the market in the stable equilibrium.

2) The variation extent of the generation quantities is not too large; and the smooth operation of the generator has important effect not only on the stability of power system but on the stability of power market.

3) The maximum price of market is not too high; and the restriction of the maximum value of electricity price can reinforce the stability of power market.

4. Numerical Simulation of Dynamic Market Behaviors

The dynamic behaviors of power market are demonstrated with an example of two-node power market as shown in Figure 1. The evolving characteristics of market behaviors are analyzed when the parameters lie in different ranges by using the bifurcation diagram, phase diagram, Lyapunov exponent and fractal dimension. In the iterative process of the numerical simulation, the benefit of consumers is identical and assumed with $a = 60\$/MWh$ and $b = 0.5\$/MWh^2$; the maximum production outputs of the two generation companies both are 200MWh; the flow limits of the line is 30MW.

4.1 Case 1: Difference between Marginal Cost of Generation Companies is Less than bk

Firstly, the dynamic behaviors of power market are numerically simulated when the difference between the marginal cost of the two generation companies is less than bk , i.e., $-bk < c_1 - c_2 < bk$. The generation marginal costs are taken as $c_1 = 20\$/MWh$, $c_2 = 30\$/MWh$. If different values are selected, similar results can be obtained. In this case, a Nash equilibrium point is obtained. By (20), the corresponding generation quantities of the two zones are (66.67MWh, 26.67MWh).

Let $\alpha_1 = 0.03MWh/\$$, the adjustment speed of the generation quantities of generation company 2 is changed. Figure 5 shows the bifurcation diagram of the stable solutions of the generation quantities and electricity price with α_2 . When the adjustment speed of generation company 1 is changed, similar results can be obtained.

If the adjustment speed of the generation quantities of generation company 2 satisfies $\alpha_2 < 0.12$, the market lie in the stability region of Nash equilibrium. The generation quantities will gradually converge to the unique stable solution, i.e., the Nash equilibrium point (66.67MWh, 26.67MWh). In this case, the power flow on the line is 20MW, that is, the line is not congested. Thus, the electricity price of the two zones is identical, both being 36.67\$/MWh. Figure 6 shows the evolving curve of the market converging to the Nash equilibrium if $\alpha_2 = 0.1$.

With the increment of the adjustment speed α_2 , when $\alpha_2 > 0.12$, the market will go beyond the stability region of Nash equilibrium and thus loses stability. If $0.12 < \alpha_2 < 0.175$, the dynamic evolution of the generation quantities and electricity price will converge to the two periodic points and the two-period variation is exhibited. Sequentially, with the increment of α_2 , the more complex dynamic behaviors are exhibited, such as four periods, eight periods, sixteen periods, etc. Figure 7 shows the periodic evolving curve of the market if $\alpha_2 = 0.16$.

With the continuous increment of the adjustment speed α_2 , when $\alpha_2 > 0.175$, the market converges to many

infinite points inside the bounded range and the seemingly random chaotic variation is exhibited. When α_2 is in the neighborhood of 0.18, the stable solutions of the market lie within a smaller range. In this case, the power flow on the line is less than 30MW, that is, the line is not

congested. Thus, the electricity price of zonal market 1 and 2 is identical. Figure 8 shows the chaotic evolving curve of the generation quantities and electricity price if $\alpha_2=0.18$; and the corresponding chaotic attractors as shown in Figure 9.

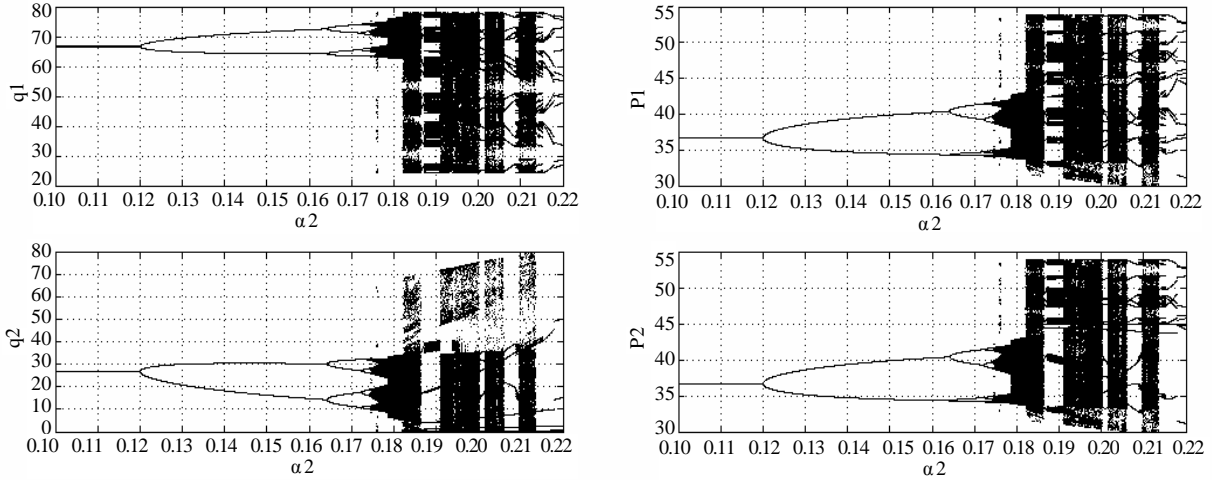


Figure 5. Bifurcation diagram of stable solutions of power market with α_2 if difference between marginal cost of generation companies is less than bk

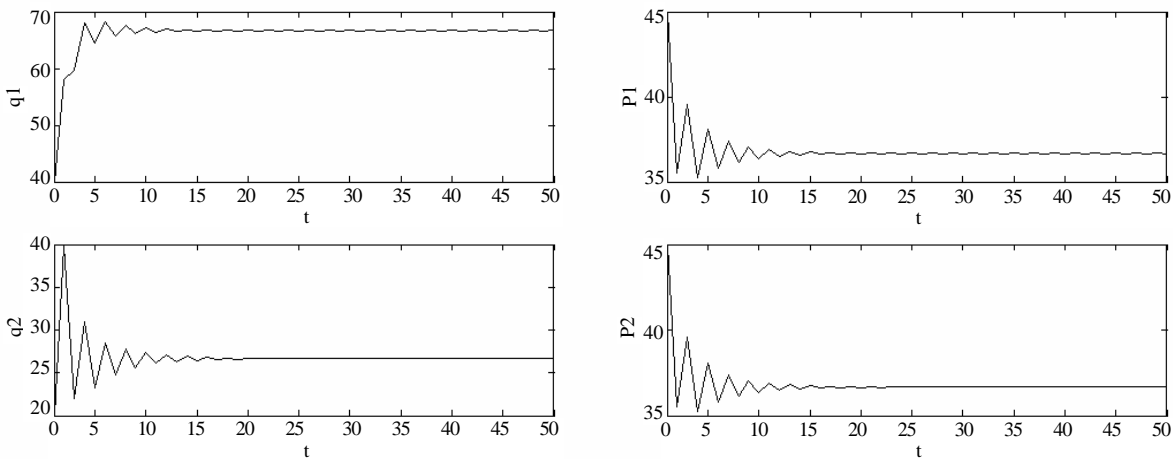


Figure 6. Dynamic market behaviors converging to Nash equilibrium if $\alpha_2=0.1$

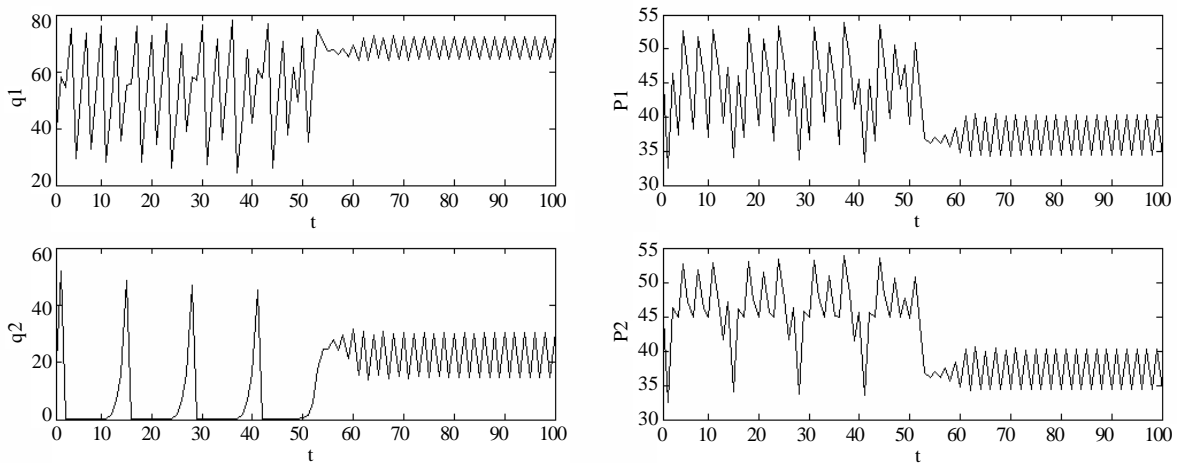


Figure 7. Periodic dynamic market behaviors if $\alpha_2=0.16$

However, when the adjustment speed α_2 lies in the other chaos area, the stable solutions of the market fall within a greater range. In this case, it is found that the line sometimes is congested to cause different electricity price in the zonal market 1 and 2; the chaotic attractors of market include not only the invariable manifold under

non-congestion condition (as shown in Figure 9), but the invariable manifold under congestion condition. Figure 10 shows the chaotic attractors of the generation quantities and electricity price if $\alpha_2=0.202$, their maximum Lyapunov exponents and fractal dimensions being 0.34 and 1.10, respectively.

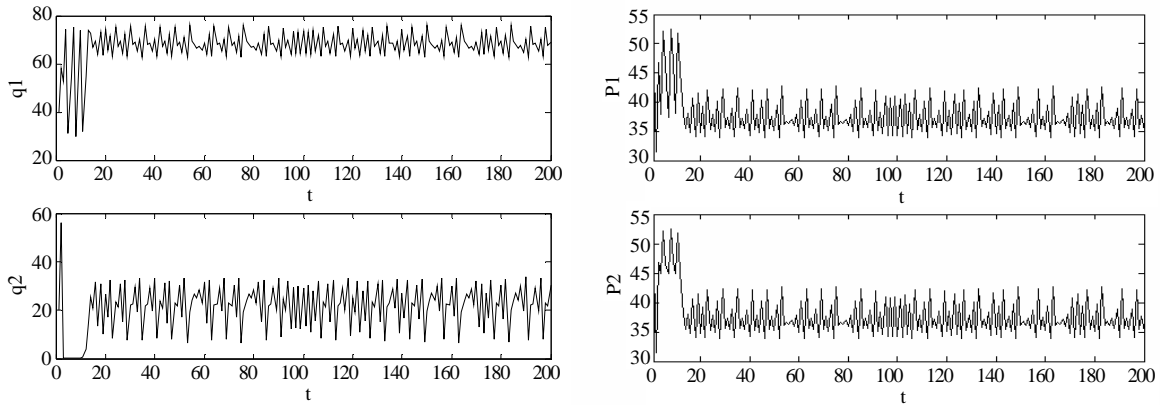


Figure 8. Chaotic dynamic market behaviors if $\alpha_2=0.18$

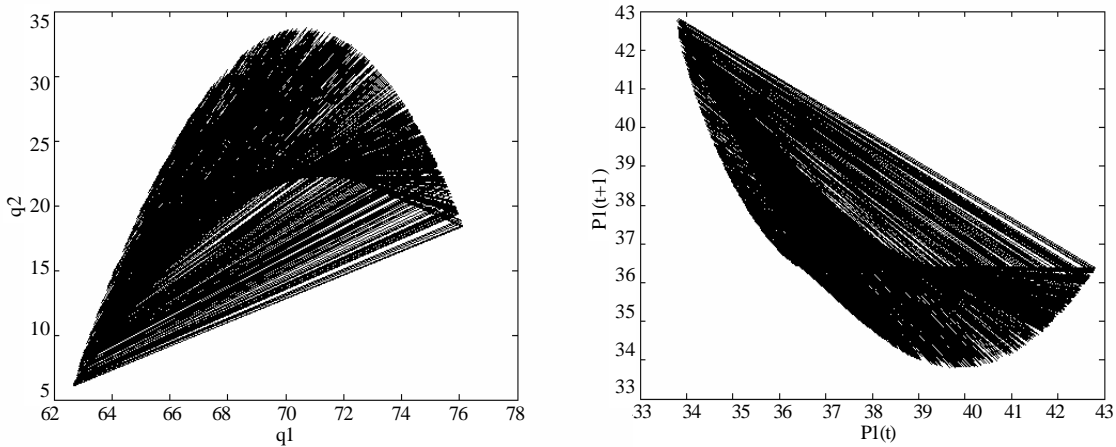


Figure 9. Chaotic attractors of generation quantities and electricity price if $\alpha_2=0.18$

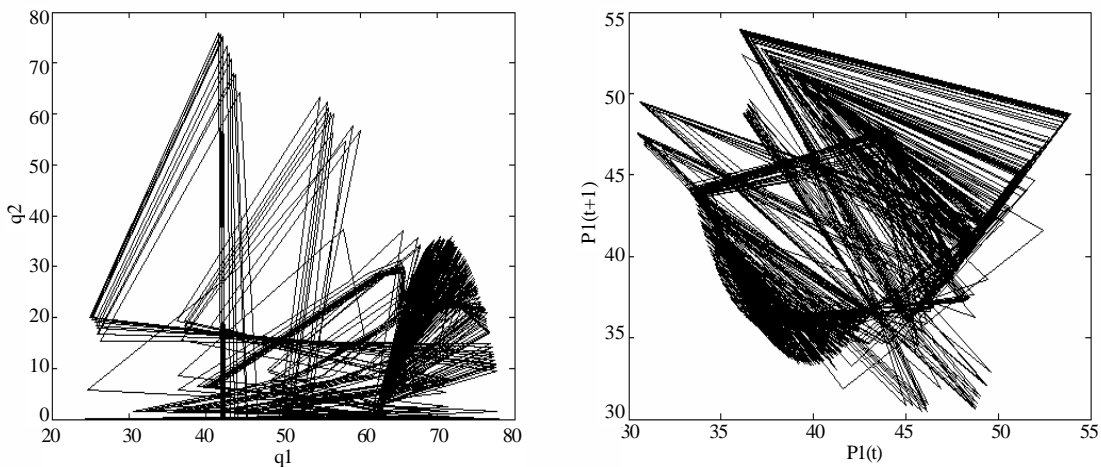


Figure 10. Chaotic attractors of generation quantities and electricity price if $\alpha_2=0.22$

4.2 Case 2: Difference between Marginal Cost of Generation Companies is Greater than $2bk$

The dynamic behaviors of the power market are numerically simulated when the difference between the marginal cost of the generation companies is greater than $2bk$, i.e., $|c_1 - c_2| > 2bk$. The generation marginal costs are taken as $c_1=40\$/MWh$, $c_2=5\$/MWh$. If different values are selected, similar results can be obtained. In this case, a Nash equilibrium point is obtained. By (21), the corresponding generation quantities of the two zones are (5MWh, 70MWh).

Let $\alpha_1 = 0.1MWh/\$$, the adjustment speed of the generation quantities of generation company 2 is changed. Figure 11 shows the bifurcation diagram of the stable solutions of the generation quantities and electricity price with α_2 . When the adjustment speed of generation company 1 is changed, similar results can be obtained.

If the adjustment speed of the generation quantities of generation company 2 satisfies $\alpha_2 < 0.028$, the market lie in the stability region of Nash equilibrium. The generation quantities will gradually converge to the unique stable solution, i.e., the Nash equilibrium point (5MWh, 70MWh). In this case, the power flow on the line is 30MW, that is, the line is congested. Thus, the electricity price of the two zonal markets is not identical, being 42.5\$/MWh and 40\$/MWh, respectively.

With the increment of the adjustment speed α_2 , when $\alpha_2 > 0.028$, the market will go beyond the stability region of Nash equilibrium and thus loses stability. The dynamic market behaviors exhibit the periodic and chaotic variation. The constraint of transmission line change the route of period-doubling bifurcation to chaos, exhibiting intermittency. Figure 12 shows the chaotic evolving behaviors if $\alpha_2=0.03$. The corresponding chaotic attractors are shown in Figure 13, their maximum Lyapunov exponents and fractal dimensions being 0.53 and 0.60.

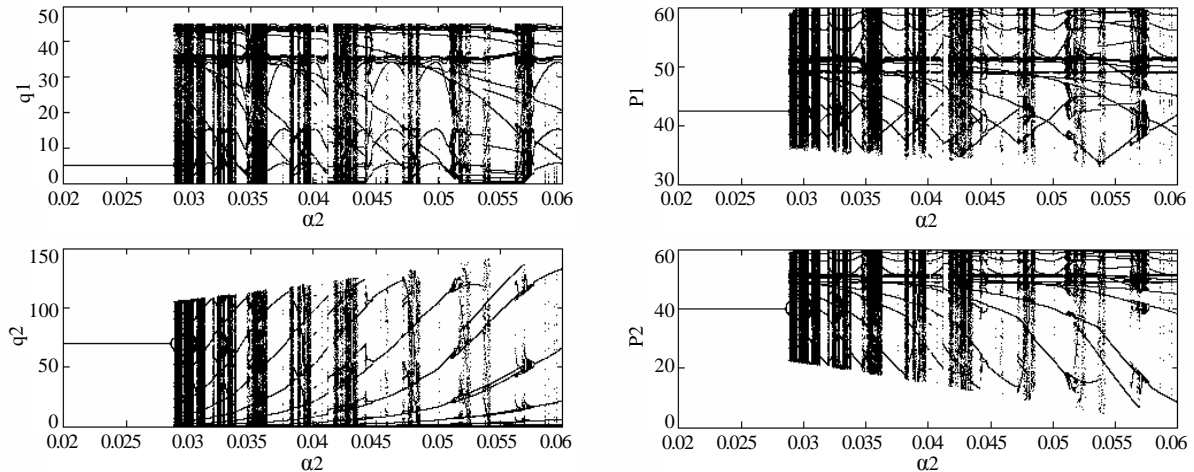


Figure 11. Bifurcation diagram of stable solutions of power market with $\alpha_2=0.22$ if difference between marginal cost of generation companies is greater than $2bk$

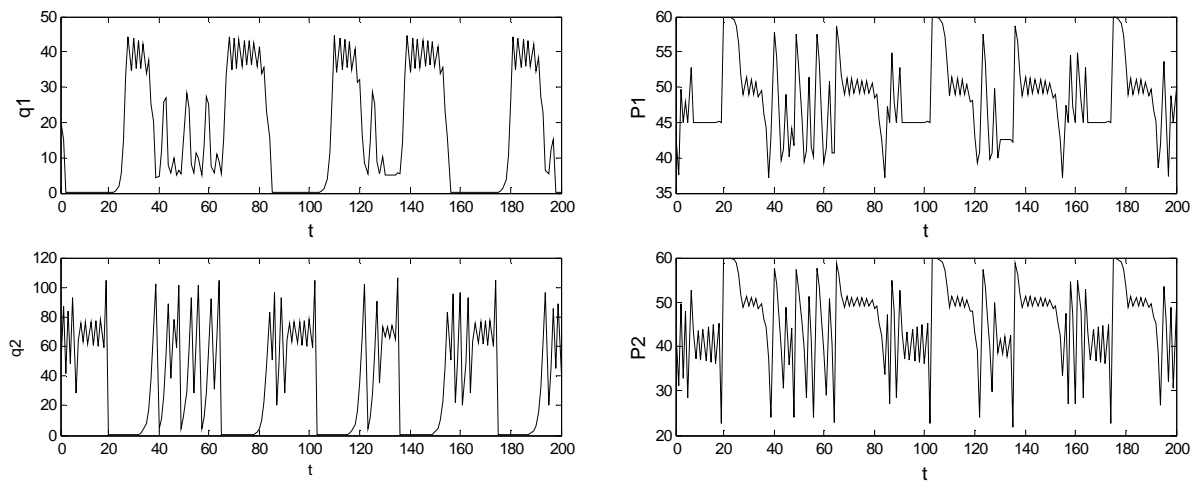


Figure 12. Chaotic dynamic market behaviors if $\alpha_2=0.03$

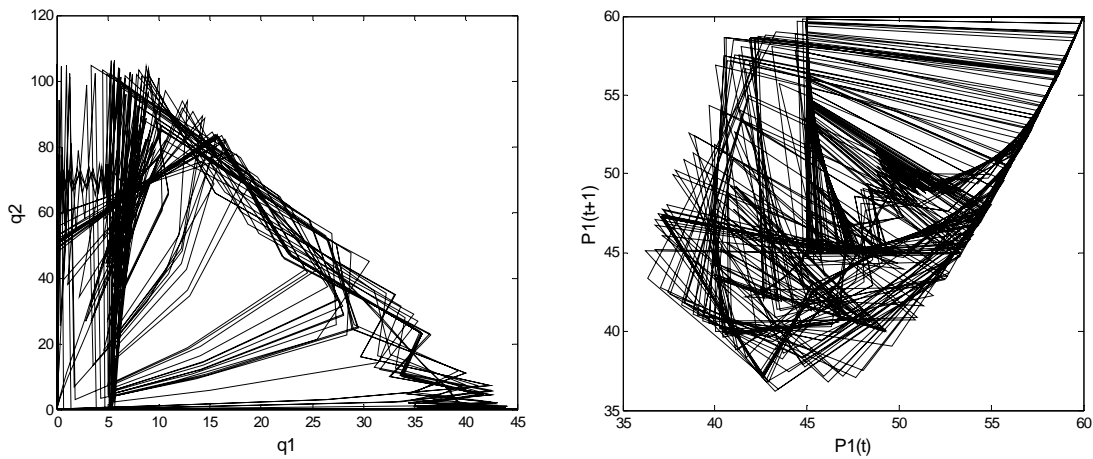


Figure 13. Chaotic attractors of generation quantities and electricity price if $\alpha_2=0.03$

4.3 Case 3: Difference between Marginal Cost of Generation Companies Lies in $[bk, 2bk]$

The dynamic behaviors of the power market are numerically simulated when the difference between the marginal cost of the generation companies lies in $[bk, 2bk]$, i.e., $bk < |c_1 - c_2| < 2bk$. The generation marginal costs are taken as $c_1=45\$/MWh$, $c_2=25\$/MWh$. Similar results can be obtained for other selected values. By the analysis of Section 3.1, there is no Nash equilibrium point in this case, that is, no matter how large the adjustment speeds are, the market cannot converge to a stable Nash equilibrium at all. Figure 14 shows the bifurcation diagram of the stable solutions of the generation quantities and electricity price with α_2 (where $\alpha_1 = 0.1MWh/\$$).

From Figure 14, it is found that the dynamic market behaviors exhibit the periodic and chaotic variation; and the chaotic and periodic windows appear in turn. Figure 15 shows the chaotic attractors of the generation quantities and electricity price if $\alpha_2=0.052$, their maximum Lyapunov exponents and fractal dimensions being 0.23

and 0.80, respectively.

Whether the transmission lines is congested or not, if the market participants with bounded rationality continuously adjust their production strategies, the market will finally converge to the Nash equilibrium under the satisfaction of its stability condition. Sequentially, a state that the market participants simultaneously maximize their respective profit is achieved.

In the complex dynamic power market, the equilibrium condition is short-term and temporary. In the equilibrium condition, many uncertain factors, such as the adjustment speeds and marginal cost of generation companies, the maximum electricity price of market, are changing the operating condition of market and pushing it towards chaos. The appearance of market chaos is very sensitive to the market parameters. The change of parameters can lead to a great difference between the long-term evolving trajectories of the dynamic market. Once the market enters the chaotic condition, it will be unpredictable, in which the generation companies are unable to effectively determine the adjustment of output quantities in the long term.

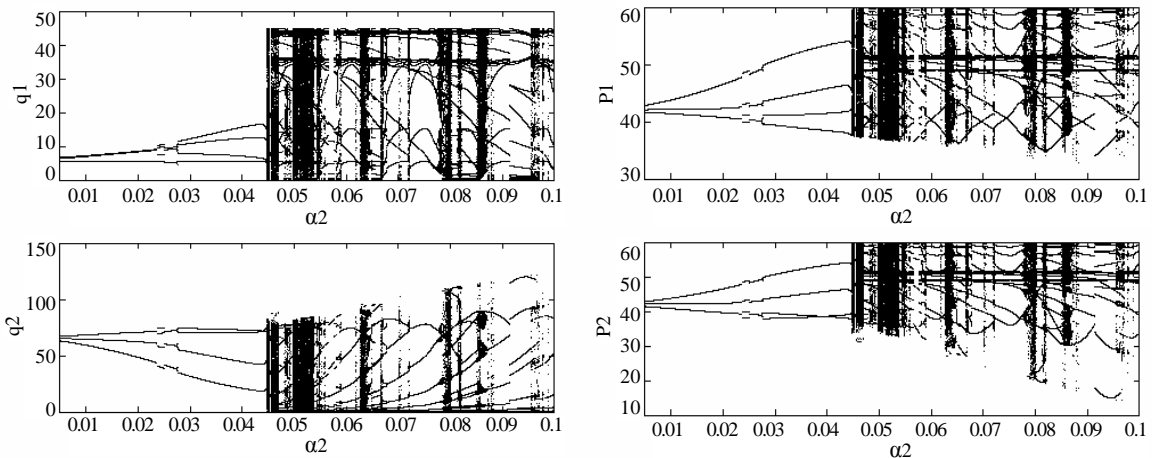


Figure 14. Bifurcation diagram of stable solutions of power market with α_2 if difference between marginal cost of generation companies lies in $[bk, 2bk]$

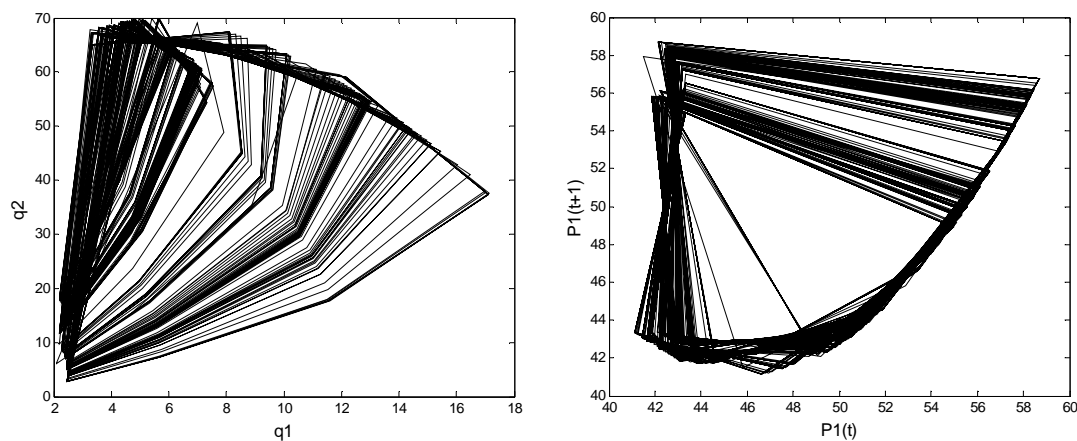


Figure 15. Chaotic attractors of generation quantities and electricity price if $\alpha_2=0.052$

However, when the market lies in the chaotic condition, it is still possible to effectively predict the short-term dynamics and change the chaotic market attractors to control the chaos. Therefore, in the case, the generation companies with bounded rationality should continuously survey their own surroundings and adjust their operation objectives. The market managers should timely modify the operation rules in order to change the chaotic market attractors and adapt the variation of the market environment.

5. Conclusions

This paper proposes the dynamic Cournot game model with bounded rationality considering the power network constraints, i.e., the difference equations embedded with the optimization problem. By using the theory of nonlinear discrete dynamic system, the Nash equilibrium and its stability for a duopoly market are quantitatively analyzed. It is found that the power market has different Nash equilibriums with different market parameters corresponding to different operating conditions, i.e., congestion and non-congestion, while in some cases it has no Nash equilibrium at all. The effect of market parameters is investigated on the stability of Nash equilibrium. It is also revealed that the smooth adjustment of the generation quantities and the restriction of the maximum value of electricity price can reinforce the stability of the power market. In the dynamic evolution, the market exhibits a variety of dynamic behaviors, i.e., converging to the Nash equilibrium, period and chaos.

Based on the above work, there are the following issues need to be explained and discussed.

(a) For descriptive simplicity, the generation marginal cost is assumed to be a linear form in this paper. If it is a quadratic function, the Nash equilibriums of market and their stability conditions may be similarly obtained, as well as the periodic and even chaotic dynamic behaviors when the market go beyond the stability region.

(b) In the dynamic Cournot game, the generation quantities are regarded as the decision variables of generation companies, which may be sold to the users through the

contract transaction, also to the Power Exchange through the Pool transaction. So long as the relationship between the demand and electricity price is identical in the two transaction models, the similar results, such as the same market equilibrium points and dynamic behaviors, can be obtained.

6. Acknowledgements

This work is supported by the National Natural Science Foundation of China (No.70601003) and the Program for New Century Excellent Talents in University of China.

REFERENCES

- [1] W. W. Hogan, "California market design breakthrough," Harvard University, Cambridge, 2002.
- [2] D. X. Zhang and Z. H. Chen, "Nonlinear dynamic economics-bifurcation and chaos," Ocean University Press of Qingdao, Qingdao, 1995.
- [3] H. N. Agiza, A. S. Hegazi, and A. A. Elsadany, "The dynamics of Bowley's model with bounded rationality," Chaos, Solitons and Fractals, 12, pp. 1705-1717, 2001.
- [4] N. A. Hamdy, I. B. Gian, and K. Michael, "Multistability in a dynamic Cournot game with three oligopolists," Mathematics and Computers in Simulation, 51, pp. 63-90, 1999.
- [5] R. Herdrik and S. Arco, "Control of the triple chaotic attractor in a Cournot triopoly model," Chaos, Solitons and Fractals, 29, pp. 409-413, 2004.
- [6] F. L. Alvarado, "The stability of power system markets," IEEE Transactions on Power Systems, 2, pp. 505-511, 1999.
- [7] F. L. Alvarado, J. Meng, and C. L. DeMarco, "Stability analysis of interconnected power systems coupled with market dynamics," IEEE Transactions on Power Systems, 4, pp. 605-701, 2001.
- [8] Z. H. Yang, Y. F. Liu, and Y. Tang, "Analysis of power market stability," Proceedings of the Chinese Society for Electrical Engineering, 2, pp. 1-5, 2005.
- [9] Y. D. Tang, J. J. Wu, and Y. Zou, "The research on the stability of power market," Automation of Electric Power Systems, 4, pp. 11-16, 2001.
- [10] A. Maiorano, Y. H. Song, M. Trovato, "Dynamics of non-collusive oligopolistic electricity markets," IEEE

- Power Engineering Society Winter Meeting, Vol. 2, pp. 838–844, 2000.
- [11] Y. B. Zhang, X. J. Luo, and J. Y. Xue, “Adaptive dynamic Cournot model of optimizing generating units’ power output under nonlinear market demand,” Proceedings of the Chinese Society for Electrical Engineering, 11, pp. 80–84, 2003.
- [12] Y. F. Liu, Y. X. Ni, and F. F. Wu, “Control theory application in power market stability analysis,” IEEE International Conference on Electric Utility Deregulation, Restructuring and Power Technologies, Vol. 2, pp. 562–569, 2004.
- [13] W. G. Yang and G. B. Sheble, “Modeling generation company decisions and electric market dynamics as discrete systems,” IEEE Power Engineering Society Summer Meeting, Vol. 3, pp. 1385–1391, 2002.
- [14] J. Gao and Z. H. Sheng, “Evolutionary game theory and its application in electricity market,” Automation of Electric Power Systems, 18, pp. 18–21, 2003.
- [15] S. Y. Xie, “Economic game theory,” 2th edition, Fudan University Press, Shanghai, 2002.
- [16] Z. Younes and M. Ilic, “Generation strategies for gaming transmission constraints: Will the deregulated electric power market be an oligopoly?” Proceedings of the 31th Hawaii International Conference on System Sciences, Vol. 3, pp. 112–121, 1998.
- [17] B. C. Lance, B. Ross, and L. B. Martin, “An empirical study of applied game theory: Transmission constrained Cournot behavior,” IEEE Transactions on Power Systems, 1, pp. 166–172, 2002.
- [18] G. I. Bischi and A. Naimzada, “Global analysis of a dynamic duopoly game with bounded rationality,” Advances in Dynamic Games and Application, Vol. 5, pp. 361–385, 1999.
- [19] H. R. Varian, “Microeconomic analysis,” 3rd edition. W. W. Norton & Company, 1992.
- [20] A. Medio and M. Lines, “Nonlinear dynamics: A primer,” Cambridge University Press, New York, 2001.

The Preliminary Design of IPv6 Home Gateway and Terminal*

Chengyi Wang¹, Ren Gao¹

¹School of Electronic Engineering, Hubei University of Economics, Wuhan, China.
Email: wcytjx@126.com; gaoren_928@yahoo.com.cn

Received January 8th, 2009; revised February 9th, 2009; accepted March 4th, 2009.

ABSTRACT

This paper briefly analyzes the advantages of IPv6 used at Intelligent home and describes an IPv6 home network frame. It also studies IPv6 transition technical problems facing home gateways and gives the summaries to the main protocol of each node of home network and their mutual relations. The key nodes of the home network based on IPv6, including the hardware design and software design of the home gateway and home network controller, are systematically designed in the paper. Finally, it illustrates the actual test environment and test in detail. The paper gives a view of the fact that the intelligent home appliances are becoming the current trend with the accelerating the transition of IPv4 to IPv6 and home network-wide implementation of IPv6 is about to become a reality, holding that the network controllers and home gateway based on ARM processor can support IPv6 and carry on the implementation of remote control and local control based on Web Browser.

Keywords: IPv6, Home Gateway, Home Network Terminal Controller, CGI

1. Introduction

With the rapid development and extensive application of micro-electronics, computers, networks, telecommunications and other technologies, various new consumer electronics products are rapidly entering the home. The intelligent home is becoming a trend of the times. One of the core technologies is the intelligent home network or home network. Through the network, a variety of information appliances, security alarm systems, medical monitoring systems and other home equipment will be connected and become an interactive information, centralized control and even remote control network.

2. IPv6 and Home Network

To build a home network, the most basic requirement is to achieve interconnection of different devices, and set up convenient ways of interaction. The interconnection's basic approach is to carry on the implementation of the connection based on TCP/IP protocol stack; To achieve interoperability, the most convenient and the simplest way is through the WEB browser; The most direct way for the equipment to achieve these functions is to contain embedded systems; To meet the needs of future home network quantity, size and security, the transition to IPv6 is becoming the current trend.

Compared to IPv4, IPv6 intelligent home has the following advantages.

- Extremely rich IP address: In theory, each square

meter of earth land surface may assign 10^{23} IP address averagely. This makes it possible that all networking equipment is assigned a public IP address. This is very important for China with the largest population [1].

- Improvement of Quality of Service: Through the support of the stream label, from the specific source to the specific destination transmission packet series, IPv6 data packets may carry on highly effective processing by the middle router. To watch video, such as to ensure the quality of programming, is an example.

- More security guarantee: With the supports of Authentication Header (AH) and Encapsulating Security Payload (ESP), the encryption of identify validation and payloads is implemented [2]. AH and ESP also support the encryption packets transmit on the Internet by the way of Tunneling technology. To easily realize remote control of home network information security is a good example.

- Strong ability of address automatic disposition: As the giant address resources, the IPv6 protocol's ability of address automatic disposition is more convenient than DHCP's. This also makes each kind of network home appliances and the intelligent network products of the user's home be connected more freely without complex disposition works than before. It is just "plug and play".

3. IPv6 Home Network Frame

3.1 IPv6 Home Network Frame

Home network mainly consists of the home gateway, PC, information appliance and intelligence control terminal

*Fund Project: Provincial Education Department of Hubei scientific research project (D200619006).

components [3]. With the exception of home gateway and PC, other equipment can be designed as controlled by the network terminal controller. The structure is illustrated in Figure 1. The general structure will meet the needs of home network interoperability and the easy operation, bearing the most basic IPv6 technical characteristics. The frame structure consists of outer network, gateway and various inner parts. All equipment shown in the Figure 1 can be controlled locally and centrally through the hand remote control device at home. It also can be controlled by the long-distance PC, which entered the home gateway machine through the Internet. The equipment is centrally controlled including local central control and long-distance central control by operator interface. Since all equipment has their own IP addresses based on the IPv6, they can be directly connected to external network without gateway. The dashed line means that it can be connected via gateway or without it directly, and the Internet should IPv6 or IPv4.

3.2 IPv6 Transition Technology

Network at home are more prone to form a pure IPv6 network. Home network often tends to connect to the Internet and the current Internet is based mainly on the IPv4 protocol stack, or IPv6 coexistence with IPv4 networks. Since the IETF released IPv6 protocol, it has been over ten years. The transition of the technology from IPv4 to IPv6 has experienced more than ten years, which is also expected to last a longer period of time. For the home network out-side, the link may be based on IPv4 port or IPv6 port. It is necessary for the home network gateway to support this transition. IPv6 transition technology has three main types: dual stack, tunnel, translate. Their typical applications are as in Table 1. Among them node A may be the home gateway. Node B may be the WAN-side node or remote PC. Middle may be the middle node or connected directly.

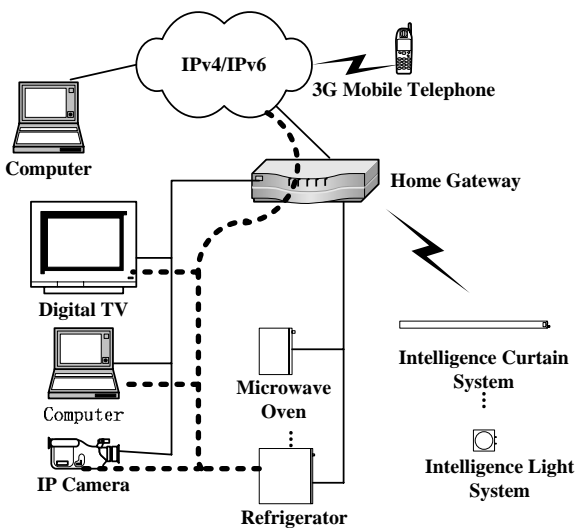


Figure 1. IPv6 home network architecture

Table 1. IPv6 transition technology and the applicable scene

Node A Protocol stack	Middle Protocol stack	Node B Protocol stack	Applicable technology
IPv6	none	IPv6	Connect directly
IPv6/IPv4	none	IPv6 or IPv4	dual stack
IPv6	IPv4	IPv6	tunnel
IPv6	none	IPv4	translate

3.3 The Protocol Stack at Home Network

At home network, the transmission of information is mainly related to the three adjacent nodes: home network terminal, home gateway and wan-side node. Relations with the protocol stack of information transmitted are as shown in Figure 2.

4. System Design

4.1 Hardware Design for Home Gateway

The design of home gateway in Figure 3 is based on network processor. The home gateway is conducted with the development board based on the network processor, such as Intel IXP425. It is equipped with a 10MB/100MB Ethernet port for external network, and provides eight 10MB/100MB Ethernet ports for internal network via a switching module. It also enables home wireless connection possible by the wireless local area network selected by the CF card plug [4].

4.2 The Hardware Design of Home Network Terminal

To support the IPv6 protocol stack and achieve remote control, the design of the terminal devices is formed with the network terminals and micro-controller, connecting the home gateway and appliance, shown in Figure 4. Network termination module can receive control information from the network through RS232 serial communication with the home appliance control module; appliance control module connected with appliances executing system can get control commands from the network termination module and operate home appliances. Among the above modules, the network terminal module is the core of information appliance system, which allows access to IPv6 network appliances, and serves as an embedded Web server to respond to the request of the client to complete the control data network.

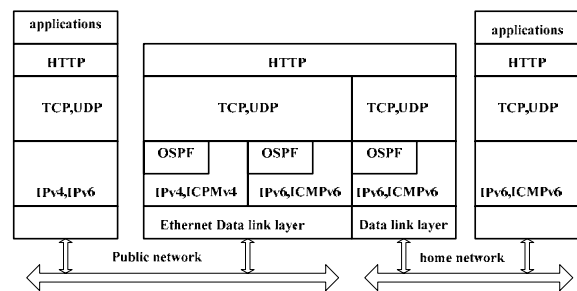


Figure 2. The protocol stack at home network

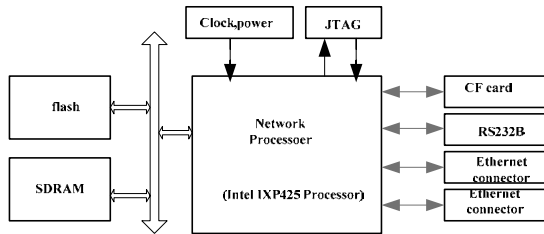


Figure 3. Hardware design for home gateway

The design in this article mainly consists of the network terminal microprocessor module, memory module, serial module, Ethernet module, power management and reset circuit modules, and JTAG module composed of several parts. Among them, the microprocessor modules are using S3C2410 of Samsung ARM9 core microprocessor. Ethernet module is constructed with the dual-NIC by two AX88796 cards.

4.3 The Design of Software System

4.3.1 The Frame of Software System

The design of the home gateway has three main functions: 1) IPv6/IPv4 route; 2) data-link layer switch; 3) Web server. Its software system structure is as shown in Figure 5, the relevant protocol stack shown in Figure 2.

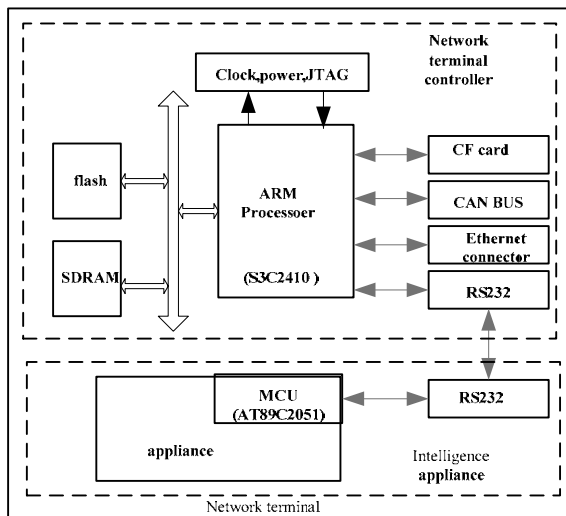


Figure 4. The hardware design of home network terminal

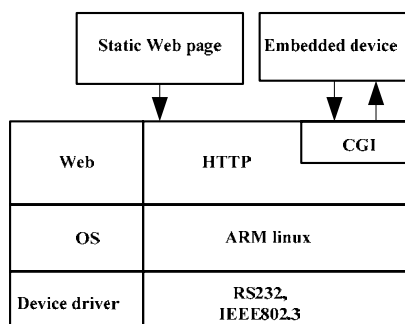


Figure 5. The frame of software system

The above-mentioned home gateways and network terminals are based on the 32bit embedded system. The main difference is the different hardware performance, which is reflected in the gateway hardware based on the network processor by a number of network processing engines to work together. The software system structure of Network terminal has the most similarities to home gateway. The main differences are: 1) network terminal without IPv6/IPv4 route just supports the data-link layer switch and Web server; 2) the boot loader of network terminal is vivi not redboot. Considering the needs of the following experiments, the following article focuses on network terminal software system structure and gives a further description below.

Network terminal software can be divided into three levels [5]: 1) hardware driver layer, including the generic hardware drivers, such as serial, USB devices, Ethernet, etc.; 2) embedded OS, including file system management, memory management, disruption and interruption of treatment, the system initialization, network protocol stack, various system calls, etc.; 3) application layer, through the kernel system call to implement the users needs of the required application services.

4.3.2 Embedded Linux

The main task is to transplant. Embedded Linux operating system transplant includes Boot Loader, the kernel and root file system. Boot Loader is the guiding procedure of embedded systems. VIVI as Boot Loader is developed by Korea Mizi system, which fits in the ARM920T and supports S3C2410 processor. Boot Loader is the first implementation code after power-on reset and is closely related to hardware. It first initializes the system hardware, sets the stack pointer, jumps to the entrance of the operating system kernel, and then gives the system control to the operating system. The kernel is the core of Linux operating system, which is the system software of managing hardware resources, controlling the running program and improving human-machine interface and application software to provide support. It achieves embedded systems management through the processor, memory management, file management, device management. The root file system is an important component of the Linux system, including system software and libraries, as well as the application software used to provide users with structure and application, and as the read/write results region of data storage.

4.3.3 CGI

According to the demands of embedded Web server application environments, network terminals and home gateways are required to provide web-based interoperability to update web page, deal with dynamic data, which can make use of Common Gateway Interface (CGI) to support. CGI is a software module of the embedded Web server for the implementation of server-side "script" program [6]. Furthermore, it uses "script" the implementation of the procedures, but also provides a channel to

handle the operation of the hardware. This constitutes a long-distance intelligent home control system's overall structure.

In the most Embedded Web applications, dynamic content show or interactive operation is required to be provided in order to remote control devices. The content provided by the simple static page is the same and is hard to be completed interoperability. Common Gateway Interface (CGI) can fundamentally solve the problem of this situation so that the WEB clients and servers have the interactive features, having remote control of embedded systems achieved. Typically, after the server responds to client requests, it will implement the corresponding CGI program and put the results of the implementation back to the client in order to achieve a dynamic Web. Web page code prepared by the ACTION attribute to specify the server required the implementation of the CGI program. METHOD property is specified in the client to submit data (POST or GET). CGI program is divided into the following sections: ① According to POST method or GET method, to receive data from the submitted forms; ② to decode URL encoding; ③ to use printf () function to generate the HTML source code and give the correctly decoded data back to the browser.

5. The Experimental Environment and Testing

5.1 The Basic Experimental Environment

The basic experimental environment to implement the systematic structure is as Figure 6. We can see from the diagram, the actual experimental environment has been simplified in order to simplify the problem, reduce costs, and realize the principle of a system. The specific simplifying job includes:

- PC2 replaces network processor: that is, the computer with dual network adapters is in place of NP. The network processor is very powerful, capable of performing the work of home gateway. It can mainly handle the analysis from the data-link layer to application layer, layer 2 switch, IPv4/IPv6 route. In this design, the focus is on implementation of the remote control of home terminals through the home gateway. Home gateway software and the transplanting process, Web server of the development process and function similar. The function of gateway is placed by PC software.
- PC1 replaces internet: pc1 is a stand-alone computers, which can be used conveniently as IPv4 node or IPv6 node. It can remote control home gateway and home network terminal by modeling.
- Using two network terminals separately replace two different types of equipment: Network terminal 1 is used to express different information appliance, such as refrigerators; Network terminal 2 is used to express two different intelligence control terminal, such as curtains.

5.2 Test

The whole experimental environment includes two networks, known as the home network and the outside network. Home network consists of PC2, network controller1

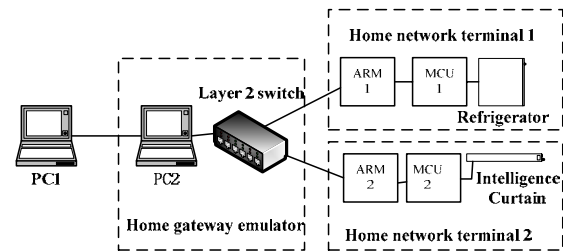


Figure 6. Basic test environment

and network controller 2. Each network controller is formed with a S3C2410 board and MCS-51 Single-chip Computer board (MCU board), each MCU board separately represents intelligence appliance. Different combinations of lights with different colors present their different control status and the actual device can be controlled. PC1 is installed with Windows XP as a client terminal. PC2 is installed with Windows Server 2003 and dual NIC, configured as a router. It is used for each access network appliance automatically assigned 64 of the IPv6 routing prefix 3FFE: FFFF: 2005:/64. Two PC machines are configured with IPv6 protocol and the installation of the browser Firefox. The kernel of embedded system is linux 2.6.8. Web software is mini_httpd, which can support IPv6 users visit, and the space needed for the compiled code is small. In order to configure and test IPv6 network environment, the supporting IPv6 configuration tools are required, such as ifconfig, ping, and traceroute and so on. Existing network configuration tools in linux do not support the IPv6 protocol. Therefore, it needs to re-compile source packages containing these instrument procedures to ensure its support for IPv6. This paper chooses the busybox 1.1.2, because it contains the majority of support for IPv6 network configuration tool, but the volume was small.

The network terminals of various home appliances are equipped with 64-bit IPv6 interface identifier derived from its MAC address. Take network controller 1 as an example, its MAC address being 00-E0-4C-4A-35-25, in accordance with IEEE EUI-64 format [7], the IPv6 interface identifier will be the 2E0:4Cff:fe4A:3525. When the appliance joins the test, it will automatically get the routing prefix of 64-bit of IPv6 distributed by PC2. Together with the existing 64-bit interface identifier for each household appliance, it can form the world's sole 128 IPv6 address.

When testing, to give the appliance's IPv6 address in the PC1 browser, can enter the corresponding appliance control interface. The user can operate on household electrical appliances by clicking the button. After the implementation of the user command, household electrical appliances will implement the results back to the browser. To cite the network controller 1 as an example, after entering in the browser the IPv6 address refrigerator [http://\[3FFE:FFFF:2005:0:2E0:4Cff:fe4A:3525\]](http://[3FFE:FFFF:2005:0:2E0:4Cff:fe4A:3525]) to get its user interface, the user can control home appliances by clicking the corresponding button.

6. Conclusions

Intelligent home appliances are becoming the trend of the times, while the IPv4 to IPv6 transition is accelerating. We can notice that a new generation of backbone network based on the IPv6 in China has been built. The new network routing equipment can support IPv6. Home network with implementation of the pure IPv6 will become a reality. Network controllers and home gateway (including IXP425 ARM Platform) based on ARM processor is able to support IPv6. In addition the implementation of the remote control and local control based on Web Browser can be achieved.

REFERENCES

- [1] D. R. Hinden, "Internet protocol version 6 (IPv6) specification," RFC 2460 standards Track, December 1998.
- [2] S. Hagen, "IPv6 essentials," Ji Qiao Translation, Tsinghua University Press, Beijing, 2004.
- [3] J. Yu, Z. Huang, and W. J. Tang, "Research and application of home network based on IPv6," Journal of Shenyang Normal University (Natural Science), Shenyang, No. 1, pp. 75–78, 2008.
- [4] W. H. Nie, Z. Q. Wang, and S. D. Du, "The construction of web server based on IXP425 and Linux," Microcomputer Applications, Beijing, No. 9, pp. 549–553, 2004.
- [5] T. Satio, I. Tomoda, and Y. Takabatake, "Home gateway architecture and its implementation," IEEE Transactions on Consumer Electronics, Vol. 46, No. 4, pp. 1161–1166, 2000.
- [6] C. G. Yao, J. D. Wang and Y. X. Peng, "Design of home gateway based on IPv6," Computer Technology and Development, Xi'an, No. 3, pp. 207–213, 2007.
- [7] M. C. Fermilab, "Transmission of IPv6 packets over Ethernet," RFC 2464 standards Track, December 1998.

Analysis and Design of a Kind of Improved Parallel Resonant Converters

Chenhu Yuan^{1,2}, Jianru Wan², Xiuyan Li², Hong Shen², Yingpei Liu², Guangye Li²

¹School of Information and Communication of Tianjin Polytechnic University, Tianjin, China, ²School of Electrical Engineering and Automation of Tianjin University, Tianjin, China.
Email: Yuanfei791019@163.com

Received January 6th, 2009; revised February 3rd, 2009; accepted February 18th, 2009.

ABSTRACT

Traditional transformer in high-voltage power supplies has many disadvantages such as high turn's ratio, large volume and great design difficulties. Parallel resonant converters (PRCs) are widely used in high-voltage power supplies. A kind of high-voltage circuit topology can be formed by combining PRCs and voltage-doubler rectifier, which is called parallel resonant dual voltage converters (PRDVCs). In PRDVCs both voltage-doubler rectifier and transformer can boost voltage, which reduced turn's ratio and volume of the transformer, making it easier to produce. Thus it not only realizes the high-voltage output, but also realizes the miniaturization of high-voltage power supply. Three modes of the converters were researched and simulated. Converting conditions of three modes were given. At last, PRDVCs was used to design a 5000V/50mA high-voltage power supply. The waveforms and results of the experiment were given, which validated the feasibility of the converters and its conversion efficiency might be improved to 93%.

Keywords: Power Converters, Parallel Resonant, Voltage-Doubler Rectifier, High-Voltage Power Supply

1. Introduction

High-voltage power supplies have been widely used in inspection equipments such as medicine, non-destructive testing, station, customs inspection and also been used for military purposes such as radar transmitters, electronic chart monitor in aviation light. Traditional high-voltage power supplies have affected development of corollary equipments because of large volume and heavy weight. At present, SMPS schemes have been widely adopted in high-voltage power supplies. It made the volume and weight be greatly reduced and power capacity and conversion efficiency be increased, especially embodied in small power high-voltage SMPS. Yet for all that, turn's ratio and volume of transformer were still very large and its difficulties in design and manufacture were still existent. For this reason, using the good adaptability of PRCs to high-voltage power supplies, A kind of high-voltage circuit topology can be formed by combining PRCs and oltage-doubler rectifier, which is parallel resonant dual voltage converters (PRDVCs) [1]. As a kind of improved parallel resonant high-voltage SMPS topology, PRDVCs can increase switch frequency and conversion efficiency by using soft switching technology. Both voltage-doubler rectifier and transformer can boost voltage, which made turn's ratio and volume of the transformer be greatly reduced, making it easier to produce. Thus it realized the miniaturization and lightweight of high-voltage power supply. In Section 2, the basic circuit topology of PRDVCs was introduced. In Section 3, work modals of PRDVCs were analyzed. In Section 4, three Modes were

studied. In Section 5, converting conditions of three modes were deduced. In Section 6, three Modes were verified by PSPICE. In Section 7, a 5000V/50mA high-voltage power supply was designed by using PRDVCs.

2. Basic Circuit Topology of PRDVCs

PRDVCs was the improvement of PRCs (as shown in Figure 1). Two kinds of basic topologies of PRDVCs were given in Figure 2. One was the half-bridge parallel resonant dual voltage converter (HBPRDVC) and the other was full-bridge parallel resonant dual voltage converter (FBPRDVC), where L_r was the resonant inductance, C_r was the resonant capacitance, R_L was load. Here the role of transformer was not only voltage transfer but also electrical isolation. Compared with PRCs, two capacitances were adopted to replace two rectifying diodes and the heavy inductance was omitted in PRDVCs circuit topology.

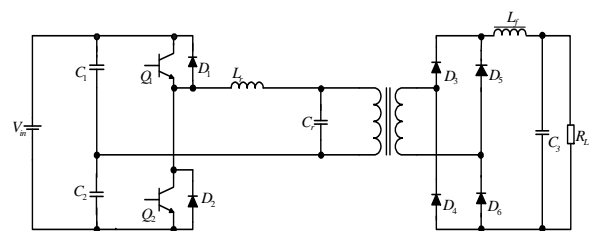


Figure 1. PRCs

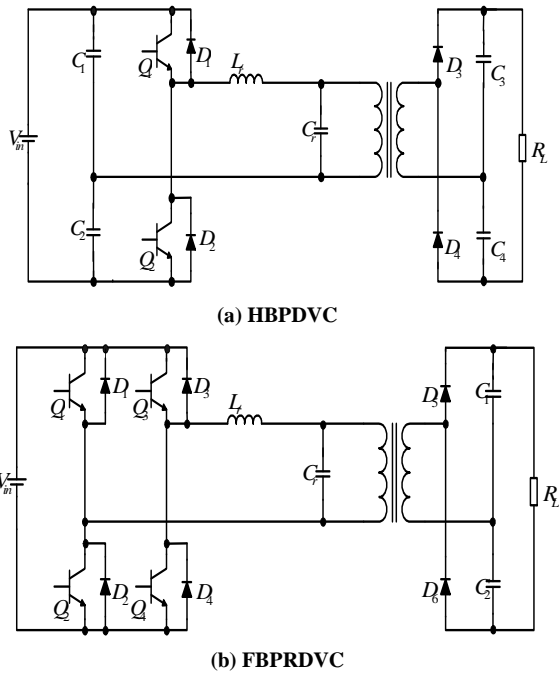


Figure 2. Basic circuit topologies of PRDVCs

3. Analysis for Work Modals of PRDVCs

Full bridge topology and half bridge topology work on the same principle [2]. In this paper, we took HBDPVC for example to research PRDVCs. For convenience transformer's ratio was declared equivalent to 1. Transformer was equivalent to excitation inductance and its leakage inductance was neglected. Then the equivalent circuit could be seen in Figure 3. Here the direction of voltage and current was reference direction. Before analyzing PRDVCs, some reasonable conditions should be assumed as follows. 1) $Q_1, Q_2, D_1, D_2, D_3, D_4$ were ideal switching tubes. 2) During a switching cycle both input voltage and output voltage were constants. C_1, C_2, C_3, C_4 were large enough. Electric potential of node A was $V_{in}/2$ and electric potential of node O was $V_o/2$. 3) Both inductance and capacitance were lossless energy storage elements. 4) line impedance was not considerable.

Under above conditions, PRDVCs had four resonant switching modals (as shown in Figure 4) and four linear switching modals (as shown in Figure 5). Where L_r was the resonant inductance, C_r was the resonant capacitance, L_m was the excitation inductance. The directions of arrows were real directions. In Figure 4 and Figure 5, it could be seen that switching tubes and directions of i_{Lr} and v_{Cr} were different from one modal to another.

Equivalent circuit of resonant switching modals was shown in Figure 6. The corresponding relations between V_E and conducting components and resonant inductance current were given in Table 1.

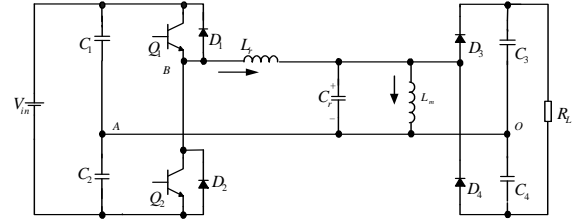
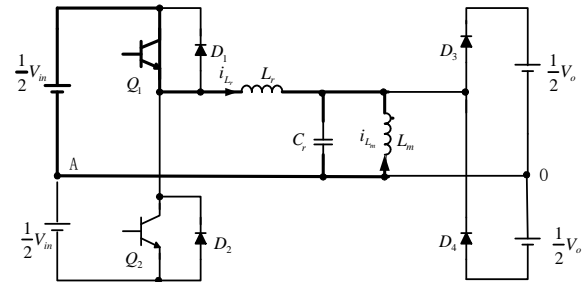
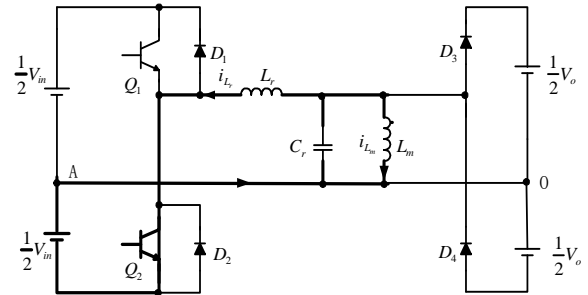


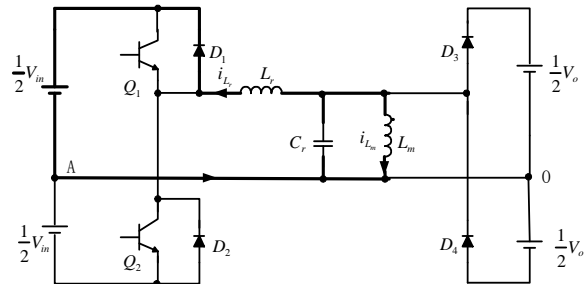
Figure 3. Equivalent circuit of PRDVCs



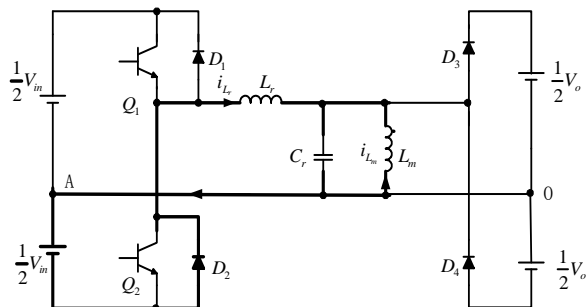
(a) Q_1 conducting state, $i_{Lr} > 0$



(b) Q_2 conducting state, $i_{Lr} < 0$



(c) D_1 conducting state, $i_{Lr} < 0$



(d) D_2 conducting state, $i_{Lr} > 0$

Figure 4. Four resonant switching modals

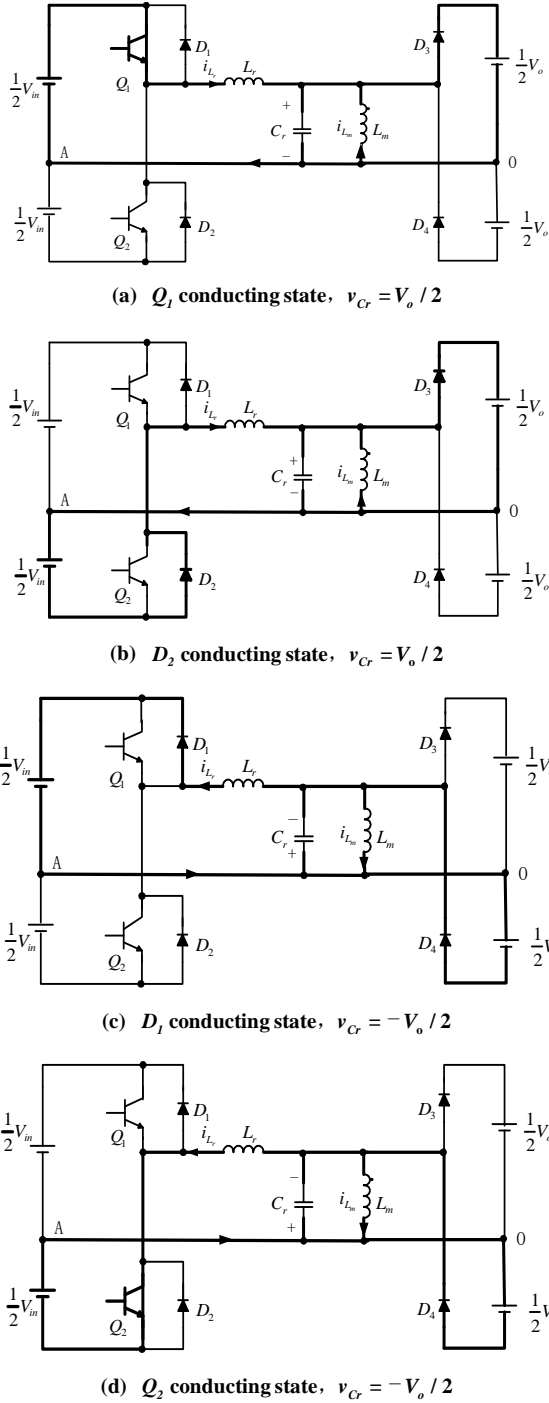


Figure 5. Four linear switching modals

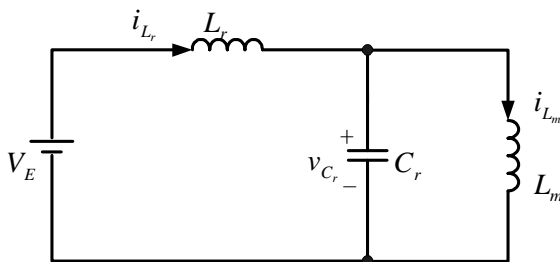


Figure 6. Equivalent circuit of resonant Switching modals

Table 1. The corresponding relations between V_E and conducting components and resonant inductance current

Inducting components	Resonant current i_{L_r}	Equivalent power supply voltage V_E
Q_1	$i_{L_r} > 0$	$V_E = \frac{1}{2} V_{in}$
D_1	$i_{L_r} > 0$	$V_E = \frac{1}{2} V_{in}$
Q_2	$i_{L_r} > 0$	$V_E = -\frac{1}{2} V_{in}$
D_2	$i_{L_r} > 0$	$V_E = -\frac{1}{2} V_{in}$

Analyzing the equivalent circuit in Figure 6, differential equations were shown as (1).

$$\begin{cases} L_r \frac{di_{L_r}(t)}{dt} + v_{C_r}(t) = V_E \\ C_r \frac{dv_{C_r}(t)}{dt} + i_{L_m}(t) = i_{L_r}(t) \\ v_{C_r}(t) = L_m \frac{di_{L_m}(t)}{dt} \end{cases} \quad (1)$$

The initial conditions were assumed as follows.

$$i_{L_r}(0) = I_{L_{r0}}, v_{C_r}(0) = V_{C_{r0}}, i_{L_m}(0) = I_{L_{m0}}$$

when $L_m \gg L_r$, general mathematic expressions of v_{C_r} , i_{L_r} , i_{L_m} could be shown as (2).

$$\begin{cases} v_{C_r}(t) = (V_{C_{r0}} - V_E) \cos \omega_r t + Z_r (I_{L_{r0}} - I_{L_{m0}}) \sin \omega_r t + V_E \\ i_{L_m}(t) = \sqrt{\frac{L_r}{L_m Z_m}} \frac{1}{Z_m} (V_{C_{r0}} - V_E) \sin \omega_r t + \frac{L_r}{L_m} (I_{L_{r0}} - I_{L_{m0}}) \\ \quad (1 - \cos \omega_r t) + \frac{V_E}{L_m} t + I_{L_{m0}} \\ i_{L_r}(t) = i_{L_m}(t) + (I_{L_{r0}} - I_{L_{m0}}) \cos \omega_r t - \frac{1}{Z_r} (V_{C_{r0}} - V_E) \sin \omega_r t \end{cases} \quad (2)$$

where $\omega_r = 1/\sqrt{L_r C_r}$, $Z_r = \sqrt{L_r / C_r}$, $Z_m = \sqrt{L_m / C_r}$.

Equivalent circuit of linear switching modals was shown in Figure 8. The corresponding relations between V_E and conducting components and capacitance voltage were given in Table 2.

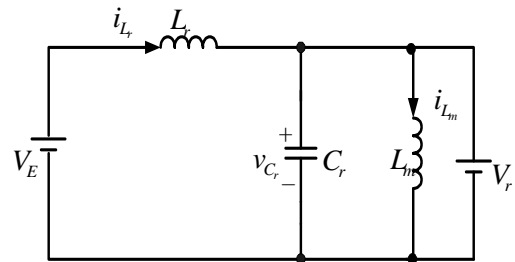


Figure 7. Equivalent circuit of linear switching modals

Table 2. The corresponding relations between V_E and conducting components and capacitance voltage

Conducting components	Equivalent power supply voltage V_E	Equivalent output voltage V_r
$Q_1 \quad D_3$	$V_E = \frac{1}{2} V_{in}$	$V_r = \frac{1}{2} V_0$
$D_2 \quad D_3$	$V_E = -\frac{1}{2} V_{in}$	$V_r = \frac{1}{2} V_0$
$Q_2 \quad D_4$	$V_E = -\frac{1}{2} V_{in}$	$V_r = -\frac{1}{2} V_0$
$D_1 \quad D_4$	$V_E = \frac{1}{2} V_{in}$	$V_r = -\frac{1}{2} V_0$

The initial conditions were assumed as follows.

$$i_{L_r}(0) = I_{L_{r0}}, i_{L_m}(0) = I_{L_{m0}}$$

Analyzing equivalent circuit general mathematic expressions of v_{C_r} , i_{L_r} , i_{L_m} could be shown as (3).

$$\begin{cases} v_{C_r}(t) = V_r \\ i_{L_r}(t) = I_{L_{r0}} + \frac{(V_E - V_r)}{L_r} t \\ i_{L_m}(t) = I_{L_{m0}} + \frac{V_r}{L_m} t \end{cases} \quad (3)$$

4. Three Modes of PRDVCs

PRDVCs appeared three operational modes when loads and operational ranges changed.

4.1 Operational Mode 1

Selecting logical parameters Mode 1 appeared. Steady operating waveforms of Mode 1 were shown in Figure 8. One switching cycle could be divided into six switching modals.

4.1.1 Switching Modal 1 [t_0-t_1]

Before t_0 moment Q_1 and D_3 were conducting, Q_2, D_1, D_2, D_4 were off. At t_0 moment Q_1 would be turned off. D_2 would be conducted because of continuous i_{L_r} , and then Q_2 would be put into operation by ZVS. During this period, v_{C_r} was constant and i_{L_r} would be decreased

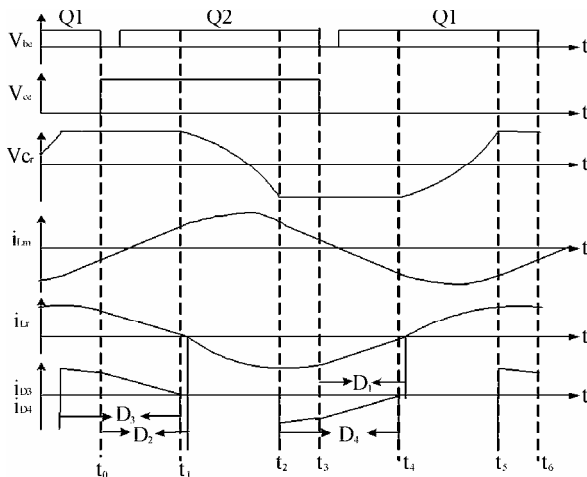


Figure 8. Steady operating waveforms of Mode 1

linearly and i_{L_m} would be increased linearly. Here stored energy. In inductance would be transmitted to load, as shown in Figure 5(b). Substituting initial conditions to (3), the corresponding mathematic models of i_{L_r} , v_{C_r} , i_{L_m} could be deduced.

4.1.2 Switching Modal 2 [t_1-t_2]

At t_1 moment, $i_{L_r}(t_1) = i_{L_m}(t_1)$ and D_3 would shut off naturally. Then D_2 would shut off naturally too. i_{L_r} would be increased reversely and i_{L_m} would be increased positively. Here circuit state would be transferred from linear modal to resonant modal, as shown in Figure 4 (b). Substituting initial conditions to (2), the corresponding mathematic models of i_{L_r} , v_{C_r} , i_{L_m} could be deduced.

4.1.3 Switching Modal 3 [t_2-t_3]

At t_2 moment, $v_{C_r}(t_2) = -V_o/2$ and D_4 was conducted. Here circuit state would be transferred from resonant Modal to linear modal. During this period, v_{C_r} was constant and i_{L_r} would be linearly decreased reversely and i_{L_m} would be linearly decreased positively.

Here stored energy in inductance would be transmitted to load, as shown in Figure 5(d). Substituting initial conditions to (3), the corresponding mathematic models of i_{L_r} , v_{C_r} , i_{L_m} could be deduced.

4.1.4 The second half of cycle [t_3-t_6]

After t_3 moment circuit state would enter the second half of cycle. These were similar to the first half.

4.2 Operational Mode 2

When switching frequency was higher than resonant frequency, PRDVCs would be shifted from Mode 1 to Mode 2 with the decreasing load. Steady operating waveforms of Mode 2 were shown in Figure 9. One switching cycle could be divided into six switching modals.

4.2.1 Switching Modal 1 [t_0-t_1]

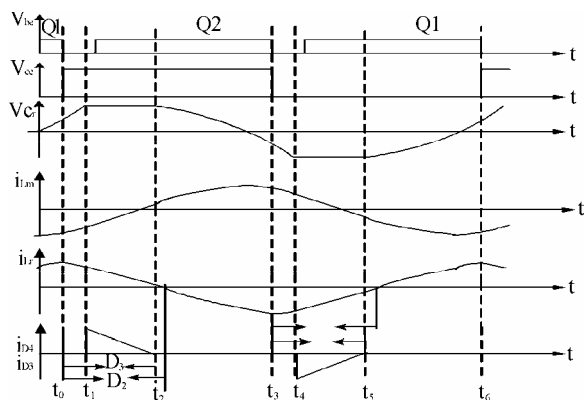


Figure 9. Steady operating waveforms of Mode 2

Before t_0 moment, Q_1 was conducting and Q_2, D_1, D_2, D_3, D_4 were off. At t_0 moment, Q_1 would be turned off and D_2 would be conducted because of continuous i_{L_r} . During this period circuit was in resonant state, as shown in Figure 4(d). Substituting initial conditions to (2), the corresponding mathematic models of $i_{L_r}, v_{C_r}, i_{L_m}$ could be deduced.

4.2.2 Switching Modal 2 [t_1-t_2]

At t_1 moment, v_{C_r} would rise to $V_0/2$ and D_3 would be conducted. Then Q_2 would be put into operation by ZVS. During this period, v_{C_r} was constant and i_{L_r} would be linearly decreased positively and i_{L_m} would be linearly decreased reversely. Here stored energy in inductance would be transmitted to load, as shown in Fig.5 (b). Substituting initial conditions to (3), the corresponding mathematic models of $i_{L_r}, v_{C_r}, i_{L_m}$ could be deduced.

4.2.3 Switching Modal 3 [t_2-t_3]

At t_2 moment, $i_{L_r}(t_2)=i_{L_m}(t_2)$ and D_3 would shut off naturally. Then D_2 would shut off naturally too. i_{L_r} would be increased reversely and i_{L_m} would be increased positively. Here circuit state would be transferred from linear modal to resonant modal, as shown in Figure 4 (b). Substituting initial conditions to (2), the corresponding mathematic models of $i_{L_r}, v_{C_r}, i_{L_m}$ could be deduced.

4.2.4 The second half of cycle [t_3-t_6]

After t_3 moment, circuit state would enter the second half of cycle. These were similar to the first half.

4.3 Operational Mode 3

When switching frequency was lower than resonant frequency, PRDVCs would be shifted from Mode 1 to Mode 3 with decreasing load. Steady operating waveforms of Mode 3 were shown in Figure 10. One switching cycle could be divided into six switching modals.

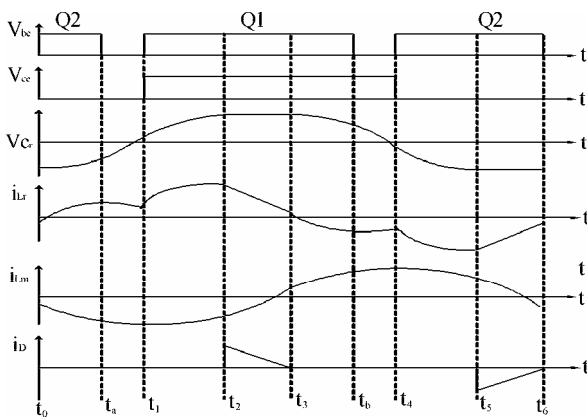


Figure 10. Steady operating waveforms of Mode 3

4.3.1 Switching Modal 1 [t_0-t_1]

Before t_0 moment, Q_2 and D_4 were conducting, Q_1, D_1, D_2, D_3 were off. During this period, circuit was in linear state. At t_0 moment, $i_L(t_0)=i_L(t_0)$ and D_4 would shut off naturally. Then D_2 would be conducted and circuit state would be transferred from linear modal to resonant modal. At t_a moment, Q_2 would be turned off by ZCS, as shown in Figure 4(d). Substituting initial conditions to (2), the corresponding mathematic models of $i_{L_r}, v_{C_r}, i_{L_m}$ could be deduced.

4.3.2 Switching Modal 2 [t_1-t_2]

At t_1 moment, Q_1 would be put into operation and D_2 would be shut off. This was a hard switching and would lead to switching loss. Here circuit was still in resonant state, as shown in Figure 4 (a). Substituting initial conditions to (2), the corresponding mathematic models of $i_{L_r}, v_{C_r}, i_{L_m}$ could be deduced.

4.3.3 Switching Modal 3 [t_2-t_3]

At t_2 moment, v_{C_r} would rise to $V_0/2$ and D_3 would be conducted. Here circuit state would be transferred resonant modal to linear modal and stored energy in inductance would be transmitted to load, as shown in Figure 5 (a). Substituting initial conditions to (3), the corresponding mathematic models of $i_{L_r}, v_{C_r}, i_{L_m}$ could be deduced.

4.3.4 The second half of cycle [t_3-t_6]

After t_3 moment, circuit state would enter the second half of cycle. These were similar to the first half.

5. Converting Conditions of Three Modes

Defined $F = f_s / f_r, M = V_o / V_{in}$. Steady output voltage could be acquired by PFM when PRDVCs was applied. With load being reduced, the steady output voltage could be realized by increasing or decreasing the switching frequency.

When switching frequency increased, PRDVCs state would be converted from Mode 1 to Mode 2. The critical

frequency was $F_1 = \pi / \frac{2\sqrt{M}}{M+1} + \arccos \frac{1-M}{1+M}$ (apparently $M > 0, F_1 \geq 1$).

When $F < F_1$, leading to Mode 1. When $F > F_1$, leading to Mode 2. When switching frequency decreased, PRDVCs would shift from Mode 1 to

Mode 3. The critical frequency was $F_2 = \pi / \frac{2\sqrt{M}}{M-1} +$

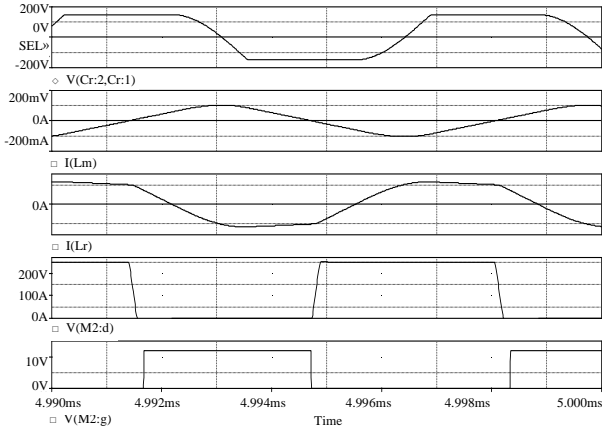
$\arccos \frac{1-M}{1+M}$ (apparently $M \geq 1, F_2 \leq 1$).

When $F > F_2$, leading to Mode 1, When $F > F_2$, leading to Mode 3.

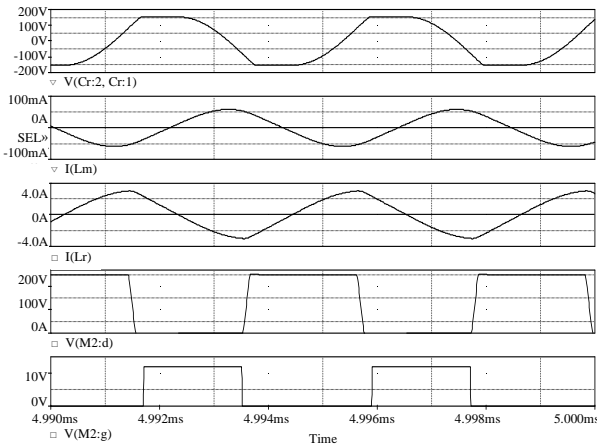
6. Simulation Experiments for Three Modes

For verifying the analyzed results, some simulation experiments were carried on by Pspice. The simulation parameters were as follows.

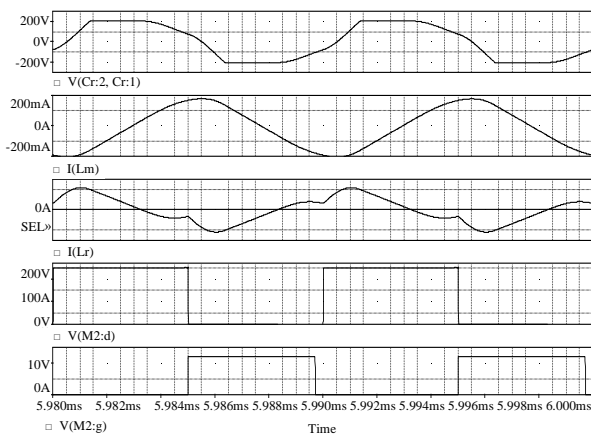
Input direct voltage: $V_{in} = 250\text{VDC}$;
 Output direct voltage: $V_o = 300\text{VDC}$;
 $Q_1(D_1)-Q_4(D_4)$: IRPF640;
 Resonant parameters: $L_r = 63.3\mu\text{H}$ $C_r = 20\text{nF}$;
 Mode 1: Switching frequency $f_s = 150\text{KHz}$;
 Output power; $P_o = 200\text{W}$



(a) Simulation waveforms of Mode 1



(b) Simulation waveforms of Mode 2



(c) Simulation waveforms of Mode 3

Figure 11. Simulation waveforms of three Modes

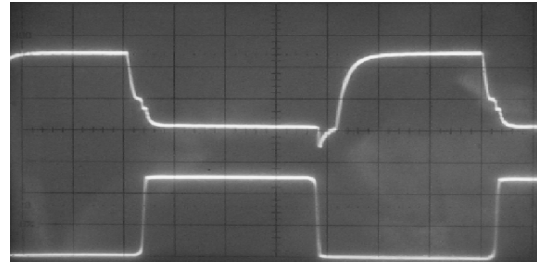


Figure 12. Waveforms of experimental circuit

Mode 2: Switching frequency $f_s = 240\text{KHz}$

Output power $P_o = 60\text{W}$;

Mode 3: Switching frequency $f_s = 60\text{KHz}$;

Output power $P_o = 130\text{W}$.

Simulation waveforms of three modes were shown in Figure 11. It was verified that the analyzed results were correct.

7. Design of 5000V Power Supply

In this section, a 5000V/50mA high-voltage power supply was designed by applying HBPRDVC. The design parameters were given as follows.

Input direct voltage: 250VDC;

Switching frequency: $f_c = 16\text{kHz}$;

Resonant inductance: $L_r = 52\mu\text{H}$;

Resonant capacitance: $C_r = 15000\text{p}$;

Output direct voltage: 5000VDC;

Full load: 250W;

Power tubes: IRPF460;

Ratio of transformer: $n=5.55$;

Under above parameters, PRDVCs operated in Mode 1 when full load. The 5000V/50mA power supply was realized by experiments. The power supply was high performance. It was verified that PRDVCs is feasible for high-voltage power supply. Under full load condition, the relationship between the voltage across power tube and its trigger pulse was given, as shown in Figure 12. Apparently, power tubes were conducted by ZVS. The conversion efficiency was up to 93%.

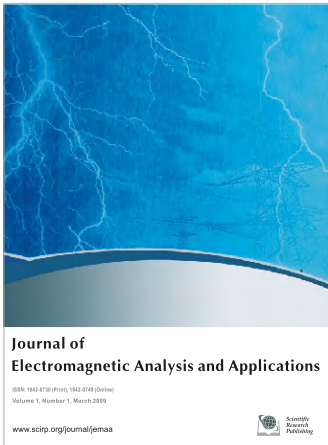
8. Conclusions

A 5000V/50mA high-voltage power supply was built by HBPRDVC. It was verified that the plan is feasible by experiment results. Compared with traditional plans of high-voltage power supplies, PRDVCs has following merits: 1) Soft switching was realized by resonant technology, thereby switching frequency and conversion efficiency were boosted; 2) Distributed capacitance and leakage inductance in high-frequency transformer were available. The influence of distributed parameters was reduced and EMC of the power system was improved. Thus the reliability of the converters was ensured; 3) Both voltage-doubler rectifier and transformer could boost voltage, which reduced

turn's ratio and volume of the transformer, making it easier to produce. Therefore, the miniaturization of high-voltage power supply was realized. In summary, *PRDVCs* was applied to pint-size high-voltage and low-current SMPS, which is worthy of broad application prospect.

REFERENCES

- [1] R. W. Erickson, "The parallel resonant converter," lecture of University of Colorado, chapter 5, 2003.
- [2] X. B. Ruan and Y. G. Yan, "Soft switching technology of DC switching power supply [M]," Beijing: Science Press, 2003.
- [3] R. Oruganti and F. C. Lee, "State-plane analysis of a parallel resonant converter," [C]. IEEE Power Electronics Specialist Conference Record, PESC-1985, pp. 56-73.
- [4] A. K. S. Bhat and M. M. swamy, "Analysis and design of a high-frequency parallel resonant converter operating above resonance," [J]. IEEE Transactions on Aerospace and electronics Systems, Vol. 25, No. 4, pp. 449-458, July 1989.
- [5] Z. G. Lu, "Computer simulation of power supply," [M]. Beijing: Science Press, 2001.



Journal of Electromagnetic Analysis and Applications (JEMAA)

ISSN: 1942-0730 (Print), 1942-0749 (Online)
www.scirp.org/journal/jemaa

JEMAA is a professional journal in the field of electromagnetic analysis, testing and application. The goal of this journal is to provide an international platform for engineers and academicians all over the world to promote, share, and discuss various new issues and developments in the field of electromagnetic. This journal is edited to encourage deeper understanding and greater effectiveness in theory analysis, testing, numerical calculation and engineering application that relevant electromagnetic fields.

Editors-in-Chief

Prof. James L. Drewniak
Prof. Yuanzhang Sun

Electrical Engineering and Materials Science and Engineering, Missouri-Rolla, USA
School of Electrical Engineering, Wuhan University, China

Subject Coverage

JEMAA publishes four categories of original technical reports: papers, communications, reviews, and discussions. Papers are well-documented final reports of research projects. Communications are shorter and contain noteworthy items of technical interest or ideas required rapid publication. Reviews are synoptic papers on a subject of general interest, with ample literature references, and written for readers with widely varying background. Discussions on published reports, with author rebuttals, form the fourth category of JEMAA publications. Topics of interest include, but are not limited to:

- Electromagnetic Numerical Analysis
- Multiphysics Coupled Problems
- Electromagnetic Inverse Problems
- Electromagnetic Structure Optimization
- Test Electromagnetic Analysis Method
- Workshop Benchmark Problems
- Electromagnetic Devices
- Electromagnetic Compatibility
- Electromagnetic Nondestructive Testing
- Electromagnetic Material Modelling

Notes for Intending Authors

Submitted papers should not be previously published nor be currently under consideration for publication elsewhere. Paper submission will be handled electronically through the website. All papers will be peer reviewed. For more details about the submissions, please access the website.

Website and E-Mail

<http://www.scirp.org/journal/jemaa>

jemaa@scirp.org

CONTENTS

Volume 1 Number 1

March 2009

Analysis of the Magnetic Flux Density, the Magnetic Force and the Torque in a 3D Brushless DC Motor M. Pakdel.....	1
Ion Exchange Softening and Alkalization Treatment for Zerodischarge of Circulating Cooling Water X. Z. Bu, L. Xu & L. Su.....	6
Reduction of Cogging Torque in Permanent Magnet Flux-Switching Machines Y. Wang, J. X. Shen, W. Z. Fei & Z. X. Fang.....	11
Impact of Reactive Power in Power Evacuation from Wind Turbines A. Ranjan, S. P. Karthikeyan, A. Ahuja, K. Palanisamy, I. J. Raglend & D. P. Kothari.....	15
Some Advances in the Application of Weathering and Cold-formed Steel in Transmission Tower F. L. Yang, J. K. Han, J. B. Yang & Z. Li.....	24
Identification of Lightning Stroke and Fault in the Travelling Wave Protection G. B. Zou, H. L. Gao, W. B. Su & D. P. Wang.....	31
Desulphurization Characteristic of Industry Alkaline Wastes during Coal Combustion B. Zheng & C. M. Lu.....	36
The Online Assessment of Electric Distribution Network Load Capability H. M. Liu, Z. K. Li, K. Yu & X. Y. Chen.....	42
Complex Dynamics Analysis for Cournot Game with Bounded Rationality in Power Market H. M. Yang & Y. X. Zhang.....	48
The Preliminary Design of IPv6 Home Gateway and Terminal C. Y. Wang & R. Gao.....	61
Analysis and Design of a Kind of Improved Parallel Resonant Converters C. H. Yuan, J. R. Wan, X. Y. Li, H. Shen, Y. P. Liu & G. Y. Li.....	66

